Christian-Albrechts-Universität zu Kiel
Institut für Theoretische Physik und Astrophysik

Kinetic Monte Carlo Simulations of Cluster Growth in Magnetron Plasmas

Dissertation
zur Erlangung des Doktorgrades
der Mathematisch-Naturwissenschaftlichen Fakultät
der Christian-Albrechts-Universität zu Kiel

vorgelegt von
Kenji Fujioka
geb. am 17.11.1979 in Long Branch, New Jersey

Kiel, den 10. Dezember 2015

This work was typeset with LuaLaTeX. Figures were created using gnuplot, the portable command-line driven graphing utility.

Erster Gutachter:	Prof. Dr. Michael Bonitz Institut für Theoretische Physik und Astrophysik, Christian-Albrechts-Universität zu Kiel, Leibnizstraße 15, 24098 Kiel, Deutschland
Zweiter Gutachter:	Prof. Dr. Sebastian Wolf Institut für Theoretische Physik und Astrophysik, Christian-Albrechts-Universität zu Kiel, Leibnizstraße 15, 24098 Kiel, Deutschland
Tag der mündlichen Prüfung:	23. November 2015
Zum Druck genehmigt:	26. November 2015

gez.

_____

Dekan

Abstract

The present thesis is focused on the growth and development of nano-sized clusters in magnetron cluster sources with an emphasis on how these particles can be modeled through kinetic Monte Carlo simulations. Developed models of cluster formation serve to establish a catalog of the fundamental processes that are essential to describing the physics invovled in these systems, and previous Monte Carlo studies that approach a similar problem serve as motivation to finding areas that can be improved.

In developing our kinetic Monte Carlo model, we find that standard kinetic Monte Carlo methods are insufficient to accurately capture the full dynamics of the system. We therefore develop a variation to standard kinetic Monte Carlo algorithms that allows for the fluctuating of background conditions to be taken into account. This new variation is analyzed and tested to ensure its agreement with standard methods and is shown to better capture the variability of process rates within the system.

The included processes are broken into two basic sections: transport and growth. As a first look at transport processes, we develop a simple collision model to address the thermalization of energetic atoms introduced into the system by sputtering. We then move towards a continuum model governed by the Smoluchowski equation and analyze the processes involved in establishing a free metal atom density profile, rates for 2D radial diffusion, and 1D axial motion. In analyzing the growth processes, we start with developing a cluster size index scheme that greatly allows us to accelerate the overall simulations. We then look at the fundamental growth processes of nucleation, atom attachment and coagulation.

Throughout our analysis we focus on the cluster size distribution. Results of the model are examined for the effect of parameter variations to gain insight into how the various processes affect cluster growth. We compare results with an experimental study and find that the developed model can accurately reproduce the size distributions of

emitted clusters.

Kurzbeschreibung

Anmerkung: Diese Arbeit wurde auf Englisch verfasst. Die Kurzbeschreibung ist eine Übersetzung der englischen Fassung von Seite i.

Die vorliegende Arbeit befasst sich mit dem Wachstum von Nanometer großen Clustern in Magnetron-Clusterquellen, wobei der Fokus darauf liegt, wie die Teilchenerzeugung mit Hilfe der kinetischen Monte-Carlo-Methode simuliert werden kann. Bereits etablierte Modelle zur Clustererzeugung ermöglichen die Aufstellung eines Katalogs grundlegender Prozesse, welche nötig sind, um die diesen Systemen zugrunde liegende Physik zu beschreiben. Dieser Arbeit vorausgehende Untersuchungen ähnlicher Probleme durch Monte-Carlo-Methoden motivieren dazu, verbesserungswürdige Teilbereiche zu finden.

Während wir unser kinetisches Monte-Carlo-Modell entwerfen, stellen wir fest, dass es mit Standardalgorithmen der kinetischen Monte-Carlo-Methode nicht möglich ist, die volle Dynamik des Systems korrekt zu beschreiben. Deshalb entwickeln wir eine Variante der Standardalgorithmen, welche es erlaubt, fluktuierende Hintergrundbedingungen zu berücksichtigen. Diese neue Variante wird analysiert und getestet, um ihre Übereinstimmung mit den etablierten Zugängen zu zeigen. Außerdem wird gezeigt, dass sie die Veränderlichkeit der Prozess-Raten im System besser erfasst.

Die beinhalteten Prozesse werden in zwei grundlegenden Abschnitten behandelt: Transport und Wachstum. Bei der ersten Behandlung der Transportprozesse entwickeln wir ein einfaches Stoßmodell, um die Thermalisierung energetischer Atome zu beschreiben, die durch Sputtern in das System gelangen. Danach wenden wir uns einem Kontinuumsmodell zu, das durch die Smoluchowski-Gleichung bestimmt ist. Hier untersuchen wir die Prozesse, die an der Ausbildung eines Dichteprofils freier Metallatome sowie den Raten für radiale Diffusion in zwei Dimensionen und die eindimensionale

Bewegung entlang der Achse beteiligt sind. Für die Analyse der Wachstumsprozesse beginnen wir damit, ein Schema der Clustergrößen-Indizes zu entwickeln, welches eine bedeutende Beschleunigung der gesamten Simulation ermöglicht. Anschließend behandeln wir die grundlegenden Wachstumsprozesse Nukleation, Anlagerung einzelner Atomen und Koagulation.

Das Hauptaugenmerk all dieser Untersuchungen liegt auf der Clustergrößenverteilung. Die Ergebnisse der Modellierung werden im Hinblick darauf untersucht, wie sich durch Parametervariation der Einfluss der verschiedenen Prozesse auf das Clusterwachstum verstehen lässt. Zudem vergleichen wir die Ergebnisse mit experimentellen Untersuchungen und stellen fest, dass sich das entwickelte Modell eignet, um die Größenverteilungen emittierter Cluster genau zu beschreiben.

Contents

List of Figures

Research is what I'm doing when I don't know what I'm doing.

Wernher von Braun

CHAPTER 1

Motivation and Outline

The problem of the agglomeration of small particles into larger and larger masses can be seen at virtually all known length scales. At the astronomical level, there are planets and stars that condense out of cosmic dust [1–3]. At more human length scales there is the condensation of water droplets into clouds [4, 5]. In the nanoscale regime there is the formation of nanoparticles [6, 7].

Obviously, there are very different physics at work in each of these examples. But there is often a general framework from within which all these examples may work. Generally there is a gas of particles (dust, molecules, or atoms) that undergoes condensation. From this small seeds are nucleated that serve as preferred attachment sites for other constituents of the gas. The condensation of the gas onto the seeds leads to the growth of larger particles. As larger particles grow, collision frequencies increase and more dynamics may come into play. For planet and star formation, gravitational forces may become significant leading to a greater attraction of the surrounding material. In cloud formation larger droplets eventually become big enough to overcome convective currents leading to rainfall. For nanoparticles on a substrate, we may observe the formation of a percolation network that can lead to novel material properties.

The present work deals with the growth of metal nanoparticles from a supersaturated [8] gas of metal atoms. Such nanoparticles are thought to form in a manner consistent with the basic ideas above. We will remain largely interested in the dynamics of the particle formation and will look at how processes, both general and system

specific, affect particle growth. Our basic measurement will be the distribution of particle sizes, with the goal of understanding how we may affect our system to achieve a desired particle size.

This knowledge can in turn be utilized in a number of emerging technologies. The exact nature of the use of metal nanoparticles is beyond the scope of this current work, but we can find many examples of the implemenation of nanoparticles across the spectrum of modern technology. In the biomedical field: copper and silver coatings have been shown to admit anti-bacterial properties [9], and gold nanoparticles have been shown to aid in the delivery of cancer specific drugs [10]. In the field of electronics, nanoparticles have been implemented in the creation of data storage devices [11] and offer a possible route to a quantum computer [12]. In the environmental field, nanoparticles may serve as a means for water treatment and purification [13] or conversely nanoparticles may be a source of air pollution [14]. With the work contained in the present thesis, it is our hope that understanding how nanoparticles may form and how we may control their size, may further inform some small portion of the many fields that encounter nanoparticles.

Thesis Outline

This work is broken into six further chapters.

Chapter 2 gives an introduction to experimental and technical applications of magnetron clusters sources, the specific system from within which we discuss the growth of metal nanoparticles. We will also look at some established models and simulations that have previously been done on the topic.

Chapter 3 presents the algorithmic and computational framework of Kinetic Monte Carlo (KMC) simulations. We will look specifically at the two most common algorithms and discuss their strenghts and weaknesses. We then present a modified KMC algorithm to address the limitations of the former two.

Chapter 4 is concerned with the transportation of metal atoms and clusters in the system. We start with a simple collison-based model and extract information on the thermalization of sputtered atoms. We then move to an equilibrium approach to metal transport models based on the convection-diffusion (AKA Smoluchowski) equation. With the Smoluchowski equation as a foundation we will look at models for a static free metal atom density, radial diffusion to chamber walls, and axial drift-diffusion through the chamber.

Chapter 5 deals with the processes specific to cluster growth. We first look at how physical properties of metal clusters are treated in the model. Then we look at the nucleation of new metal clusters from the surrounding gas. Next we examine the fundamental growth process of single atom attachment to the cluster surface. Finally we investigate the coalescence of two clusters in the formation of a larger one.

Chapter 6 shows results of the model outlined in the previous three chapters. We will remain focused on the size distribution of the metal clusters emitted from the source. We will investigate the effects of various physical parameters and the interplay of the included processes.

Chapter 7 summarizes the results and presents conclusions. We will also discuss some known limitations of the current model and possible extensions that could alleviate them.

It doesn't matter how beautiful your theory is. It doesn't matter how smart you are. If it doesn't agree with experiment, it's wrong.

Richard Feynman

CHAPTER 2

Introduction

In this chapter we will introduce the specific experimental apparatus that serves as the source of metal nanoparticles: the magnetron cluster source. We examine what is known about the system's behavior and identify key experimental parameters that are known to affect the emitted cluster size distribution. We then look at several theoretical studies that have been done with these systems, with the intent of seeing what general processes are common amongst them and see what improvements may be implemented. This leaves us with a clear direction to take for our own approach to the simulation of cluster generation in a magnetron cluster source; one that is motivated by experiment, informed by existing models, and driven to improve upon the known limitations of previous simulations.

2.1 Magnetron Sputtering

The development of the magnetron can be traced back at least into the 1930s [15]. Early innovations in the 1940s found their use in radar navigation equipment and microwave oven technology [16]. However it was not until the 1970s that magnetrons found an application in sputtering technology [17, 18]. Sputtering, in turn, is the removal of atoms or molecules from the surface of a bulk material target via the impingement of energetic particles. Magnetron sputtering became a highly reliable and commercially viable means of thin film production in the 1980s [18]. Furthermore, the use of magnetron

sputtering as a source for nanoclusters is often credited to the work of Haberland starting in the early 1990s [15]. So while magnetron technology has been around for nearly 100 years, its slow and steady advancement has only seen its application as a source of nanoclusters in the last 20 years.

2.1.1 Basics of Operation

The basic magnetron cluster source consists of a cylindrical chamber with a planar magnetron at one end perpendicular to the chamber axis and a small orifice at the opposite end. A metal target is placed over the magnetron and an operating buffer gas is continually pumped into the chamber. Outside of the chamber there is a vacuum and this sets up a pressure differential through the orifice that drives material out of the chamber. A voltage is applied to the metal target (anode). This sets up an electric field that can initiate some charge separation in the atoms of the buffer gas. Then power is delivered to the magnetron, which establishes a toroidal magnetic field. Free electrons are captured in a so-called "race track" above the target and neutral buffer gas atoms are easily ionized by these electrons which then becomes the driving force for the plasma in the system. The positive buffer gas ions are drawn towards the negative bias of the target and energetic collisions free individual metal atoms from the target's surface. This is the sputtering process. These sputtered metal atoms are highly energetic and very quickly move away from the target and eventually come into thermal equilibrium with the buffer gas background. The amount of sputtered material is proportional to the power applied to the target. If a sufficient amount of power is applied, the sputtered metal atoms will constitute a super saturated gas. Some of this gas will diffuse to the boundaries of the chamber and will condense along the walls and even back on the target. A small portion of the sputtered metal will condense among itself to form nano-sized clusters of the material. These clusters can be picked up by the overall drift of the buffer gas and eventually exit the system through the orifice.

2.1.2 Experiments

In recent years there have been a number of experimental studies on the formation, growth, and deposition of clusters from magnetron cluster sources [19–25]. Collectively, these experiments show that the production of clusters and their size distribution are influenced by the composition of materials (target material and the operating/buffer gas), the power delivered to the magnetron, the input flow rate of the buffer gas, the

orifice shape and size, the temperature of the chamber walls, and the details of the magnetron used (balanced vs. unbalanced).

2.2 Models and Studies

In an attempt to further the understanding of magnetron cluster sources, researchers have proposed a number of models that compare with varying degrees to experimental results. Here we look at several models of magnetron cluster sources based on semi-analytic methods and simulations. We will examine some strengths and weaknesses of each to inform our own approach to the modeling of magnetron cluster sources.

2.2.1 Semi-Analytic Models

Through the following semi-analytic models we gain insight into the formation and growth of clusters by looking at processes that likely dominate the development of clusters in magnetron sources. Various theories are used to find analytic rates for the processes involved and then simplified models are solved based on those rates to get a base understanding of what each process adds to the overall picture of cluster development.

One of the earlier semi-analytic studies was conducted by Hihara and Sumiyama in 1998 [26]. Their model posits the formation and growth of nanoclusters to be based on three fundamental stages:

- embryo formation
- cluster-cluster collision
- vapor condensation growth

The embryo formation stage consists of three-body collisions that release the latent heat of condensation while conserving energy and momentum for the three bodied system. The three bodies under consideration are two metal particles and a third buffer gas atom. At some point, these small embryos reach a size such that the release of the latent heat of condensation can transfer to internal degrees of freedom. Once this size is reached, the embryo is considered to be fully formed and stable, and other growth mechanisms may proceed. Hihara and Sumiyama take the stable embryo to be reached for clusters of 7 metal atoms. The remaining two growth mechanisms implemented adhere to the

kinetic theory of ideal gases for two-bodied collisions. The cluster-cluster collision rate for a cluster of size k (atoms) is based on a balance equation for the production of a k-sized cluster by the addition of two smaller clusters $i + j = k$ minus the loss of k-sized clusters that collide with some other cluster size. They write,

$$\frac{dn_k}{dt} = \sum_{\substack{i+j=k \\ i \leq j}} C_{ij} n_i n_j - \sum_i C_{ik} n_i n_k \tag{2.1}$$

where n_α is the number density of the α species and C_{ij} is the product of the collision cross section and the relative thermal velocity of the i and j species. The final element included in the model is the vapor condensation growth process where single atoms are added to clusters one-by-one. In their model, this growth rate encompasses a net difference between the rates for condensation and evaporation for single atoms from the cluster's surface. They write the condensation rate as:

$$\frac{dk}{dt} = \sigma_{ka} v_{\text{th}} n_0 (1 - \eta), \tag{2.2}$$

where k is the cluster size in atoms, σ_{ka} is the geometric collision cross section between cluster and atom, v_{th} is the mean relative velocity, n_0 is an initial metal atom density, and η is a condensation rate factor that accounts for reevaporation.

Hihara and Sumiyama discussed the fundamental physics involved in their model, as roughly outlined above. However, for the actual analysis of their model, they made two rather large simplifications. First, they only analyzed the cluster-cluster and the vapor condensation processes independently. That is, they ran two separate analyses to see the effect of the different growth processes. They did not implement a full analysis that allowed for any competition or interaction of these two processes. Second, a full treatment of embryo formation would have involved a heterogeneous mixture of metal ions, metal atoms, and excited buffer gas atoms. This was found to be too complex for their analytical treatment at the time, and they instead opted for homogeneous approximation of just metal atom collisions. In effect this allowed them to reduce the embryo formation process to an input parameter with which they tested their models.

In the analysis of the models, Hihara and Sumiyama found that the cluster-cluster collision process was too slow to reproduce their own experimental results. In these results, they took the residency time (duration of the clusters' time spent in the growth chamber) as a free parameter to fit to their experimental data. They found that they needed to increase the residency time by 2 orders of magnitude over initial approximations in order to provide a good fit for the model's cluster size distribution compared to

experiment. The vapor condensation process provided for a much better fit, although they only looked at the mean cluster size, not a full size distribution. Thus they concluded that the cluster-cluster collision process is not a significant player in the overall description of the observed cluster size distributions and that the vapor condensation process dominates cluster growth.

In more recent years, there has been a more exhaustive model put forth by Smirnov [7, 15, 27–29]. Similarly to Hihara and Sumiyama, Smirnov recognizes three essential processes that need to be accounted for:

1. nucleation of new clusters
2. cluster-cluster collision
3. single atom attachment to existing clusters

Smirnov uses a slightly different vocabulary to refer to essentially the same three processes of Hihara and Sumiyama.

Essentially, Smirnov's cluster collision process and atom attachment process is equivalent to Hihara's cluster collision and vapor condensation growth, respectively. However, Smirnov's model makes an improvement to the generation of clusters.

The nucleation process is akin to the embryo formation stage. Smirnov also envisions this as a three body process between two free metal atoms and a single buffer gas atom. Where Smirnov's model differs however is in what constitutes a stable nucleus (embryo). Smirnov allows for the formation of stable dimers, two atom bound state, to initiate the growth of clusters as opposed to Hihara's 7 atom embryos. Smirnov goes on to model the nucleation process explicitly, giving the rate for which new clusters are added to the system as,

$$\frac{dN_{\mathrm{d}}}{dt} = K n_{\mathrm{m}}^2 n_{\mathrm{g}}. \tag{2.3}$$

Here, N_{d} is the number of dimers, K is a nucleation constant that can be found experimentally, n_{m} is the density of free metal atoms, and n_{g} is the number density of buffer gas atoms. This already presents a major step forward from Hihara's model in that it allows one to more accurately model the introduction of new clusters.

2.2.2 Direct Simulation Monte Carlo

Simulation work on cluster growth in magnetron sources has already been achieved with the Direct Simulation Monte Carlo (DSMC) approach.

Briehl and Urbassek's approach to the DSMC method [30] starts by allowing for several processes to occur. They use:

- elastic collisions between any atoms
- collision of two metal atoms to form metastable dimers
- cluster-cluster collisions
- inelastic collision between clusters and gas atoms
- single atom evaporation from a cluster

They initialize a system that consists of a volume to represent the chamber. Into this volume, they place a finite number of buffer gas (10^6) and metal atoms (10^5), with initial Maxwellian velocity distributions, and the simulation is then ready to begin. Throughout the simulation, each individual particle object is tracked for its energy and size (in case of clusters). At each Monte Carlo time-step, they randomly choose a pair of atoms to act upon for each of the included processes. Each process may then produce a change to the state space of the entire system; but it need not, as their algorithm allows for a null process to occur where the chosen pair of atoms is returned without any action taking place. The simulation continues to iterate over all processes until the preset time limit is reached, at which point the size distribution of clusters is recorded.

The elastic collision process essentially acts to move the velocity distribution of the initialized atoms away the equilibrium Maxwell distribution, and this may affect the probability outcomes of the other processes. The collision of two metal atoms may result in the formation of a metastable dimer, however, the newly formed dimer only has a limited lifetime, thereafter it will break apart to two atoms again. In order for it to become stable, it must undergo another collision process with any other atom species before its lifetime limit is reached. The cluster-cluster collision process allows for the collision of two smaller metal clusters, sized in atoms i and j, to produce a larger cluster of size k conserving atom number, $i + j = k$. The inelastic collision process allows for internal energies of the clusters to be lowered (or raised), thus making it less (more) likely that an evaporation process may take place. Finally, the evaporation process may remove a single atom from the cluster's surface resulting in a smaller cluster plus an additional free metal atom.

The simulation presented by Briehl and Urbassek is interesting for the direct treatment of the metastable dimers, however it also suffers some drawbacks. First, it somehow treats each of the included processes on equal footing. At each time-step, each of the included processes may be performed. Thus, in order to avoid treating all processes as if they have equal rates, care must be taken to allow for the proper probability of a null process to occur. The model also lacks any sort of spatial resolution. There is no treatment of particle drift towards an exit. Any particle species are assumed to be homogeneously distributed throughout the space.

As for results, the DSMC method only allowed for relatively small system dimensions to be observed (1 cm chamber radius and 1 cm chamber length). Consequently, only small clusters could be achieved. The mean size of the cluster depended strongly on the residence time of the atoms through the space, with longer residence times resulting in larger clusters. Even so, given the maximal residence time of their investigation, clusters did not grow much larger than 30 atoms, this is quite small compared to the known sizes of 10^4 atoms in experiments.

2.3 Silane Simulations

The simulation model of Briehl and Urbassek is not the only numerical model of cluster formation in a plasma. Notably, there is also a rather complete picture of nanoparticle formation in dusty plasmas throught the work of De Bleeker[31, 32]. These simulations present a fluid model for the description of silane nanoparticle formation in a dusty plasma environment. Among the included effects are those of collisions with free electrons that allow for particle charging as well as the inclusion of a large number of particle species as silane nanoparticles may have a complex chemistry in the form Si_nH_{2n}. These simulations, may serve as a reference point for further developing the present model to account for more of the plasma environment.

2.4 Outlook

We find that there is a rich supply of experimental data to draw upon and we are interested in developing a model of the magnetron cluster source to add to the collective knowledge of these systems. The semi-analytic model developed by Smirnov provides for a sufficient starting point of processes and rates to consider [7, 15, 27]. While the DSMC work of Briehl and Urbassek [30] provides a suitable approach to the simulation

of clusters in magnetron sources, we find some limitations in their model that warrants the need to take a different direction. We will utilize a kinetic Monte Carlo framework that places more emphasis on the rates for processes to occur, thereby addressing the issue surrounding the equal treatment of processes in DSMC. Additionally, we will find a solution that can address larger particle sizes than those simulated with DSMC. These elements will be brought together into an original model that can accurately and efficiently simulate the growth of clusters in magnetron sources.

Learning by doing, peer-to-peer
teaching, and computer simulation
are all part of the same equation.
NICHOLAS NEGROPONTE

CHAPTER 3

Kinetic Monte Carlo Methods

A substantial portion of the present thesis is dependent on the specifics of the chosen algorithm of Kinetic Monte Carlo (KMC). In addressing the specifics of the problem at hand, we find that traditional algorithms of KMC are insufficient to fully and accurately describe the systems encountered in magnetron cluster sources. To help solve these problems we borrow some elements from an algorithm used in astrophysical simulations [33]. This current thesis then builds a new approach towards simulations of cluster growth by working off of the semi-analytic models of Smirnov [7] and implementing an alternative KMC method.

3.1 General Kinetic Monte Carlo Methods

In general KMC methods are statistical models that realize the time evolution of a system along one of its possible paths through its entire state space [34–37]. In this respect, one may need to analyze sufficiently many KMC runs together to gain some insight into the relevant statistical properties of the system. The evolution through the state space is mediated by the included processes. We will define a "process" as a type of action that can occur within a system. A single instance of a process will be termed an "event". Each process is associated with a distribution of waiting times for the process to be completed or performed. Single events may or may not be associated with a definite process time, as we will see below. In either case, a single event is somehow chosen to

be performed and the completion of the event moves the system to a new point in its state space. All KMC algorithms require a set of base processes that are included in the model. This is both a strength and a weakness for KMC methods. The weakness being that we must know before hand the relevant physics to include, the strength being that we can single out specific processes in order to see their lone effect on the system.

There are two equivalent algorithms for standard KMC methods. The Bortz-Kalos-Lebowitz (BKL) algorithm [38] and the First Reaction (FR) algorithm [39, 40]. These will be discussed in the following sections.

3.2 Bortz-Kalos-Lebowitz (BKL) Algorithm

The BKL algorithm assumes that all possible events that may occur are independent Poisson processes. Therefore, the waiting times for these included processes are efficiently described by exponential distributions. Exponential distributions are unique for being the only distribution with the memoryless property. This means the transition from one state to the next is completely independent of the system's history. Instead, the transition out of the current state is soley dependent on the current state, and the sequence of states that the system moves through can be effectively studied via the theory of Markov Chains [41]. [1]. An exponential distribution takes one parameter, λ, the rate of process occurrence [2].

Let us look at a simple example of the BKL algorithm in action. We will allow for N possible events all of the same process described by a single rate λ. If we like, we may envision N particles randomly placed on a large lattice such that no two particles sit at adjacent sites. The rate λ may then refer to a rate for any particle to jump from its current site to a neighboring one. We can define a total rate (λ_{total}) for some event to occur as the sum of rates of all the events. In our example we have $\lambda_{\text{total}} = \sum_{i=1}^{N} \lambda = N\lambda$. The distribution of times for moving from the current point of our state space to a new one is now described by an exponential distribution with a rate parameter $N\lambda$. We advance

[1] For an in-depth discussion of the mathematics and theory of Kinetic Monte Carlo and its relation to Markov chains, see the doctoral thesis of L. Rosenthal, Ref. [41].

[2] A note on vocabulary: throughout this work, "rate" will only refer to the inverse of the mean time for the process to occur with respect to exponentially distributed waiting times. Of course most other distributions will allow for an inverse mean time to be defined, but for clarity these will not be referred to as rates.

the global clock by sampling from the cumulative distribution function (CDF),

$$P(t) = \int_0^\infty N\lambda e^{-N\lambda t} dN = 1 - e^{-N\lambda t}. \tag{3.1}$$

A sample from the CDF returns a real number on the interval (0,1). We then compose $1-P(t) = r$ which remains a real number on the same interval as $P(t)$. An advancement of the global clock can then be composed as,

$$r = e^{-N\lambda t} \rightarrow t = \left(-\frac{1}{N\lambda}\right) \ln(r). \tag{3.2}$$

The BKL algorithm then has us randomly pick one of the events to carry out, which completes a KMC step. A schematic of this algorithm may look like:

1. Initialize N events in our system.
2. Find the total rate λ_{total}.
3. Advance the global clock:
   sample r from a uniform distribution (0,1)
   $t = \left(-\frac{1}{\lambda_{\text{total}}}\right) \ln(r)$
4. Randomly pick one of the N events to perform.
5. Return to (2)

This is a very simple example and we can imagine that as the system gets more complex, the algorithm outlined above will have to be modified. For instance, we may need to keep in mind that λ_{total} may need to be updated. Within our simple picture, for example, if two particles are in neighboring lattice sites then perhaps we want to eliminate any event that could be performed such that two particles are sharing a single site. Or perhaps we can consider an attractive pair-wise potential that tends to bring particles together; then after each movement we may need to calculate new rates for each particle. This may also entail a modification to step (4) above to include a weighting system such that events with larger rates are more likely to be chosen to be performed. We may also consider adding more processes that may occur: adding new particles onto the lattice, removing particles, allowing particles to combine, etc. Each additional process should be governed by a new rate λ_i and needs to be accounted for properly.

The BKL algorithm is nice because it is fairly well studied and it is efficient. However, it relies on at least one crucial rule: that the waiting times for each process are exponentially distributed. The exponential distribution is applicable for a diffusive jump between lattice sites as in the case for models of surface diffusion. However, for cases of a continuous diffusive motion over some length interval, one does not find an exponential distribution for the time to transverse the interval. To amend this deficit within the BKL algorithm we have to look at another traditional KMC approach.

3.3 First Reaction Algorithm

While maintaining equivalence to the BKL algorithm for cases where the above points one and two are met, the First Reaction algorithm can address the above sighted shortcomings. The equivalence between the BKL algorithm and the First Reaction algorithm comes from a property of the exponential distribution. The distribution of the minimum of a set of independent exponentially distributed variates is distributed exponentially with a rate given by the sum of rates of each variate. Where the BKL algorithm advances time via the total rate and randomly selects the next event, the First Reaction algorithm samples a time point for each process to occur separately and simply performs the event with the smallest waiting time.

In order to extend the BKL algorithm beyond the limitations of the point above, the First Reaction algorithm sets up a list of waiting times for all possible events to occur. Each of those waiting times are drawn from a distribution specific to the process at hand and we are no longer required to include only events whose waiting times are distributed exponentially. As a consequence of including processes with non-exponential distributions, the First Reaction algorithm moves the Kinetic Monte Carlo method away from the theory of Markov Chains.

Another important issue in Kinetic Monte Carlo methods is the handling of processes whose rates or mean process times are time dependent. The BKL algorithm, is somehow set up to treat this directly. One can, for instance, have all rates be computed at every Monte Carlo step. We are then only concerned with the current state the system is in. In terms of the First Reaction algorithm implemented for exponential distributions, we would only need to resample any events whose rates underwent a change due to the last event. These methods for handling changing rates are accurate for exponential distributions, due to the memoryless property. But suppose we are utilizing the First Reaction algorithm with distributions besides the exponential. The method then becomes

unclear. Indeed, we can not simply resample the time for an event's occurance from the new distribution because we will likely lose some information. The other alternative is to ignore the changes to the sampled distribution. This solution is not theoretically correct or satisfying, and can lead to some large errors.

For a concrete example of how this can be important, consider the diffusion of a particle through an interval with a decreasing gradient of the medium's density.

Instead, we must look for an alternative method for treating these changes. The solution proposed here is referred to as Threshold Kinetic Monte Carlo.

3.4 Threshold KMC Algorithm

Threshold KMC is a proposed solution to the problem of dealing with changing parameters of a distribution. As this solution is a strong component of the work done within the model of the present thesis, we will look at its principles with several lenses in the hopes of gaining a firm understanding of its composition and utility.

3.4.1 Astrophysical Motivation

The central idea for this approach comes from astrophysical Monte Carlo simulations for the determination of polarization maps of light traveling through stellar dust clouds [33]. Part of the algorithm presented by Fischer includes an approach for sampling the mean free path of a photon through the cloud. In this physical system, the photon's mean free path is dependent upon the dust cloud's density which itself is position dependent. The algorithm is therefore used to find a photon's annihiliation point given some fluctuating background conditions.

Fischer begins by sampling the dimensionless optical depth, τ. This optical depth defines the decay of light intensity, I, in a continuous manner by $I(\tau) = I_0 \mathrm{e}^{-\tau}$. The probability, $f(\tau)d\tau$, to reach a given depth is given by a ratio between the intensity $I(\tau)$ at τ and the incident intensity reaching that point.

$$f(\tau)d\tau = \frac{I(\tau)d\tau}{\int_0^\infty I(\tau)d\tau} = \mathrm{e}^{-\tau}d\tau. \tag{3.3}$$

From this Fischer finds the corresponding cummulative distribution function for a photon being transmitted beyond the optical depth, τ,

$$F(\tau) = \int_0^\tau \mathrm{e}^{-\tau'}d\tau' = 1 - \mathrm{e}^{-\tau}. \tag{3.4}$$

The cummulative distribution is defined on the interval $(0, 1)$. Fischer uses this to sample the optical depth by drawing a uniform random number, R, on the interval $(0, 1)$ and setting it equal to $F(\tau)$. This will yield a sample for the optical depth to be given by,

$$\tau = -\ln(R - 1) \tag{3.5}$$

Next, Fischer relates the random walk coordinate, s which refers to a position along an arbitrary path, to τ. He writes the general relation between τ and s as,

$$\tau = \int_0^s n(r)C(r)ds, \tag{3.6}$$

where $n(r)$ is the position dependent number density of dust particles, $C(r)$ is the extinction cross section between a photon and dust elements, and $(n(r)C(r))^{-1}$ is the mean free path length. However, as space is discretized in Fischer's model, he must index the spatial elements with a length, Δs_j, and the integral becomes a summation,

$$\tau = \sum_{j=1}^{j_{\max}} n(s_j)C(s_j)\Delta s_j. \tag{3.7}$$

With this, Fischer has a method for determining the point at which a photon is annihilated. The algorithm can be written as:

1. sample τ as $\tau = -\ln(R - 1)$ where R is a random number on the interval (0,1)
2. as the photon moves through space, maintain the sum: $\tau' = \sum_{j=1}^{j_{\max}} n(s_j)C(s_j)\Delta s_j$
3. when $\tau' \approx \tau$ at $j = j_{\max}$, then the photon is annihilated

We can say, that the sampling of τ sets a threshold to which τ' is incremented. Once the threshold is met, the event is carried out.

3.4.2 Kinetic Monte Carlo Analogy

With an understanding of Fischer's implementation of this algorithm, we look to make an analogy that will be useful in a KMC setting. Apart from the differences of the physical nature of Fischer's work and the present model, the fundamental difference between his implementation and the demands of KMC is the domain variable over which it is applied. In Fischer's work, the goal is to find a spatial point where an event takes place.

In KMC the emphasis is within the time domain; we are looking for a point in time for the completion of an event.

First we make an analogy to the optical depth parameters in Fischer's model. We want to have a sample of a dimensionless quantity, T. Typically, in KMC simulations, samples are made from an appropriate distribution of the time for an event to occur. We will stick with this implementation, but compose a dimensionless parameter by scaling the sample by the inverse of the mean time for the process completion, k, or inverse-mean. That is, our dimensionless sample is given by,

$$T \sim k_0 f(t, \{\beta_0\}). \tag{3.8}$$

The distribution function $f(t, \{\beta\})$ describes the waiting times for our chosen process, and $\{\beta\}$ is a set of background dependent parameters. The subscript applied the notation of the distribution parameters and the inverse-mean are to remind us that these quantities are determined by the initial conditions at the time the sample is made.

Next we compose the elements of the summation, T'. In Fischer's model, each element of the summation was composed of a unit of length along a path multiplied by the inverse-mean free path. The KMC analog just needs to place these quantities in the time domain. The most natural connection is to have a unit of time along some path multiplied by the inverse-mean time. That is, we make the substitutions:

$$\begin{aligned} \Delta s_j &\to \Delta t_j \\ n(s_j)C(s_j) &\to k_j, \end{aligned}$$

and we compose the sum,

$$T' = \sum_{j=1}^{j_{\max}} k_j \Delta t_j. \tag{3.9}$$

This leads us to the picture that we have clusters moving over finite intervals whose background conditions provide for variations in the mean time for a process to occur. Again, analgous to Fischer's algorithm, we write the new KMC algorithm as:

1. sample T as $T \sim k_0 f(t, \{\beta_0\})$
2. as the cluster moves through space, maintain the sum: $T' = \sum_{j=1}^{j_{\max}} k_j \Delta t_j$
3. when $T' \approx T$ at $j = j_{\max}$, then the cluster event is performed

It should be stated here that the Threshold Method as it is outlined above, is not necessarily a complete algorithm in its own right. At the moment, we have left out a discussion of the exact nature of the time step Δt_j. What we mean to emphasize here is that the Threshold Method provides an alternative means for determining the point at which an event is performed. It is alternative to the standard methods in that it can account for background conditions that fluctuate between the point of sampling a waiting time for an event to be completed and the actual time point at which it is completed. Indeed, in the context of the present model, the Threshold Method is embedded within a larger skeleton of a First Reaction KMC simulation and we will come to this in the following section.

3.5 Description of Cluster Growth Model

Above, we discussed the general principles that account for the methods of Kinetic Monte Carlo simulation employed in the current model. Here we describe how these principles are put into use along with a brief overview of the processes that are implemented into our model. An in depth consideration of the physical processes will be expounded upon in Chapters 4 and 5. The main objective of this model is to simulate the growth of metallic clusters. As such, we focus on the processes that directly involve the clusters themselves. All other processes, while important, are reduced to background effects. While this may seem like a gross simplification, it also allows the model to remain flexible so that it may be applied to various systems. We focus too on neutral cluster growth. At present there are no effects considered that would be due to charge distributions of the environment and to charged clusters.

3.5.1 Static Background Conditions

The 3D space of the physical system essentially gets reduced to a one dimensional discretized space of length L. We refer to a single discrete element of the space as a spatial slice (or slice). All slices are of equal length l with volume V. Any particle species that reside within the slice are assumed to be distributed uniformly throughout the slice. This allows us to discuss a local density of the α particle species as n_α.

We fill each slice with a buffer gas. We will only be interested in the clusters as the objects of the simulation, therefore the buffer gas properties are treated as static

background parameters in each slice. We assume a uniform buffer gas of density n_{g}. The gas is said to move through each slice with a mean or drift velocity, v_{d}.

Another background species added to the system are the sputtered free metal atoms. We do not attempt to model the free metal atoms individually, instead we assume that a balance between the source (sputtering) and drain (diffusion to walls, cluster formation) of free atoms can be accurately modeled by a static, time-independent, density profile. The profile is then discretized by giving each slice a metal density n_{m}. Within any single slice, this density is assumed to be uniform and constant.

3.5.2 Physical Processes

Within this basic environment, we allow a number of physical processes to occur. First among those is the nucleation process (Ch. 5.2) whereby new clusters are generated within each slice based on the local background conditions of that specific slice. These clusters become the objects within the simulation that are subsequently acted upon in the remaining physical processes. The nucleation process is considered to be a Poisson process and therefore the waiting times between successive nucleation events is described by an exponential distribution with a rate λ_N.

A second fundamental process is the movement of clusters between adjacent slices (Ch. 4.7.2). Each cluster is assigned a size-dependent fixed time, $\langle t \rangle$, to make a possible transition to a neighboring slice. Upon moving the cluster, there is a size-dependent probability, p, that the cluster will move forwards, backwards, or stay in its current slice. The exact nature of the transition probabilities and movement intervals is taken from a Lattice Monte Carlo method developed in Ref. [42].

A second transport process is included that allows for clusters to diffuse and stick to the chamber walls (Ch. 4.7.1). This wall diffusion process is size-dependent as well, with smaller clusters diffusing faster than larger ones; it therefore acts as a drain for small clusters. The distribution of times for a wall diffusion event to a occur for a particular cluster size is derived via a convolution of two exponential distributions.

Finally, we have two processes that govern the growth of clusters. First, the atom attachment process is the process where single free metal atoms impinge and stick to the surface of a cluster (Ch. 5.3). The collision process of the free metal atoms with a cluster is also described by a Poisson process. And we have collision times described by an exponential distribution with a rate λ_A. However, in our model, clusters do not increment in size by the addition of just single atoms. Instead, we consider larger jumps between size indices (Ch. 5.1.1). As a result, the waiting times for the completion of the

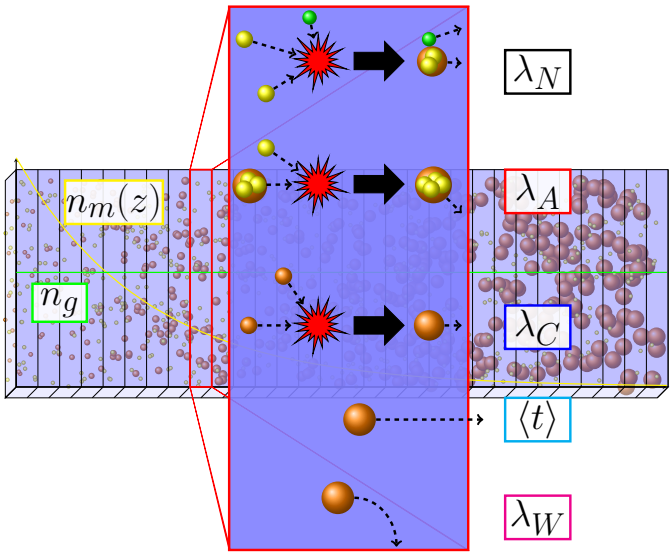

Figure 3.1: Schematic of the cluster growth model. A 1D space is sliced and populated with background densities of gas atoms, n_{g}, and free metal atoms, $n_{\mathrm{m}}(z)$. Within the zoomed slice is a depiction of the included processes (from top): cluster nucleation, atom attachment, coagulation, movement, and wall diffusion.

atom attachment event, with respect to a size index, is given by an Erlang distribution. The second process that relates to cluster growth is the coagulation process where two clusters collide and coalesce to form a single larger cluster (Ch. 5.4). This is another Poisson process and is therefore described by waiting times given by an exponential distribution with a rate λ_C.

Figure 3.1 provides a schematic of the cluster growth model. We have an essentially 1D space, depicted as a thin rectangular block for ease of visualization. The space is divided into a number of slices. Each slice is populated with a background density of buffer gas atoms, n_{g}. The horizontal green line indicates that the gas atom density is constant throughout the space. We also include a background density of free metal atoms, n_{m}. The decaying yellow line indicates a density profile of free metal atoms. In this environment, clusters are nucleated and grow as they move (from left to right) through the system. The zoomed spatial slice shows a depiction of the included physical processes. Starting from the top, we have:

- Nucleation of new clusters
- Free metal atom attachment to an exisiting cluster
- Coagulation of two clusters
- Cluster movement out of the slice
- Cluster diffusion and loss to the chamber walls

3.5.3 KMC Implementation and Algorithm

The KMC method employed in the model is a hybrid of the First Reaction Method and the Threshold Method. First we assign a nucleation event to each spatial slice and sample a time for each slice to produce its first cluster. These times for the nucleation events are then organized in a list and we begin the simulation in a First Reaction fashion, choosing to perform the event with the shortest sampled time. Once clusters are introduced into the system, they are assigned a movement time and are sorted into the list of events accordingly. The simulation proceeds, in this sense, very much like a standard First Reaction algorithm would. We have a list of events that are chronologically ordered. The only events included in the list are the nucleation of clusters and the movement of clusters between slices. To incorporate the remaining processes of atom attachment, coagulation, and wall diffusion, we employ the Threshold KMC algorithm in conjunction with the basic First Reaction procedure described here.

The Threshold method of event performance is used for those events which undergo a change in the rates for event completion due to fluctuating background conditions. The atom attachment process is dependent upon the local free metal atom density which decays when moving forwards through the space. The coagulation process is dependent upon the local cluster density which changes with each slice and (possibly) the cluster's diffusion coefficient which changes as the cluster grows. The wall diffusion process is dependent upon the cluster's diffusion coefficient as well.

There are two key elements involved in the Threshold Method: 1) an original sample which acts as the threshold to be met and 2) a time step with which to calculate the accumulation to the threshold. Upon nucleation, each cluster is given an original sample threshold for each process that utilizes the Threshold Method. This original sampled threshold is composed of a sampled time for the event's completion multiplied by the inverse-mean time for that process using whatever conditions are local to the cluster

at that time. The time step is taken to be given by the movement process itself. In this sense, the movement process acts as an internal time-step for the atom attachment, coagulation, and wall diffusion processes.

With this we can write the general algorithm in outline form:

1. Initialize system and nucleation events in each slice
    a) Set Global time to 0
    b) Sample a time for a nucleation event to occur in each slice
    c) Organize the events chronologically in a list
2. Select the earliest occuring event from the top of the list
3. Perform the selected event
    a) Set Global time equal to selected event's time
    b) If event is nucleation: create a new cluster in the appropriate slice
        i. Initialize new cluster object
        ii. Sample thresholds for atom attachment, cluster coagulation, and wall diffusion
        iii. Set cluster movement time and add to event list
        iv. Resample slice nucleation time and re-insert in event list
    c) If event is cluster movement: move cluster to new slice
        i. Accumulate atom attachment, coagulation, and wall diffusion thresholds
        ii. Perform any events that meet the original sampled thresholds
        iii. Resample thresholds for any events performed
        iv. Move cluster to new slice (remove cluster if new slice is an axial boundary)
        v. Reset cluster movement time and re-insert in event list
4. Check for continuation
    a) If Global time $<$ simulation length: return to 2
    b) If Global time $\geq$ simulation length: exit simulation

Note that within the algorithm outline, if we read the Arabic numerals alone, thus seeing the algorithm in its broadest sense, the algorithm reads much like the First Reaction algorithm. The Threshold Method, as described in Sec. 3.4, is only conjured in 3.c. when a cluster moves and we check if a growth or wall diffusion event is performed. In this sense, the Threshold Method only acts as a subroutine of the movement process to determine when an event is performed. However, for ease of reference, we will use *Threshold Method* to refer to the full algorithm that includes this additional subroutine and *First Reaction Method* will refer to the standard KMC method described in Sec. 3.3.

3.6 Threshold Model Analysis

In this section we offer two modes of analysis in an attempt to justify the validity of the proposed Threshold Model. The first presents a statistical analysis of the method's central claim. We then present results of a comparison of simulations performed with the Threshold Method and with a standard First Reaction Method.

3.6.1 Analysis of Cumulants

The central statement of the Threshold Method is held within the approximate equivalence of a sampled quantity with a summation of terms over many finite intervals,

$$[T \sim k_0 f(t, \{\beta_0\})] \approx \left[T' = \sum_{j=1}^{j_{\max}} k_j \Delta t_j \right]. \tag{3.10}$$

The approximation of the two terms stems from the discretization of the space. Of course, it is possible to make the spatial slices aribitrarily small, and thus we can improve the fidelity of the approximation to within an arbitrarily small margin of error. Therefore, for ease of discussion we will treat the approximation as an equality.

An analysis of Eq. (3.10) can be made by appealing to the cumulants of the distributions involved. Cumulants are an analytical tool for stuyding statistics, similar to moments [43, 44]. The discussion of cumulants begins with the characteristic function, $\phi(t)$, of a distribution which is the Fourier transform of the distribution's probability density function. From the characteristic function, we can define the cumulant generating function, $g(t)$, as the natural logarithm of $\phi(t)$,

$$g(t) = \ln[\phi(t)]. \tag{3.11}$$

The n^{th} cumulant, κ_n, can then be calculated from the cumulant generating function as,

$$\kappa_n = \frac{\partial^n}{\partial t^n}[g(t)]\Big|_{t=0}. \tag{3.12}$$

For example, we look at the atom attachment process. Within our model the atom attachment process is determined by an Erlang distribution, $\text{Erl}(t; \Delta\mathcal{N}, \lambda)$, stemming from the use of a cluster size index. The two parameters carry the physical meanings: $\Delta\mathcal{N}$ is the number of single atom attachments needed to increment the size index, and λ is the mean rate for one of those atoms to impinge on the cluster surface[3]. In accordance with the Threshold algorithm, we have a random variate, $T \sim \text{Erl}(t; \Delta\mathcal{N}, \lambda)$ and scale it by λ. The product λT can then be found to be drawn from the distribution $\text{Erl}(t; \Delta\mathcal{N}, 1)$.

The general Erlang distribution, $\text{Erl}(t; k, \lambda)$, is associated with the characteristic function $\phi(t) = \left(1 - \frac{it}{\lambda}\right)^{-k}$, therefore the scaled distribution's characteristic function is $\phi(t) = (1-it)^{-\Delta\mathcal{N}}$. Continuing the analysis for the sampled component of the atom attachment process, we find,

$$g(t) = \ln[\phi(t)] = \ln\left[(1-it)^{-\Delta\mathcal{N}}\right]. \tag{3.13}$$

And the first cumulant is found to be,

$$\kappa_1 = \frac{\partial}{\partial t}[g(t)]\Big|_{t=0} = i\Delta\mathcal{N}. \tag{3.14}$$

We can continue with calculating other cumulants, but as will be seen, this is unnecessary.

Next we look at the term T' given by the summation. In our model, the movement times are made with a fixed size-dependent interval[4]. We will therefore use a Dirac delta function in the statistical analysis of the cumulants for the T' term. A delta function, $\delta(t-a)$, is associated with the characteristic function $\phi(t) = \mathrm{e}^{ita}$ and the cumulant generating function $g(t) = ita$. Therefore, we take each term in the summation to return a cumulant generating function $g_j(t) = it\lambda_j\Delta t_j$. However, the cumulant generating function that we need to analyze is essentially a sum of random variates (of course, the delta function fixes the value of the variate, but for the analysis we can still consider drawing a number from the distribution). This is where the convenience of starting the analysis with cumulants as opposed to moments in presented. The cumulant generating

[3] For more details on the use of the Erlang distribution for the atom attachment process, see Ch. 5.3.3

[4] For more details on the movement process between slices in our model, see Ch. 4.7.2

function of a sum of random variates, $g_{X+Y}(t)$, is equal to the sum of the generating functions for the individual terms: $g_{X+Y} = g_X(t) + g_Y(t)$. This allows us to write the cumulant generating function for the T' term as,

$$g'(t) = it \sum_{j=1}^{j_{\max}} \lambda_j \Delta t_j, \tag{3.15}$$

and the first cumulant is,

$$\kappa_1' = i \sum_{j=1}^{j_{\max}} \lambda_j \Delta t_j. \tag{3.16}$$

All other cumulants in this case are 0.

Now we can make some statements about Eq. (3.10) by comparing the cumulants obtained from each side of the equation. First, because the movement process occurs in fixed intervals, leaving only one non-zero cumulant for the T' term, the equivalence between T and T' is limited to only the first order. That is, we can only *possibly* say that the Threshold Method captures the appropriate mean. Using the analysis above, Eq. (3.10) can be reduced to the first-order statement: $\kappa_1 = \kappa_1'$ or,

$$\Delta\mathcal{N} = \sum_{j=1}^{j_{\max}} \lambda_j \Delta t_j. \tag{3.17}$$

This is, perhaps, the most general but concise statement we can make with respect to the Threshold Method and the atom attachment process.

We can understand the implications of Eq. (3.17) a bit better if we look at the special case of constant background conditions. In such a case, each λ_j is equivalent to all the others and since we have already stated that movement times are fixed, we can write,

$$\Delta\mathcal{N} = j_{\max} \lambda \Delta t. \tag{3.18}$$

For clarity, again, $j_{\max}$ is the total number of movement steps carried out before the event is performed, Δt is the movement time interval for each step, λ is the rate of single atom attachment, and $\Delta\mathcal{N}$ is the total number of atoms needed to increment the cluster size index by one. With this in mind, the product $j_{\max}\Delta t$ is simply the total movement time. The total time multiplied by the rate for atom attachment returns the number of attachment events, but this is precisely $\Delta\mathcal{N}$. This implies that the Threshold Method does indeed capture the appropriate mean.

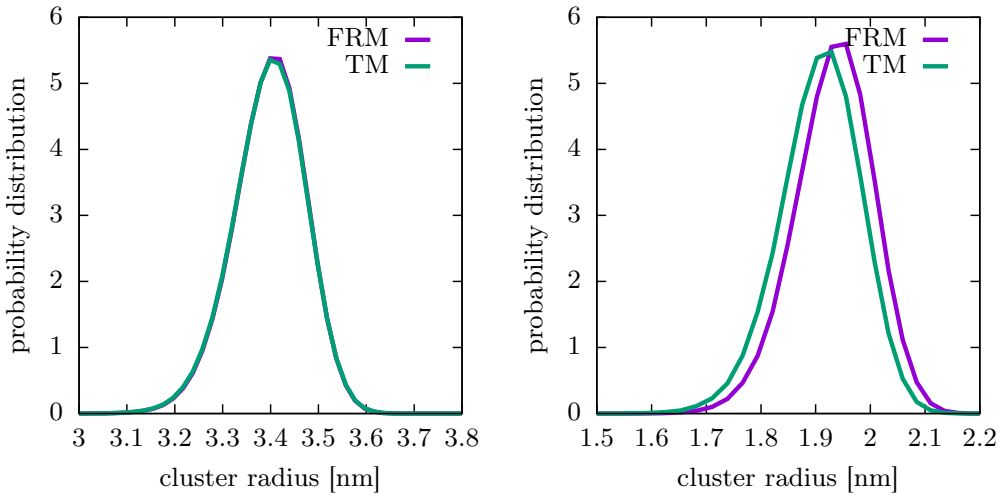

(a) Constant Free Atom Density

(b) Decaying Free Atom Density

Figure 3.2: Comparison of First Reaction and Threshold algorithm for a simple cluster growth case. (a) The size distributions for a constant free atom density are nearly independent of the chosen algorithm. (b) For a decaying free atom density, the First Reaction algorithm yields larger clusters while the Threshold algorithm better preserves the theoretical mean (see Table 3.1)

With this analysis we looked at the specific example of the atom attachment process in the context of the Threshold Method. We found that the central statement of the method, Eq. (3.10), can be reduced to Eq. (3.17) via an analysis of cumulants. This analysis also uncovers the fact that the Threshold Method can only be valid up to the first order, which is equivalent to saying that the method reproduces the appropriate mean time for the event performance.

3.6.2 Comparison of First Reaction and Threshold Methods via Simulation

Here we compare results for simple cluster growth simulations run with the Threshold and First Reaction algorithms. These simulations have clusters generated in only the first slice of the space. Clusters then move through the space with a constant forward drift, such that we can determine the cluster's residence time. We include only the atom attachment process for cluster growth. We then compare the cluster size distributions given by use of a purely First Reaction algorithm and the Threshold algorithm for cases

Method	Constant Density Mean Radius [nm] (% error)	Decaying Density Mean Radius [nm] (% error)
Theoretical	3.404 (0)	1.907 (0)
First Reaction	3.397 (0.2)	1.933 (1.33)
Threshold	3.395 (0.22)	1.908 (0.01)

Table 3.1: Mean radius values for the distributions shown in Fig. 3.2. Both methods faithfully reproduce the expected theoretical values for cluster growth within a constant free metal atom density background, but the Threshold method is much better suited for systems that include an exponentially decaying free atom density.

of a constant free atom density profile and an exponentially decaying free atom density profile. We will also compare the mean values of each distribution to theoretical values for each case.

Figure 3.2 (a) shows the results for the first case of a constant free atom density. The distributions for both algorithms are nearly identical to each other. The Threshold algorithm is transparent with respect to constant background conditions, reproducing results from an algorithm that has been well studied. Still, we may be interested to know if those results are valid with respect to an analytical evaluation. The theoretical mean radius[5], $\langle R \rangle$, for the clusters as a function of the particle position is given by,

$$\langle R(z) \rangle = \frac{1}{3} k_0 r_\mathrm{w} n_\mathrm{m} \frac{z}{v_\mathrm{d}} + R_2, \tag{3.19}$$

where k_0 is a reduced rate constant, r_w is the metal atom radius, n_m is the free metal atom density, v_d is the constant drift velocity, and R_2 is the radius of the nucleated clusters. The center column of Table 3.1 shows a comparison for the value of the mean cluster radius when derived with the above formula (theoretical) and the two algorithms. We see that, indeed, both of our simulations match the expected value with less than 1% error.

Figure 3.2 (b) shows the results for the second case of an exponentially decaying free atom density. First we may note that the cluster sizes for either algorithm are significantly smaller than they were for the constant density case. This is due to the decaying free atom density. The decay of the free atom density reduces the atom attachment rate producing smaller clusters overall. Next we note that the First Reaction algorithm produces larger clusters than the Threshold algorithm. This is because the First Reaction

[5] For details on the derivation of this formula, see Ch. 5.3. In this example we use a change of variables of $t \to \frac{z}{v}$

Method does not take into account the changing background conditions as the cluster moves through the space. In the First Reaction algorithm, a cluster is assigned a definite time for the atom attachment event to occur. It may be that the cluster moves through several slices before the sampled time is reached. But, as it moves through those slices, the cluster does not pick up any information about how the background conditions have changed, effectively the event is performed as if the conditions at the time of sampling are held constant until the event performance. As the free metal atom density is decaying with each movement, thereby slightly reducing the atom attachment rate with each step, we would expect that a correct implementation that accounts for the changing density would result in smaller clusters than those given by the First Reaction algorithm. The Threshold algorithm shows this very trend.

Again, we may wish to check these results against a theoretical value for the mean cluster radius. We take the decaying free metal atom density to be given by $n_{\mathrm{m}}(z) = n_0 \exp[-z\lambda_{\mathrm{m}}]$, where n_0 is the initial density and λ_{m} is a decay constant[6]. Then, similarly to the formula used above for the constant density case, we may find a mean cluster radius produced in a decaying metal atom density profile to be given by,

$$\langle R(z) \rangle = \frac{1}{3} k_0 r_{\mathrm{w}} n_0 \frac{1}{\lambda_{\mathrm{m}} v_{\mathrm{d}}} (1 - \exp[-\lambda_{\mathrm{m}} z]). \tag{3.20}$$

The rightmost column in Table 3.1 shows the mean cluster radius values when calculated with Eq. (3.20) and with our two algorithms. The system is small enough such that the simulated results do not diverge too far from the theoretical values. However, we can clearly see that the Threshold algorithm does a much better job at preserving the theoretical value, with a percent error that is well below 1. The mean radius obtained with the First Reaction algorithm produces an error over 1%.

These results strengthen the validity of our new Threshold Method approach to event performance within a KMC simulation. The complete algorithm is essentially a hybrid of the First Reaction Method, employed to treat cluster nucleation and movement processes, and the Threshold Method, used to treat processes with background parameter dependent rates.

[6] For a more in-depth discussion of the initial density and decay constant for the free atom density, see Ch. 4.6.

Laws of motion of any kind only become comprehensible to man when he can examine arbitrarily selected units of that motion. But at the same time it is this arbitrary division of continuous motion into discontinuous units which give rise to a large proportion of human error.

Leo Tolstoy

CHAPTER 4

Metal Transport Models

The transportation of material through the system is of utmost importance to the overall model. Clearly, it is essential to define the mechanisms for material to move through the system, else we have a completely static system. In this chapter we will look at simple models for metal transport in equilibrium and non-equilibrium cases. We will derive a simple statistical picture involving elastic atomic collisions and show that diffusion emerges naturally with diffusion coefficients that are extracted with limited, but reasonable accuracy. We then switch to diffusive transport models based on statistical solutions to the Smoluchowski equation. With such solutions, we can eliminate the modeling of individual atomic interactions, which would dominate all other processes, and consequently considerably speed-up a computation.

4.1 Background Buffer Gas

An understanding of some basic properties of the background buffer gas is essential to all transport models in the system. We assume that once the sputtered metal atoms come into equilibrium with the buffer gas, they take on the gas' drifting characteristics. Furthermore, as the metal atoms coagulate into larger and larger clusters, they are always assumed to remain in equilibrium with the buffer gas and therefore they too maintain the mean drift velocity.

We assume that the buffer gas is homogenously distributed over the entire mag-

netron cluster chamber and obeys the equation of state for an ideal gas [45],

$$PV = Nk_{\mathrm{B}}T, \tag{4.1}$$

where P is the pressure, V is the volume of the chamber, N is the number of gas atoms, k_{B} is the Boltzmann constant, and T is the system's temperature. In a homogeneous system, the buffer gas mean number density follows as

$$n_{\mathrm{g}} = \frac{N}{V} = \frac{P}{k_{\mathrm{B}}T}. \tag{4.2}$$

The drift velocity of a gas moving through a pipe can be obtained through considerations of the conservation of mass [26, 45]. We look at the cross section of a circular pipe and find the average velocity of a gas molecule through the cross section. Mass should be conserved as follows:

$$\dot{m} = \rho_m \bar{v} A, \tag{4.3}$$

where $\dot{m}$ is the mass flow rate into the pipe, ρ_m is the mass density of the gas, $\bar{v}$ is the average gas velocity through the cross section and A is the cross sectional area of the pipe. The mass density follows from the number density with the introduction of the gas atom mass m_{g}, $\rho_m = \frac{Pm_{\mathrm{g}}}{k_{\mathrm{B}}T}$. An estimation for the drift velocity then becomes,

$$\bar{v} = \frac{\dot{m}k_B T}{m_{\mathrm{g}} P A}. \tag{4.4}$$

The mass flow rate, $\dot{m}$, is obtained through the experimental input parameter of buffer gas flow rate often measured in sccm (standard cubic centimeters per minute). The standard for the cubic centimeter is at 0° C and 1 atm. In SI units this becomes 10^{-6} cubic meters at 273.15 K and 101,325 Pa [46]. Therefore, the number of particles that move through a fixed cross section area in one minute is,

$$N_{\mathrm{sccm}} = \frac{PV}{k_B T} = \frac{101,325 \times 10^{-6}}{1.38 \times 10^{-23} \times 273.15} \approx 2.688 \times 10^{19} \text{ particles}. \tag{4.5}$$

This helps us write the mass flow rate for 1 sccm along with the gas particle mass,

$$\dot{m} = \frac{N_{\mathrm{sccm}} m_{\mathrm{g}}}{60\mathrm{s}} \tag{4.6}$$

As an example of typical buffer gas drift velocities in a magnetron cluster source, we look at typical experimental values [19] for the flow rate of 15 sccm of Ar, a chamber

pressure of 19 Pa, operating temperature of 300 K, and a chamber radius of 5 cm, we find for the drift velocity

$$\bar{v} = \frac{\dot{m} k_B T}{mPA} \approx 18.7\text{cm/s}. \tag{4.7}$$

4.2 Simple Collision Model

In this section we derive a simple, collision-based KMC model. The basic system we look to model is that of a single particle (metal atom or cluster) suspended in a gas of buffer atoms. Particles are assumed to be neutral, so electromagnetic effects are ignored. Gravitational effects are also assumed to be negligible and do not enter the model. The only force acting on the particle then is via the momentum imparted by a collision with the buffer gas background.

We assume the buffer gas has a constant, fixed temperature, and as such acts as a perfect thermal bath for the particle under consideration. The temperature (T) and gas atom mass (m_{g}) define a Maxwell-Boltzmann velocity distribution which the buffer gas adheres to. Likewise the equilibrated metal particle velocity distribution is parametrized by T and the particle mass (M). However, we will not necessarily demand that the metal particles initially be in equilibrium. Large initial velocities are expected for sputtered material, in which case we expect a relaxation time for the metal particles to reach an equilibrated velocity distribution.

The essential parameter to the description of the collisions with the buffer gas is the collision frequency. This is, in general, taken to be,

$$\nu = n_{\text{g}} \varsigma v_{\text{rel}}, \tag{4.8}$$

where n_{g} is the number density of buffer gas atoms, ς is the collision cross section of metal particles with buffer gas atoms, and v_{rel} is the mean relative velocity between the particle and gas atoms. The essential result of each collision is an effective update to the particle velocity. We will only remain interested in the metal particle properties after each collision and ignore any effects on the properties of the buffer gas. This is a reflection of the perfect thermal bath assumption as the buffer gas velocity distribution remains unchanged. In the intervening time between two consecutive collisions (Δt), the particle has a definite fixed velocity vector $\vec{v}$, and we compose a displacement vector as $\vec{d} = \Delta t \vec{v}$.

If we allow that collision events between the metal particle and the surrounding gas atoms are independent of each other, then the statistical nature of these collisions is

described by a Poisson process [47–49], and the waiting time between two consecutive collisions obeys an exponential distribution. As such, we can implement a simple KMC-BKL algorithm [38] to sample a particle's waiting time between successive collisions with the gas. The particle velocity is adjusted with respect to a randomly drawn gas atom velocity and is then displaced to the point of the next collision. We iterate this process and make any appropriate measurements that are relevant to understanding the system, such as recording particle velocities and positions, or recording ensemble's mean velocity.

4.2.1 1D Velocity Evolution

We start by looking at a 1D model of collisions between gas atoms of mass m_{g} and metal particles of mass M. We assume the collisions to be elastic and central, and we ignore effects on the velocity distribution of the gas. We consider the circumstance in which we know the particle masses and initial velocities, and we want to find the resulting velocity for M. Perfectly elastic collisions must obey conservation of energy and momentum:

$$\frac{1}{2}m_{\mathrm{g}}u_0^2 + \frac{1}{2}Mv_0^2 = \frac{1}{2}m_{\mathrm{g}}u^2 + \frac{1}{2}Mv^2, \tag{4.9}$$

$$m_{\mathrm{g}}u_0 + Mv_0 = m_{\mathrm{g}}u + Mv. \tag{4.10}$$

Solving for v, we find a particle velocity after one collision to be

$$v = (1-a)v_0 + au \tag{4.11}$$

where v is the particle's resulting velocity, v_0 is the cluster's initial velocity, u is the gas velocity, and $a = \frac{2m_{\mathrm{g}}}{M+m_{\mathrm{g}}}$.

Iterating this for many collisions we find the velocity after N collisions to be,

$$v(N) = (1-a)^N v_0 + a\sum_{i=1}^{N}(1-a)^{N-i}u_i. \tag{4.12}$$

where u_i is an independent gas velocity associated with the i^{th} collision. Each u_i is a random variate of the background gas velocity drawn from a normal distribution with mean μ and variance $\sigma_{\mathrm{g}}^2 = \frac{k_{\mathrm{B}}T}{m_{\mathrm{g}}}$; $u_i \sim \mathcal{N}[\mu, \sigma_{\mathrm{g}}^2]$.

We can treat the summation in Eq. (4.12) by taking note of two basic rules for the algebra of normal distributions [47]:

1. *Normal linear transform theorem*: $\alpha + \beta\mathcal{N}[\mu, \sigma^2] = \mathcal{N}[\alpha + \beta\mu, \beta^2\sigma^2]$

2. *Normal sum theorem*: $\mathcal{N}[\mu_1, \sigma_1^2] + \mathcal{N}[\mu_2, \sigma_2^2] = \mathcal{N}[\mu_1 + \mu_2, \sigma_1^2 + \sigma_2^2]$

Using the linear transform theorem, we write each term in the sum of Eq. (4.12) as a random variate drawn from a normal distribution,

$$a(1-a)^{N-i}u_i = u_i'(N) \sim \mathcal{N}[a(1-a)^{N-i}\mu, a^2(1-a)^{2(N-i)}\sigma_{\mathrm{g}}^2]. \tag{4.13}$$

This leads to a sum of variates drawn from normal distributions that vary with the number of collisions. The sum can be reduced to a single variate drawn from a single normal distribution with the use of the normal sum theorem,

$$\sum_{i=1}^{N} u_i'(N) = w(N) \sim \mathcal{N}\left[a\mu\sum_{i=1}^{N}(1-a)^{N-i}, a^2\sigma_{\mathrm{g}}^2\sum_{i=1}^{N}(1-a)^{2(N-i)}\right]. \tag{4.14}$$

The sums that survive in the mean and variance of the distribution from which $w(N)$ is drawn are geometric series and can be approximated for large N as

$$a\mu\sum_{i=1}^{N}(1-a)^{N-i} \approx \mu(1-(1-a)^N) \tag{4.15}$$

$$a^2\sigma_{\mathrm{g}}^2\sum_{i=1}^{N}(1-a)^{2(N-i)} \approx \sigma_{\mathrm{M}}^2(1-(1-a)^{2N}), \tag{4.16}$$

where $\sigma_{\mathrm{M}}^2 = \frac{m_{\mathrm{g}}}{M}\sigma_{\mathrm{g}}^2$ is the variance of the metal particle's equilibrated thermal velocity distribution. We make the substitution $b = -\ln(1-a) = \ln\left(\frac{M+m_{\mathrm{g}}}{M-m_{\mathrm{g}}}\right)$. With this we write the particle's velocity evolution as a function of the number of collisions as,

$$v(N) = v_0\mathrm{e}^{-bN} + w(N), \tag{4.17}$$

where $w(N)$ is a random variate of velocity drawn from the normal distribution, $w \sim \mathcal{N}[(1-\mathrm{e}^{-bN})\mu, \sigma_{\mathrm{M}}^2(1-\mathrm{e}^{-2bN})]$. It may be useful to invoke the normal sum theorem again and pull the exponential terms back out of the normal distribution related to $w(N)$,

$$w(N) \sim (1-\mathrm{e}^{-bN})\mu + \sqrt{1-\mathrm{e}^{-2bN}}\mathcal{N}[0, \sigma_{\mathrm{M}}^2]. \tag{4.18}$$

This allows us to view the velocity evolution clearly. We have,

$$v(N) = \mathrm{e}^{-bN}(v_0-\mu) + \mu + \sqrt{1-\mathrm{e}^{-2bN}}v_{\mathrm{M}},\ v_{\mathrm{M}} \sim \mathcal{N}[0, \sigma_{\mathrm{M}}^2] \tag{4.19}$$

The mean velocity of the particle can be identified with a constant drift term, μ, plus an exponentially decaying relative term between the particle's original velocity and the

mean drift of the background gas, $e^{-bN}(v_0 - \mu)$. To this one adds a noise term based on the thermal properties of metal particles in equilibrium.

A quick look at limits shows that for $N = 0$, $v(N)$ returns the original velocity v_0. And for $N \gg 0$, $v(N)$ reduces to a random velocity drawn from the cluster's thermal velocity distribution plus the drift term. That is, given enough collisions the metal particle will come to thermal equilibrium and assume the mean velocity (drift) of the buffer gas.

4.3 Thermalization of Sputtered Atoms

We apply the theory outlined above to the case of highly energetic metal atoms being ejected into a perfect bath of buffer atoms. That is, the buffer gas remains fixed at a constant temperature and metal atom collisions do not affect the gas' velocity distribution. We look to gain some insight into the dynamics of equilibration that the metal atoms undergo. In particular we ask the questions: how long does it take for the atoms to thermalize with the buffer gas and how far do they travel in that time? This abstract model can be used to approximate a very simple sputtering process; one in which the energetic atom number density is much lower than the buffer gas number density such that the rate of gas self-interaction is much higher than the interaction between gas atoms and sputtered atoms. In such a case, the gas would have sufficient time to equalize any deviations from a Maxwell-Boltzmann velocity distribution induced by the collisions with the sputtered atoms. Then we may use these results to gain a first idea about where cluster formation may begin in the magnetron chamber.

4.3.1 Time Domain of Velocity Evolution

In Eq. (4.19), we expressed the velocity of a particle as a function of the collision number, here we look to move that expression into the time domain. We first need to define the collision frequency more precisely. In general we take the collision frequency to be given by Eq. (4.8). We will assume a constant buffer gas density in our model given by $n_g = \frac{P}{k_B T}$. The collision cross section (ς) will be given by the simple hard-sphere model, $\varsigma = \pi(r_1 + r_2)^2$, where r_1 and r_2 are the radii of the two colliding particles under consideration. We take the mean relative velocity to be given by the root mean-squared of the difference between our particle's velocity and the gas background. This is most easily calculated from within the reference frame of the buffer gas where we

have $v' = v - \mu$ and $u' \sim \mathcal{N}[0, \sigma_g^2]$.

$$v_{\text{rel}} = \sqrt{\langle (v' - u')^2 \rangle} = \sqrt{\int_0^\infty (v'^2 - 2v'u' + u'^2) f(u') du'} = \sqrt{v'^2 + \sigma_g^2} \quad (4.20)$$

Our collision frequency is then found to be,

$$\nu = n_g \pi (r_1 + r_2)^2 \sqrt{(v - \mu)^2 + \sigma_g^2} \quad (4.21)$$

We write the collision frequency as a function of the number of N collisions by substituting the mean velocity found in Eq. (4.19),

$$\nu(N) = n_g \pi (r_1 + r_2)^2 \sqrt{(\langle v(N) \rangle - \mu)^2 + \sigma_g^2} \quad (4.22)$$

$$= \nu_f \sqrt{(\frac{v_0 - \mu}{\sigma_g})^2 e^{-2bN} + 1} = \nu_f \sqrt{\alpha e^{-2bN} + 1}, \quad (4.23)$$

where $\nu_f = n_g \pi (r_1 + r_2)^2 \sigma_g$ and $\alpha = \left(\frac{v_0 - \mu}{\sigma_g}\right)^2$

We move the collision frequency into the time domain by substituting $N \to N(t) = \int_0^t \nu(t') dt'$ to obtain an integral equation,

$$\nu(t) = \nu_f \sqrt{\alpha e^{-2b \int_0^t \nu(t') dt'} + 1} \quad (4.24)$$

This can be rewritten as the differential equation,

$$\frac{\nu'(t)}{\nu(t)^2 - \nu_f^2} + b = 0 \quad (4.25)$$

The solution to the differential equation yields,

$$\nu(t) = \nu_f \left[\frac{\nu_0 - \nu_f \tanh(-\nu_f bt)}{\nu_f - \nu_0 \tanh(-\nu_f bt)} \right], \quad (4.26)$$

where $\nu_0 = \nu_f \sqrt{\alpha + 1}$ is the initial collision frequency. Again utilizing the relation between collision number and collision frequency, we integrate to find $N(t)$,

$$N(t) = \frac{1}{b} \left\{ \ln \left[\frac{\nu_f}{\nu_f \cosh(-\nu_f bt) - \nu_0 \sinh(-\nu_f bt)} \right] \right\}. \quad (4.27)$$

For convenience, we define the time dependent term,

$$C(t) = \frac{\nu_f}{\nu_f \cosh(-\nu_f bt) - \nu_0 \sinh(-\nu_f bt)}. \tag{4.28}$$

We then substitute $N(t) = \frac{1}{b}\ln[C(t)]$ into Eq. (4.19) to arrive at a time dependent form of the velocity,

$$v(t) = C(t)(v_0 - \mu) + \mu + \sqrt{1 - C(t)^2}\, v_{\mathrm{M}},\ v_{\mathrm{M}} \sim \mathcal{N}[0, \sigma_{\mathrm{M}}^2] \tag{4.29}$$

As before we can check the limits of this equation for consistency. For $t = 0$, $\cosh(0) = 1$ and $\sinh(0) = 0$ making $C(0) = 1$, and $v(0)$ returns our initial velocity. For $t \to \infty$, $\cosh(t \to \infty) = \infty$ and $\sinh(t \to \infty) = -\infty$ making $C(t \to \infty) = 0$. We can see that the long time limit yields a drift term plus a the random thermal term, as expected.

Note that this analysis is relevant only when we assume that the collision frequency between the particle and gas atoms changes over time, ie when the particles are not in equilibrium with the gas. For the equilibrium case, we have a constant collision frequency which greatly simplifies the calculation of $N(t)$. Namely, $N(t) = \nu t$ which yields a time dependent velocity of,

$$v(t) = \mathrm{e}^{-b\nu t}(v_0 - \mu) + \mu + \sqrt{1 - \mathrm{e}^{-2b\nu t}}\, v_{\mathrm{M}}. \tag{4.30}$$

4.3.2 Sputtered Atom Relaxation Time

In the following we test our simple collision model against the theory outlined above. We take a collection of 200,000 test particles and initialize them all with a high velocity. We then implement a very simple KMC-BKL algorithm with a primary process of collisions between the metal particles and buffer gas atoms. As the system evolves, we look at the mean velocity of the collection and compare it to our theory.

Parameters are taken from typical experimental settings for sputtered metal atoms in a magnetron cluster source [19]. We will assume a buffer gas of argon at 300 K with a constant drift of 19 cm/s. Initial velocities are estimated from initial energies of 15 eV for the sputtered atoms.

Figure 4.1 compares simulation results based on the simple collision model with the analytical results. We look at two systems with the sputtering of (a) copper atoms into a low pressure (19 Pa) environment and (b) silver atoms in a high pressure (200 Pa) environment. In both cases, the analytical results are well fitted to the simulations. The

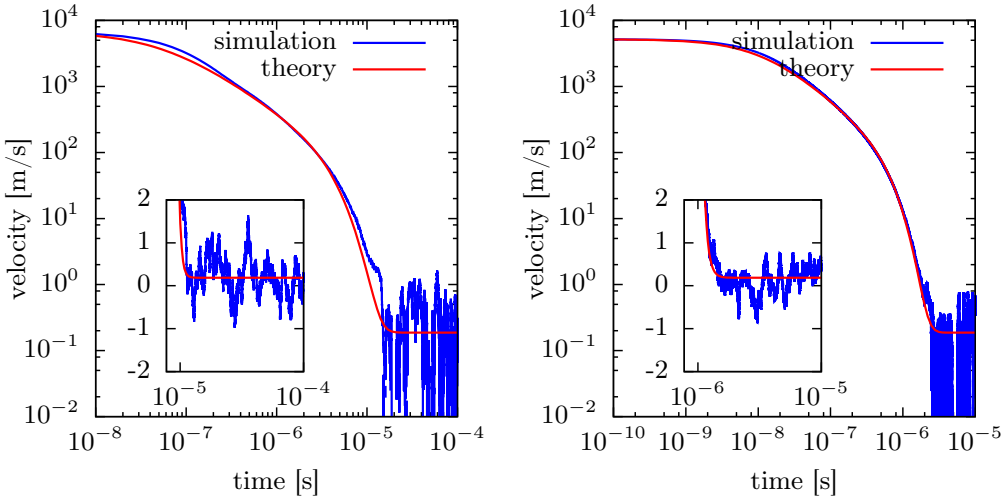

(a) Low pressure Cu

(b) High pressure Ag

Figure 4.1: Theoretical and simulation comparison of velocity relaxation curves. Insets show oscillations around drift velocity with a linear scale

linear scale of the insets better illustrates the fluctuations of the metal velocities around the buffer gas drift. Although the absolute value of those fluctuations are dependent on the number of sampled particles, we can still see that thermal fluctuations are much stronger once the metal reaches equilibrium.

The simulation results compare favorably to the analytical form. We can then utilize the analytic form to gain some more insight into the relaxation of sputtered atoms. Integration of the mean velocity gives us an estimate for how far the sputtered atoms travel into the chamber before coming to thermal equilibrium,

$$\int_0^\tau \langle v(t)\rangle dt = \mu\tau + \frac{2(-v_0+\mu)}{b\sqrt{\nu_f^2-\nu_0^2}}\arctan\left(\frac{-\tanh(b\nu_f\tau/2)\sqrt{\nu_f^2-\nu_0^2}}{\nu_f+\nu_0\tanh(b\nu_f\tau/2)}\right). \tag{4.31}$$

For the case of copper atoms in a low pressure environment, we take $\tau \approx 10\mu$s and the mean distance a metal particle travels before reaching equilibrium is 1.4 mm. For the case of silver atoms sputtered into a high pressure environment, we take $\tau \approx 1\mu$s and the distance traveled is 0.25 mm. This leads to the conclusion that metal atoms may come into thermal equilibrium relatively close to the target. The distance traveled before reaching equilibrium is negligible with respect to a chamber length on the order of 10

cm. It is also relevant to remember that this analysis is made with a 1D model of the sputtered atoms' propagation through the buffer gas where we assume that the initial sputtered atom velocity is perpendicular to the target. For a more complete approach in 3D, we can re-examine Eqs. (4.9) and (4.10) to find a vector form of Eq. (4.30). The addition of the radial dimension could only serve to shorten the distance along the axis at which sputtered atoms come to thermal equilibrium. Therefore, when further developing the model of cluster formation we may take the entire length of the chamber into account and do not limit ourselves to cluster formation in only a portion of the chamber.

4.4 Thermal Equilibrium and Diffusion

The point of this section is to show the extraction of diffusion coefficients that compare reasonably to what is taken to be excepted values for the diffusion coefficients which are based on Chapman-Enskog first approximation model [50, 51]. We take this to reflect on the result from the previous section. While we cannot apply diffusion theory directly to the sputtering of atoms, we hold that the results presented for the relaxation times are still a good first approximation. However, we will also see that the simple collision model results in diffusion coefficients that differ by constant factor from accepted theory for fixed particle masses.

To look into diffusive motion, we will look at a simple picture of a single particle interacting with a buffer background. We will assume that there is no drift within the system. We will use the simple collision model in a KMC simulation to measure the diffusion constants in several ways. If the model is self-consistent and accurately implemented, we should see agreement between our measurements of the diffusion constant regardless of the method employed to find it.

4.4.1 Measurement of Diffusion Constants

Mean Squared Displacement

The mean squared displacement is a measurement of the mean of the squared distance a particle travels in some time interval. It is shown [52] to be related to the diffusion constant by the formula,

$$\langle (x(t) - x(0))^2 \rangle = (2d)Dt, \tag{4.32}$$

where d is the dimensionality of the system, and D is the diffusion coefficient.

First Passage Time

The mean first passage time is a measurement of the mean time it takes a particle to be displaced by a given distance. It is complementary to the mean squared displacement and thus can be related to the diffusion constant by [53, 54],

$$\langle t \rangle = \frac{x_c^2}{(2d)D}, \tag{4.33}$$

where x_c is the critical distance of the measurement.

Velocity Autocorrelation

The velocity autocorrelation function is a measurement of the correlation between a particle's initial velocity and its velocity at some later time. It can be related to the diffusion constant via a Green-Kubo relationship [52],

$$D = \frac{1}{d} \int_0^\infty \langle \vec{v}(0) \cdot \vec{v}(t) \rangle dt \tag{4.34}$$

4.4.2 Theoretical Diffusion Constants

Simple Collision Model

We can use our analytical results of the simple collision model to extract diffusion coefficients via the velocity autocorrelation function. We take the initial velocity v_0 to be given by v_M. That is to say that the initial velocity considered is one that adheres to the metal particle's Maxwell-Boltzmann distribution, $v_0 \sim \mathcal{N}[0, \sigma_\mathrm{M}^2]$. The time dependent velocity is taken from the result presented in Eq. (4.30) but ignoring the drift terms, $v(t) = \mathrm{e}^{-b\nu t} v_0 + \sqrt{1 - \mathrm{e}^{-2b\nu t}} u$, where $u \sim \mathcal{N}[0, \sigma_\mathrm{M}^2]$. Keeping in mind that while u and v_0 are both variates from the same distribution, they are independent of each other.

The velocity autocorrelation function is then,

$$C_v(t) = \langle v(0)v(t)\rangle \tag{4.35}$$
$$= \int_{-\infty}^{\infty} v_0 f_{v_0} dv_0 \int_{-\infty}^{\infty} (\mathrm{e}^{-b\nu t} v_0 + \sqrt{1-\mathrm{e}^{-2b\nu t}} u) f_u du \tag{4.36}$$
$$= \mathrm{e}^{-b\nu t} \int_{-\infty}^{\infty} v_0^2 f_{v_0} dv_0 \tag{4.37}$$
$$= \mathrm{e}^{-b\nu t} \sigma_M^2 \tag{4.38}$$

The diffusion coefficient, D, follows

$$D_{\mathrm{VAF}} = \int_0^{\infty} C_v(t) = \int_0^{\infty} \mathrm{e}^{-b\nu t} \sigma_M^2 = \frac{k_{\mathrm{B}} T}{Mb\nu}. \tag{4.39}$$

It should be noted that the derivation of these diffusion coefficients is dependent on the validity of the assumptions that went into Eq. (4.30). In particular, the approximation of the geometric series encountered in Eq. (4.14) can be seen as a limitation. As such we expect deviations to occur for lighter clusters that do not need to undergo many collisions before $C_v(t)$ sufficiently reaches 0.

Chapman-Enskog First Approximation

The Chapman-Enskog diffusion coefficients are based on a solution to the Boltzmann equation [50, 51, 55]. It is beyond the scope of this work to reproduce the derivation of the coefficients, and we simply state the results as,

$$D_{\mathrm{CE}} = \frac{3\pi}{32} \frac{\bar{v}^2}{\nu} = \frac{3\pi}{32} \frac{8 k_B T}{\pi \mu} \frac{1}{\nu} \tag{4.40}$$

Comparing the two theoretical values of the diffusion coefficients, we find the ratio

$$\frac{D_{CE}}{D_{VAF}} = \frac{3}{2} \frac{1}{a} \ln\left[\frac{1}{1-a}\right] \approx \frac{3}{2}(1 + a/2), \tag{4.41}$$

where $a = \frac{2m_g}{M+m_g} < 1$. For a cases where the medium's atomic mass dominates over the diffusing particle, $M \to 0$, $\frac{D_{CE}}{D_{VAF}} = 3$. More relevant to a magnetron cluster source system, where the diffusing particles are much heavier than atoms composing the medium, $M \to \infty$, and $\frac{D_{CE}}{D_{VAF}} = 3/2$.

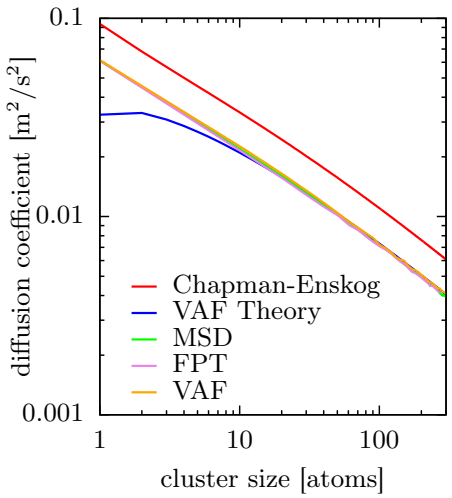

Figure 4.2: Comparisons of diffusion constants. Measurement with the simple collision model of mean square displacement (MSD), mean first passage time (FPT), and the velocity autocorrelation function (VAF) are consistant with each other and differ from the Chapman-Enskog theory by an overall factor. Diffusion constants derived within the theoretical confines of the collision model result in deviations for small cluster sizes.

Figure 4.2 illustrates a comparison between measured values of the diffusion coefficient and theoretical values. We look at a system typical of conditions within the magnetron cluster source. Copper particles constituted by a range of sizes from single atoms up to clusters of hundreds of atoms were placed in argon buffer gas held at a temperature of 300 K and a pressure of 19 Pa. A basic KMC simulation was set up where particles were initialized with a random velocity drawn from the particle's 1D Maxwell-Boltzmann distribution. After each collision event with the buffer gas, the particle's position and velocity were updated. Three independent sets of measurements were made for the mean squared displacement, first passage time, and velocity autocorrelation. In each of the sets a minimum of 10,000 particles were sampled to gain decent statistics. The three curves generated via simulation measurements are consistent with each other. The curve generated from the analysis of the simple collision model shows deviations for smaller particles, as expected due to the approximations made within the analysis. A comparison to the accepted curve of the Chapman-Enskog theory shows that the simple collision model produces diffusion coefficients that are smaller by a factor of 3/2. This result is reasonable considering the simplifactions that went into the

analysis.

4.4.3 Effective Diffusion Coefficients in Arbitrary Mixtures

For the general case of diffusion through a multi-component gas, the above derivation for diffusion coefficients is inadequate. A more appropriate framework for discussion can be found in the generalized Stefan-Maxwell equation [56, 57]. This takes into account mass and mole fractions, pressure and temperature gradients, diffusion velocities, thermal diffusion coefficients, and more. It is beyond the scope of this work to model the full complexities of such a system. We will, however, make use of effective diffusion coefficients that are produced with simplified models that serve as approximate solutions to the Stefan-Maxwell equation. The binary diffusion coefficients above are combined with mole fractions to write an effective diffusion coefficient as,

$$D_{\text{effective}} = \left(\sum_{\alpha} \frac{X_\alpha}{D_\alpha} \right)^{-1} \tag{4.42}$$

where X_α is the mole fraction and D_α is the binary diffusion coefficient with respect to the α species. This effective diffusion coefficient is an approximation for a non-reactive medium. This is something akin to a linear mixture of the species such that the presence of a third species does not affect the diffusion with the second and vice versa.

As an example of how the effective diffusion coefficient may vary with the introduction of a secondary buffer gas species, we look at figure 4.3. In this example we plot the diffusion coefficient for copper atoms in a mixture of Ar and He. We keep the partial pressure of Ar constant at 20 Pa at a temperature of 300 K and see how the effective diffusion coefficient changes with the introduction of He. The addition of any amount of He increases the total pressure in the system, but we still find that the effective diffusion coefficient rises with low partial pressures of He. That is, we may find that the introduction of small amounts of a secondary buffer gas can allow for greater mobility of a third species of diffusing particles. This would be the case if the secondary buffer gas has a lower viscosity than the primary gas, thereby lowering the mixtures viscosity to allow for easier mobility.

4.5 Smoluchowski Equation

In the previous section we showed that the simple collision model can self-consistantly display diffusive behavior. However, the simplifications that went into the model ac-

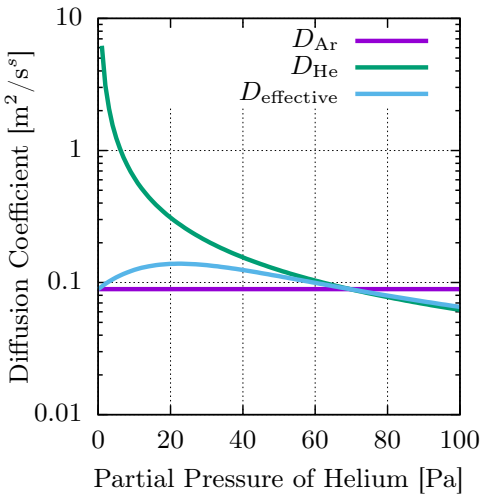

Figure 4.3: Effective diffusion coefficients for Cu atoms in a mixture of He and Ar buffer gas. Ar pressure is held at 20 Pa yielding a constant binary diffusion constant. With an increase of He pressure, the binary diffusion constant of He monotonically decreases. However, the effective diffusion constant of the mixture increases to a maximum at about a He partial pressure of 20 Pa before decreasing.

count for a discrepancy of the diffusion constants that is roughly constant for $M \gg m_g$. To better account for the diffusive motion of particles, we will look for methods of movement that are derived from solutions to well established theory of diffusive motion. The key advantage in this approach is that we may remove explicit buffer gas collision events, and free computation power. We limit our model to cases of homogeneous thermal equilibrium (no temperature gradients) that allow for an overall drifting velocity of the particles. The drift is motivated by a pressure differential through the chamber's orifice.

The base theory comes from the convection diffusion equation

$$\frac{\partial p(\vec{r},t)}{\partial t} = \nabla \cdot (D \nabla p(\vec{r},t)) - \nabla \cdot (\vec{v} p(\vec{r},t)) + R \tag{4.43}$$

where $p(\vec{r},t)$ is the probability for a diffusing particle to be at the position $\vec{r}$ at time t. D is, in general, a position dependent diffusion coefficient, $\vec{v}$ is the drift velocity of the diffusive medium, and R is a source or sink term. For our magnetron systems we take $R = 0$, a constant diffusion coefficient, and assume an incompressible flow($\nabla \cdot \vec{v} = 0$).

The resulting general diffusion equation that we will make use of is then,

$$\frac{\partial p(\vec{r},t)}{\partial t} = D\nabla^2 p(\vec{r},t) - \vec{v}\cdot\nabla p(\vec{r},t). \tag{4.44}$$

This is equivalent to the Smoluchowski equation [58, 59]. A useful limit of the Smoluchowski equation is the case $\vec{v} = 0$, this returns Fick's second law of diffusion. In one dimension we have,

$$\frac{\partial p(z,t)}{\partial t} = D\frac{\partial^2 p(z,t)}{\partial z^2}. \tag{4.45}$$

4.6 Monomer Density Profile Along Chamber Axis

We found in Sec. 4.3 that highly energetic atoms come into thermal equilibrium relatively close to the target. The atoms then diffuse and drift through the magnetron cluster source. The sputtered atoms are then the primary component of a monomer density profile from which clusters are nucleated. This profile is crucial to the overall development of clusters in the system and deserves a close examination. There are several physical processes that feed into the monomer density profile:

- Generation of free atoms from sputtering (sputtering)
- Loss of free atoms due to the nucleation of new clusters (nucleation)
- Loss of free atoms due to attachment to existing clusters (atom attachment)
- Loss of free atoms due to adhesion to chamber walls and boundaries (wall diffusion)
- Addition of free atoms from the evaporation of larger clusters (evaporation)
- Loss of free atoms from the transport out of the chamber along with buffer gas (drift)

Of these items, we consider the three dominant contributions to be: sputtering, drift, and wall diffusion. The remaining are considered to be negligible and thus are ignored in the context of generating a monomer density profile. This can be justified by considering that the nucleation process is slow, requiring a three-body collision. With a low number density of clusters, the atom attachment and evaporation processes cannot significantly contribute to the free atom density, especially when considering the much higer rate of

sputtering. We then look for a steady state solution where the addition of free atoms by sputtering is balanced by the transport of atoms through the system axially and to the chamber walls radially. A static, time-independent, density can then be sought via the Smoluchowski equation.

The time independent Smoluchowski equation with a drift velocity, v, only in the z—direction is

$$v\frac{\partial n(r,z)}{\partial z} = D\nabla^2 n(r,z). \tag{4.46}$$

We can connect the number density $n(\vec{r},t)$ to the probability density $p(\vec{r},t)$ via the normalization conditions

$$\int d^3 r p(\vec{r},t) = 1 \tag{4.47}$$

$$\int d^3 r n(\vec{r},t) = N. \tag{4.48}$$

That is, the number density is simply the probability multiplied by a constant N, the total number of particles. With azimuthal symmetry the general solution can be found by separation of variables [60]. We find

$$n(r,z) = R(r)Z(z) \tag{4.49}$$

$$R(r) = A_r J_0(\sqrt{k/D}r) + B_r Y_0(\sqrt{k/D}r) \tag{4.50}$$

$$Z(z) = A_z \exp\left[-\frac{z}{2D}(-v-\sqrt{v^2+4kD})\right] + B_z \exp\left[-\frac{z}{2D}(-v+\sqrt{v^2+4kD})\right]. \tag{4.51}$$

A few boundary conditions for our system will constrain the form of the density. First, demanding that we maintain a finite density for $r = 0$ means we cannot have contributions from Bessel functions of the second kind and $B_r = 0$. Second, we take the chamber walls to be a perfect absorber of incident atoms so $n(r = R, z) = 0$. This means $J_0(\sqrt{k/D}R) = 0$ and therefore the Bessel function argument, $\sqrt{k/D}R$, must evaluate as a zero of the Bessel function and we have,

$$k_i = \frac{x_i^2 D}{R^2}, \quad \text{where } x_i \in \{x\} := \text{the set of roots of } J_0(x). \tag{4.52}$$

Finally we recognize only the sputtered target, located at $z = 0$, to be the source of free atoms. We cannot, therefore, have a density that increases with z. Because $4kD$ is positive definite, $-v - \sqrt{v^2+4kD} < 0$, and the exponential factor associated with

A_z in $Z(z)$ would escape to infinity. So we must have $A_z = 0$. The limitations of these boundary conditions leaves us with a Fourier-Bessel series for the 2D stationary density [61],

$$n(r,z) = \sum_{i=1}^{\infty} A_i J_0\left(\frac{x_i}{R}r\right) \exp\left[-\frac{vz}{2D}\left(\sqrt{1+\left(\frac{2x_iD}{vR}\right)^2}-1\right)\right], \tag{4.53}$$

where we have collected the integration constants A_r and B_z into the single indexed constant A. The constants A_i are found from considerations of the initial density at $z = 0$,

$$A_i = \frac{2}{R^2 J_1(x_i)^2}\int_0^R n(r,0) J_0\left(\frac{x_i}{R}r\right) r dr. \tag{4.54}$$

For ease of discussion, we will also collect the factors in the exponent as λ_i, that is,

$$\lambda_i = \frac{v}{2D}\left(\sqrt{1+\left(\frac{2x_iD}{vR}\right)^2}-1\right) \tag{4.55}$$

and we write the density simply as

$$n(r,z) = \sum_{i=1}^{\infty} A_i J_0\left(\frac{x_i}{R}r\right) \mathrm{e}^{-\lambda_i z}. \tag{4.56}$$

Before looking at the initial conditions, it would be useful to remark on how this result is utilized in our model. The model we utilize is essentially one-dimensional along the z-axis. We therefore make use of the radially averaged density in place of the fully resolved radial distribution. That is,

$$\bar{n}(z) = \frac{1}{\pi R^2}\int_0^R 2\pi n(r,z) r dr = 2\sum_{i=1}^{\infty}\frac{A_i}{x_i} J_1(x_i)\mathrm{e}^{-\lambda_i z} \tag{4.57}$$

Turning our attention once again to the initial condition, we are interested in knowledge of the initial sputtered density so that we may solve for the constants, A_i. We make the approximation that the sputtered atoms come off the target with an initial velocity in only the z—direction, along the axis of the chamber. Experiments show that sputtering from the target takes place along a ring associated with the so-called racetrack of electons bound to a circular path above the target due to the magnetic field of the magnetron [15]. We will therefore take the initial density to be of the form,

$$n(r,0) = n_0(\Theta(r-a) - \Theta(r-b)), \tag{4.58}$$

where a and b are the inner and outer radii of the ring respectively, and n_0 is the sputtered atom density. We may then find the coefficients to be,

$$A_i = \frac{2n_0}{R^2 J_1(x_i)^2} \int_0^R \left(\Theta(r-a) - \Theta(r-b)\right) J_0\left(\frac{x_i}{R} r\right) r dr \tag{4.59}$$

$$= \frac{2n_0}{R x_i J_1(x_i)^2} \left(b J_1\left(\frac{b}{R} x_i\right) - a J_1\left(\frac{a}{R} x_i\right)\right) \tag{4.60}$$

The parameters a, b, and n_0 can be estimated from experimental considerations. By simply observing and measuring a used target, we can easily get estimations for a and b. The initial density n_0 is estimated by assuming that the sputtered atoms remain along a straight trajectory as they relax towards the drift velocity. Then we may equate the sputtered flux to the drifting flux of atoms. The drifting flux is given by $\Phi_{\text{drift}} = n_0 v$. The sputtered flux is determined by experimental values for the sputtering yield Y and the incident ion current density i, $\Phi_{\text{sputter}} = Yi/e$ [62], where e is the elementary electron charge. This gives us,

$$\Phi_{\text{drift}} = \Phi_{\text{sputter}} \Rightarrow n_0 = \frac{Y \cdot i}{v \cdot e}. \tag{4.61}$$

Pulling everything together we write the monomer density profile along the chamber axis as,

$$\bar{n}(z) = \frac{4Yi}{veR} \sum_{i=1}^{\infty} \frac{b J_1\left(\frac{b}{R} x_i\right) - a J_1\left(\frac{a}{R} x_i\right)}{x_i^2 J_1(x_i)} \mathrm{e}^{-\lambda_i z}. \tag{4.62}$$

We may compare this result with that of the semi-analytic model of cluster formation presented by Smirnov. Smirnov assumes a form of the monomer density profile to be a simple exponential decay, $n^*(z) = n_0^* \mathrm{e}^{-\lambda^* z}$. The model presented above can reproduce this same functional form if we limit the Fourier-Bessel series to the dominant first term. Smirnov then argues for a value of $n_0^* \sim 2 \times 10^{13}$ cm^{-3} and $\lambda^* \sim 1.25$ cm^{-1}. Following the parameters presented in his own estimations we have: $R = 5$ cm, $v = 15$ cm/s. We add some typical experimental parameters for the sputtering of copper atoms: $a = 1.25$ cm, $b = 1.75$ cm, $Y = 1.05$, $i = 1$ mA/cm^2. The resulting value for $\bar{n}(z = 0)$ that the above model would produce limiting the Fourier-Bessel series to just the first term is $\bar{n}(0) \approx 3.66 \times 10^{13}$ cm^{-3}. If we take the first 20 terms of the sum, however, we may find $\bar{n}(0) \approx 2 \times 10^{13}$ cm^{-3}, very much in line with Smirnov's model. Of course, these numbers are only a rough estimation, but it is still encouraging to see two separate analyses producing similar results.

An important point of caution is needed. When we compose $\bar{n}(z)$ from $n(r, z)$, we are losing the radial density profile. This approximation can still be valid provided the

metal atoms' radially diffusive motion is greater than the axial drifting motion. In this case, we would expect a fairly uniform metal atom density filling the whole chamber. However, it may be the case that sputtered atoms maintain a tighter beam, embedded within the space filling buffer gas, where cluster formation may occur. This effect can be parametrized by the Péclet number, $\mathrm{Pe}_{\mathrm{rad}} = vR/2D$. For large values of $\mathrm{Pe}_{\mathrm{rad}}$ the axial drift dominates and we expect a larger density closer to the chamber axis. Conversely when $\mathrm{Pe}_{\mathrm{rad}}$ is small, the radial diffusive motion dominates and our approximation of $\bar{n}(z)$ is validated. The Péclet number can be seen in the expression for the decay parameters λ_i Eq. (4.55). We can see that for very small values of $\mathrm{Pe}_{\mathrm{rad}}$, we may have

$$\lambda_i = \frac{v}{2D}\left(\sqrt{1+\left(\frac{x_i}{\mathrm{Pe}_{\mathrm{rad}}}\right)^2}-1\right) \approx \frac{v}{2D}\left(\frac{x_i}{\mathrm{Pe}_{\mathrm{rad}}}\right) = \frac{x_i}{R}. \tag{4.63}$$

If the radial diffusion is much stronger than the axial drift, then the decay parameters are simply inversely proportional to the chamber's radius.

4.7 Cluster Transport Processes

The transport of clusters through the system will be divided into two independent pieces. First, we have the 2D purely diffusive radial motion that may move clusters to the chamber walls. The wall diffusion process essentially acts as a drain of clusters as the sticking efficiency of clusters with the chamber wall is taken to be 1. Second, we have the 1D convective-diffusive motion along the chamber's axis that transports clusters with a bias towards the orifice, thus exiting the chamber. In each case we take the Smoluchowski equation as the basis of the cluster motion.

4.7.1 2D Radial Diffusion

Clusters are taken to move in a purely diffusive manner in the radial direction. This assumption presupposes a smooth laminar movement of the buffer gas background. That is, there is no turbulent behavior that clusters could get caught in that might otherwise serve as a bias towards the chamber walls. The diffusive radial motion also presupposes the absence of any relative charge difference between the clusters and the chamber walls that might result in a radial force.

We assume that clusters that do manage to come into contact with the chamber walls are absorbed with 100% efficiency. Therefore, the completion of the wall diffusion

process, resulting in attachment to the chamber walls, removes clusters from the system. This makes the radial diffusion process of clusters to the chamber walls unique in that the performance of the event may only occur once for each cluster.

The implementation of this process in KMC requires us to have a distribution of the times for clusters to diffuse to the wall given some initial position. The sample will only be made when the clusters are nucleated. Thereafter, as the clusters move axially, we make updates via the mean time to hit the wall. In each case, we will look for expressions that are derived from first passage time solutions to the Smoluchowski equation.

First Passage Time to the Chamber Walls

The governing equation of a cluster's probability density ($p(r,t)$) is taken to be Fick's second law of diffusion Eq (4.45),

$$\frac{\partial p(r,t)}{\partial t} = D\nabla^2 p(r,t). \tag{4.64}$$

In 2D-polar coordinates with axial symmetry, the general solution for the probability density can easily be found via separation of variables with the separation constant k and constants of integration A and B,

$$p(r,t) = \left\{ AJ_0\left(\sqrt{\frac{k}{D}}r\right) + BY_0\left(\sqrt{\frac{k}{D}}r\right)\right\} \mathrm{e}^{-kt}. \tag{4.65}$$

Here, J_0 and Y_0 are the zero-order Bessel functions of the first and second kind respectively. To this general solution we apply two boundary conditions: (1) we demand finite density at $r = 0$ and (2) cluster loss at the chamber wall leaves $p(r = R, t) = 0$, where R is the radius of the chamber. The first boundary condition forces $B = 0$. The second boundary condition implies that, at the chamber walls, the argument of the Bessel functions are identically zeroes of the function:

$$\sqrt{\frac{k}{D}}R \in \{x_i\} := \text{roots of } J_0(x). \tag{4.66}$$

This means the constant k is indexed as $k_i = \frac{x_i^2 D}{R^2}$; there are an infinite number of solutions and our general solution for the probability density becomes the Fourier-Bessel series,

$$p(r,t) = \sum_{i=1}^{\infty} A_i J_0\left(x_i \frac{r}{R}\right) \mathrm{e}^{-k_i t}. \tag{4.67}$$

The Fourier-Bessel coefficients, A_i, are determined by the initial condition $p(r, t = 0)$ and by exploiting the orthogonality of the Bessel functions over the finite interval,

$$A_i = \frac{2}{R^2 J_1(x_i)^2} \int_0^R p(r,0) J_0\left(x_i \frac{r}{R}\right) r dr \tag{4.68}$$

At the moment we leave the initial probability density undefined and continue towards expressions for the first passage time. First we compose the survival probability. This is the probability of finding a particle within a given region at a particular time. Presently, we want to find the survival probability of remaining within the radial boundaries of the chamber and thus we integrate the density over the cross-sectional area,

$$S(t) = 2\pi \int_0^R p(r,t) r dr \tag{4.69}$$

$$= 2\pi \sum_{i=1}^{\infty} A_i \mathrm{e}^{-k_i t} \int_0^R J_0\left(x_i \frac{r}{R}\right) r dr \tag{4.70}$$

$$= 2\pi \sum_{i=1}^{\infty} A_i \mathrm{e}^{-k_i t} \frac{R^2}{x_i} J_1(x_i) \tag{4.71}$$

The first passage time density $f(t)$, can be found via its relation to the survival probability. The probability that a particle first hits the boundary over some infinitesimally small time interval, dt is equal to the difference in survival probability over the interval $f(t)dt = S(t) - S(t + dt)$. Using a first order Taylor approximation, this can be written as $f(t) = -\frac{dS(t)}{dt}$. Our first passage time distribution is then found to be

$$f(t) = -\frac{dS(t)}{dt} = 2\pi D \sum_{i=1}^{\infty} A_i J_1(x_i) x_i \mathrm{e}^{-k_i t}, \tag{4.72}$$

and the mean first passage time is,

$$\langle t \rangle = \int_0^{\infty} t f(t) dt = 2\pi \frac{R^4}{D} \sum_{i=1}^{\infty} A_i J_1(x_i) \frac{1}{x_i^3}. \tag{4.73}$$

These solutions will be examined for various initial conditions.

FPT Models via Simple Initial Cluster Densities

Turning back now to the initial condition, we will look at a few example cases of initial densities. We introduce the characteristic time $\tau = R^2/D$ as a single parameter in the following analysis.

First, for the oft-used test case of an initial density given by a delta function $p(r,0) = \frac{\delta(r)}{2\pi r}$, we would find

$$A_i = \frac{1}{\pi R^2 J_1(x_i)^2}, \tag{4.74}$$

the first passage time distribution [54] and mean first passage time are given by,

$$f_\delta(t) = \frac{2}{\tau}\sum_{i=1}^{\infty}\frac{x_i}{J_1(x_i)}\mathrm{e}^{-tx_i^2/\tau}, \quad \langle t\rangle_\delta = \frac{\tau}{4}, \tag{4.75}$$

where we have made use of the evaluation $\sum_i^\infty 1/J_1(x_i)x_i^3 = 1/8$. Note the complementary relationship between the mean first passage time and the mean squared displacement, $\langle x^2\rangle = 4Dt$.

A second simple initial density is considered by looking at the general solution of the Fourier-Bessel series. It may be instructive to look at only the fundamental term. In this case the initial density is proportional to $J_0\left(\frac{x_1}{R}r\right)$. The normalized density is found to be

$$p(r,0) = \frac{x_1}{2\pi R^2 J_1(x_1)}J_0\left(\frac{x_1}{R}r\right). \tag{4.76}$$

The Fourier-Bessel coefficients are

$$A_1 = \frac{x_1}{2\pi R^2 J_1(x_1)}, \quad A_{i\neq 1} = 0. \tag{4.77}$$

The first passage time distribution reduces to a simple exponential distribution with a mean given by the inverse of the decay rate,

$$f_{J_0}(t) = \frac{x_1^2}{\tau}\mathrm{e}^{-tx_1^2/\tau}, \quad \langle t\rangle_{J_0} = \frac{\tau}{x_1^2}. \tag{4.78}$$

These are two simple examples of how the first passage time is affected by the initial conditions. As would be expected, the initial spatial distribution of the particle affects when it will first hit the wall and with what sort of distribution of times the particles may take to get there. For a more accurate determination of the first passage times of clusters to the wall, we need to have better knowledge of the density of clusters upon nucleation. The above examples can serve as an approximation of the initial density, but these models can be improved upon as well. As will be discussed in the following chapter, clusters are introduced into the system as two-atom dimers. The formation of these dimers is dependent upon the collision of two free metal atoms. Therefore we expect the initial cluster radial distribution to be proportional to the square of that of the free metal atoms.

Initial Cluster Density via Free Atom Distribution

The free-atom radial distribution is also, in principle, not well established. An approach to a practical distribution for the free atoms starts by examining the Fourier-Bessel series for the general solution of the particle density. Each term of the solution decays exponentially in time, with higher order terms having a higher rate of decay. The particle's diffusion coefficient also contributes to the decay rate with, again, larger coefficients leading to greater rates. Diffusion coefficients decrease with particle size and so we would expect the free-atom density to have the quickest decay to the lowest order term. This harkens back to the caveat at the end of Sec. 4.6. The model implemented for the monomer density profile requires the Péclet number ($\mathrm{Pe}_{\mathrm{rad}} = vR/2D$) to be sufficiently small, then we may safely make the approximation that the free atoms uniformly fill the space. Here, we are interested in the details of the free atom radial profile before we average over the cross-sectional area. The assumption that $\mathrm{Pe}_{\mathrm{rad}}$ is sufficiently small implies that the free-atom radial density is proportional to the fundamental term $J_0(\frac{x_1}{R}r)$. This leads us to a better definition for the initial cluster probability density,

$$p(r,0) = \frac{1}{\pi R^2 J_1(x_1)^2} J_0\left(\frac{x_1}{R}r\right)^2. \tag{4.79}$$

Unfortunately, a closed-form expression for the Fourier-Bessel coefficients cannot be found, and an analytic solution to the first passage time distribution from this initial density is elusive. We can however write general mathematical expressions for the first passage time distribution and mean first passage time,

$$f_{J_0^2}(t) = \frac{1}{\tau}\frac{4}{J_1(x_1)^2}\sum_{i=1}^{\infty}\frac{x_i}{J_1(x_i)}\mathrm{e}^{tx_i^2/\tau}\int_0^1 J_0(x_1\rho)^2 J_0(x_i\rho)\rho d\rho \tag{4.80}$$

$$\langle t\rangle_{J_0^2} = \tau\frac{4}{J_1(x_1)^2}\sum_{i=1}^{\infty}\frac{1}{J_1(x_i)x_i^3}\int_0^1 J_0(x_1\rho)^2 J_0(x_i\rho)\rho d\rho. \tag{4.81}$$

The first passage time distribution associated with an initial cluster density proportional to $J_0(\frac{x_1}{R})^2$ would be the ideal distribution to use for sampling wall diffusion times. This distribution represents an optimal model for the statistics of clusters diffusing to the chamber walls. Finding an efficient implementation of this distribution is, however, not a trivial problem.

With these limitations, the best we may hope for would be an easily implemented approximation to the exact first passage time distribution. Inspired by the general form

of the first passage time as a sum of exponentials, we look at a convolution of exponentials to serve as an approximation of the first passage time distribution derived from an initial cluster density proportional to $J_0(r)^2$. Sampling from a convolution of exponential distributions is easily implemented as a sum of independent samples of the individual distributions. With this simple idea, we can show that a convolution of exponential distributions with rates $k_1 = x_1^2/\tau$ and $k_2 = x_2^2/\tau$ provides for a good approximation to our desired distribution.

A convolution of two distributions picks out the overlap between them. We write this in general as,

$$(f_1 * f_2)(t) = \int_0^t f_1(t')f_2(t-t')dt', \tag{4.82}$$

and we will take $f_\alpha(t) = \lambda_\alpha \mathrm{e}^{-\lambda_\alpha t}$, the exponential distribution. This produces the convolution and mean,

$$f_{\text{conv}}(t) = \frac{1}{\tau}\frac{x_1^2 x_2^2}{x_2^2 - x_1^2}\left(\mathrm{e}^{-t x_1^2/\tau} - \mathrm{e}^{-t x_2^2/\tau}\right), \quad \langle t\rangle_{\text{conv}} = \tau\left(\frac{1}{x_1^2} + \frac{1}{x_2^2}\right). \tag{4.83}$$

Figure 4.4 shows a comparison between the first passage time distributions and the mean first passage times derived from the various initial particle densities. The FPTD associated with the intial density proportional to $J_0(\frac{x_1}{R}r)$ is simply an exponential decay with the lowest available rate and is depicted by a straight line in the chosen log plot. The slope of the line is given by the decay rate, so all lines parallel to this one indicate an exponential decay with a rate of x_1^2/τ. Therefore, the parallel tails in each of the FPTDs indicate that, as expected, the lowest term will eventually dominate the FPTD. A non-zero mode, ie a local maximum, of the FPTD is introduced with the addition of higher order terms. A maximum MFPT is expected for the initial δ density as this is the configuration where a particle is guaranteed to start at a maximal distance from the chamber wall. Also shown in the figure is a comparison between the FPTDs resulting from the J_0^2 initial density and the simple approximation that allows for ease of implementation. The convolution of exponential distributions with rates given by the lowest two terms is a fair approximation to the desired distribution with a percent error in the MFPT of about 5%.

With these results we implement the wall diffusion process in the context of the threshold KMC algorithm. The initial sampled wall diffusion time is taken once at the cluster's nucleation from a convolution of exponential distributions. Each update takes the MFPT of the convolution which conveniently contains a single parameter based on the cluster's current size.

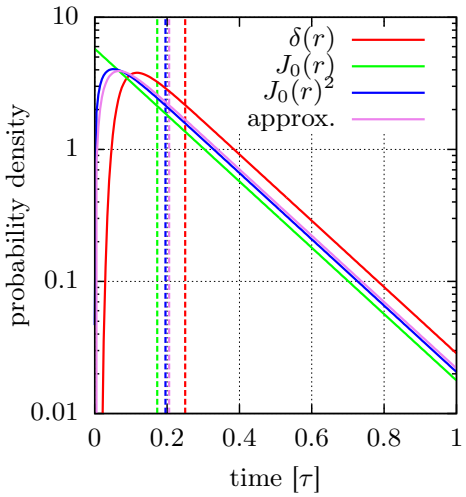

Figure 4.4: First passage time distributions (solid lines) and mean first passage times (dashed lines) for various initial cluster densities are drawn. Results associated with the δ and J_0 densities are analytic solutions representing simplified initial cluster densities. The distribution resulting from the J_0^2 density is the target solution for the model. The approximation to the J_0^2 results from a convolution of exponential distributions with rates x_1^2/τ and x_2^2/τ and allows for ease of implementation.

4.7.2 1D Axial Motion

In the previous section we examined the distribution of times and the mean time for clusters to radially diffuse to the chamber walls. In this section, we are interested in similar quantities for the axial motion of clusters. Under the right circumstances this motion can be easily understood via a constant axial drift velocity. In such cases, we get the trivial solution that the mean time to move a known distance is x_c/v, where x_c is the critical distance under consideration and v is the drift velocity. However, in general we will need to consider the effect of axial diffusion as well. This effect can be characterized by the Péclet number $\text{Pe}_{\text{axial}} = \frac{x_c v}{2D}$, essentially a ratio between the mobilities due to the drift and diffusion. For $\text{Pe}_{\text{axial}} > 1$, the drifting motion dominates the movement process. Conversely for $\text{Pe}_{\text{axial}} < 1$, the diffusive motion is dominant.

In the model description of Chapter 3, we mention that the cluster's movement time operates as an internal time-step for all other processes. It is therefore not an exaggeration to say that the axial motion of the clusters is one of the most crucial points

of the model. We will examine this process critically and ensure that the implementation of the movement process is accurate. To do so, we will draw upon several analyses of the drift-diffusion problem. The individual theories are all rooted in the same problem, but take different approaches to solutions and therefore have various strengths and weaknesses. Together, they serve to validate the approach.

Background to the Drift-Diffusion Problem

We look for first passage time solutions to the 1D drift-diffusion problem via the Smoluchowski equation,

$$\frac{\partial p(x,t)}{\partial t} = D\frac{\partial^2 p(x,t)}{\partial x^2} - v\frac{\partial p(x,t)}{\partial x}. \tag{4.84}$$

An unbounded solution to this problem for an initial distribution of $p(x, t = 0) = \delta(x)$ can be found as,

$$p(x,t) = \frac{1}{\sqrt{4\pi Dt}}\exp\left[-\frac{(x-vt)^2}{4Dt}\right]. \tag{4.85}$$

Of interest for our model, however, is the first passage time to some critical distance, x_c. This places a boundary condition on the general solution. The first passage time solution to the boundary condition, first written by Schrödinger in 1915 [63], yields the well known inverse-Gaussian distribution

$$f_{IG}(t; x_c, D, v) = \frac{x_c}{\sqrt{4\pi Dt^3}}\exp\left(-\frac{(x_c - vt)^2}{4Dt}\right), \tag{4.86}$$

which has the naively expected mean time $\langle t\rangle_{IG} = \frac{x_c}{v}$. That is, on average a particle undergoing drift-diffusive motion will move to a critical point in the same time it takes if the particle were just drifting alone.

However, this solution is not completely well suited to our physical system. The inverse-Gaussian solution allows for a particle to move infinitely in the opposite direction before moving forwards towards the critical point. In the broadest sense, a particle in our physical system sees two boundaries: the orifice from which it exits the system, and the target where it may be re-deposited. In the more accute sense, a particle in our model is located within a spatial slice and we are interested in the movement to an adjecent slice in either the forward or backward direction. While the solutions presented above may still serve to qualify our implementation under appropriate conditions, we should look for solutions to the first passage time problem on a finite interval.

Lattice Monte Carlo Model

A model for the motion of a particle undergoing drifting and diffusive motion has already been developed in the context of Lattice Monte Carlo (LMC) by Gauthier [42]. We implement this solution and make sure that it adheres to other work on the drift-diffusion problem.

Gauthier's basic model has two elements: a mean jump time to move between lattice sites (spatial slices in our model) and a probability to move in either the forward or backward direction. In this model, we do away with the notion of sampling from a full distribution of movement times. Instead, the statistical variation of passage times emerges from the composition of several movement events, each with an independent probability for the direction of movement. It is therefore dependent on the number of slices into which we divide the space.

In Gauthier's basic model, we have the mean movement time given by,

$$\langle t \rangle_{\text{LMC}} = \frac{x_c}{v} \tanh\left(\frac{x_c v}{2D}\right). \tag{4.87}$$

And the relative probabilities to move forward or backward are given by,

$$p_{\pm}(x_c, D, v) = \frac{1}{2} \exp\left(\pm \frac{x_c v}{2D}\right) \operatorname{sech}\left(\frac{x_c v}{2D}\right). \tag{4.88}$$

Note the appearence of the Péclet number in the arguments of each function. We can already gain some insight into the magnitudes of the Péclet number that transition the movement from dominance in drifting or diffusion. Figure 4.5 plots the mean movement time in units of x_c/v and the transition probabilities as functions of the Péclet number. We see that for larger values of Pe, the mean time approaches the simplification of constant drifting motion. Likewise, the backward transition drops to zero, leaving certainty for motion in the forward direction. For small values of Pe, the mean movement time drops towards zero while the transition probabilities each become one-half. That is, as diffusive effects become stronger, the particle may move forwards or backwards with equal probability. Meanwhile, the effect of diffusion shortens the jump time so that particles make more rapid transitions between slices.

Gauthier makes an extension of this basic model to also include a static transition probability; that is, a particle may stay in the same slice over the course of its "move-

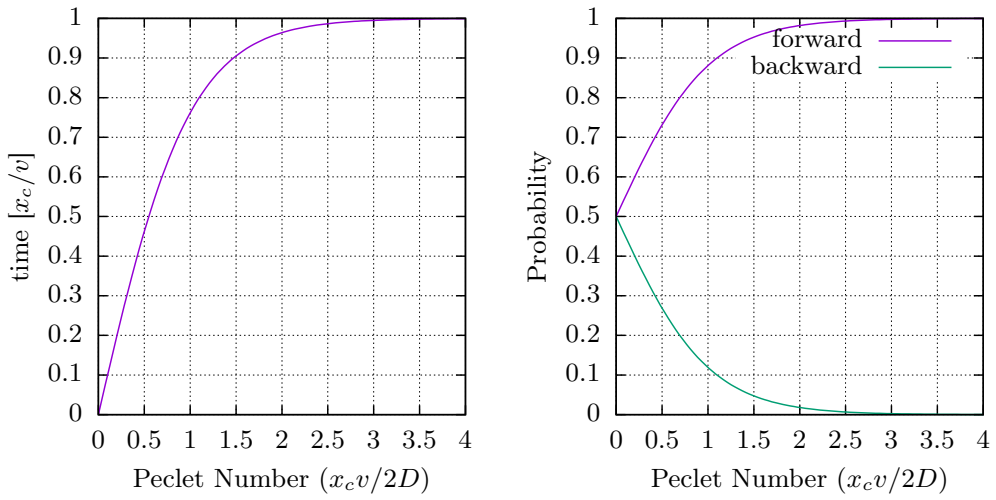

(a) Mean Jump Time

(b) Forward/Backward Probabilities

Figure 4.5: The effects of the Péclet number on the mean movement time and the transition probabilities. Smaller values of Pe indicate a dominance of diffusive motion with faster but equal transitions in either direction. As Pe increases, the effect of the drift takes over eventually resulting in only forward transitions with a time given by x_c/v.

ment" time. This is done with the introduction of the quantity s[1],

$$s = \frac{2D}{x_c v}\coth\left(\frac{x_c v}{2D}\right) - \operatorname{csch}^2\left(\frac{x_c v}{2D}\right) \tag{4.89}$$

The modified mean movement times and transition probabilities take the form,

$$\langle t'\rangle_{\text{LMC}} = \langle t\rangle_{\text{LMC}}(1-s), \quad p'_{\pm}(x_c, D, v) = p_{\pm}(x_c, D, v)(1-s). \tag{4.90}$$

Figure 4.6 shows how the mean transition time and transition probabilities are affected by the addition of a static transition. With the modification, we see that much larger Péclet numbers are needed to ensure a purely drifting motion. But we also can see that, for small Pe, clusters are less likely to move in the backward direction as they were under the forward/backward scheme. Instead, we see that for strong diffusive effects, the addition of a static transition means that particles will most likely remain in their current slice.

[1] The trigonometric function $\operatorname{csch}(x)$ is the hyperbolic cosecant. Similarly to the ordinary trigonometric function, $\csc(x)$, $\operatorname{csch}(x) = 1/\sinh(x)$

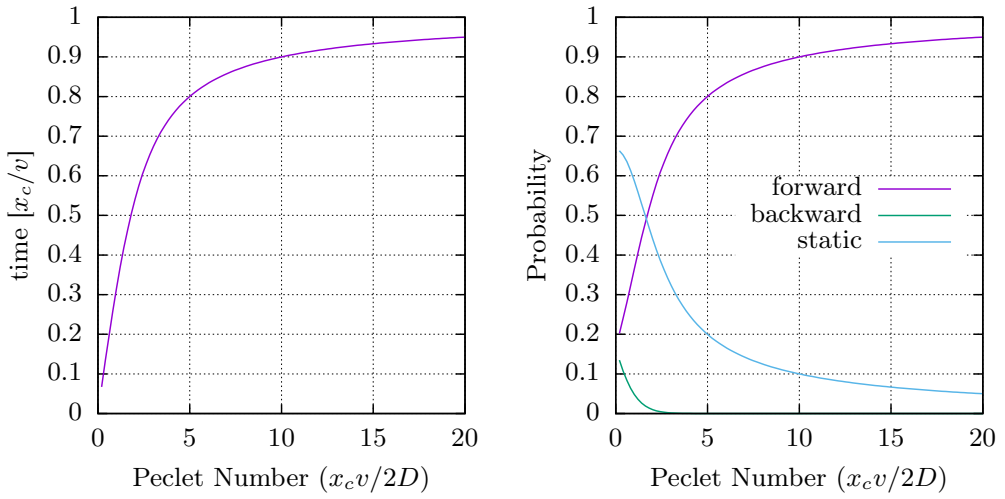

(a) Mean Jump Time

(b) Forward/Backward/Static Probabilities

Figure 4.6: The effects of the Péclet number on the mean movement time and the transition probabilities given the addition of a static transition.

We will continue to implement the modified LMC approach into our KMC model and verify its accuracy. Apart from testing the approach for accuracy, we must also look for limitations induced by the number of slices that we put into the space. The implementation with respect to movement alone is straightforwad and is essentially a form of First Reaction KMC:

1. Initialize: a particle is initialized into a spatial slice.

2. Set movement: the particle's size sets its diffusion constant (D); together with the buffer drift velocity (v) and the slice width (x_c), we set the time for the particle to make a transition using $\langle t' \rangle_{\text{LMC}}$.

3. Sample direction: draw a random number (P) from a uniform distribution. Forward motion is chosen for $P <= p'_+$, Backward motion for $p'_+ < P <= p'_-$, and no movement for $P > p'_+ + p'_-$

4. List: store the particle according to movement times

5. Select: move the first particle in the list according to its sampled direction

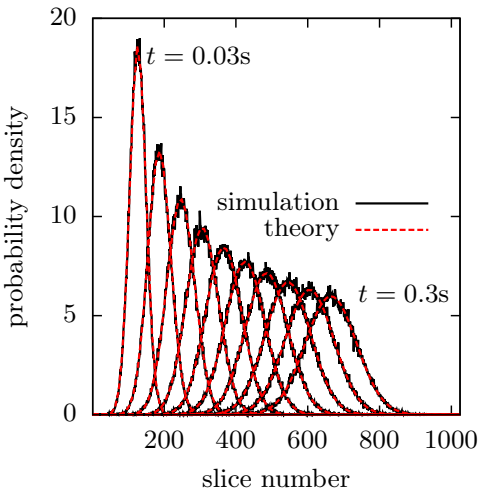

Figure 4.7: Movement on a (nearly) infinite interval. Plotted is a comparison between the modified LMC model and the unbounded solution of the Smoluchowski equation for large particles with Pe ≈ 15. The model is able to reproduce results for a freely moving particle with no boundary condition

6. Return to (2)

With this scheme we cannot arbitrarily initialize any number of particles at once because all particles of the same size would have the same transition time, and we would not be able to properly compose a list. This problem is naturally circumvented because each cluster will be nucleated at varying times and should not present a problem when ordering the list.

Figure 4.7 shows a comparison between the modified LMC model and the unrestricted solution to the Smoluchowski equation. If we move the axial boundaries of the chamber far away, then we should be able to observe a particle that moves in accordance with Eq. (4.85). Even though each individual movement is made via considerations of a solution on a finite interval, the composition of many movements taken together generates the behavior of the general solution. Indeed, we find that the modified LMC model can accurately represent the free solution of the Smoluchowski equation.

Figure 4.8 gives a visualization for how particles move over a finite interval. We plot the number of particles in each spatial slice over several increments of time. Particles are initialized at the center of 128 slices and then allowed to move under the modified LMC

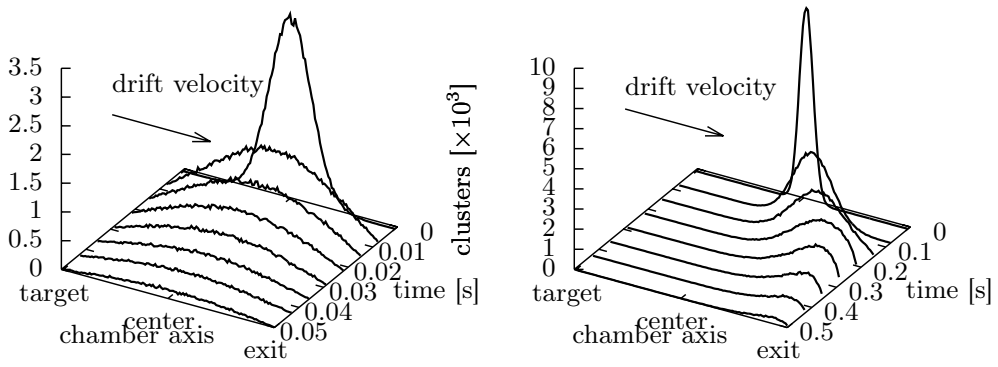

Figure 4.8: Movement on a finite interval. Plotted is a visualization of the time dependence for particle loss on a finite interval. (Left) For Pe ≈ 0.15, particles move both forwards and backwards maintaining a high probability to remain in the center. (Right) for larger Pe ≈ 15, particles tend toward the forward direction where they eventually exit from the chamber's orifice.

scheme. For small Péclet numbers, left plot, we see that the largest number of particles at any given time is found in the center. This indicates that particles are lost equally via a forward drift towards the exit and by diffusing backwards towards the target. For large Péclet number, right plot, the peak particle count moves in the drifting direction and are essentially all lost when they reach the chamber's exit.

Analysis of Motion on a Finite Interval

We turn now to checking our implementation of the modified LMC model against two additional analyses of first passage times on a finite interval. As mentioned earlier, the LMC model does not invoke a reference to any distribution of times. Instead the statistics of first passage times emerge from the transition probabilities. Guo's investigations of the first passage time problem lead to an explicit solution for the distribution of first passage times [64]. These solutions assume an initial condition of a particle starting at the center of the interval $(0, 2x_c)$. The first passage time distribution is shown to be

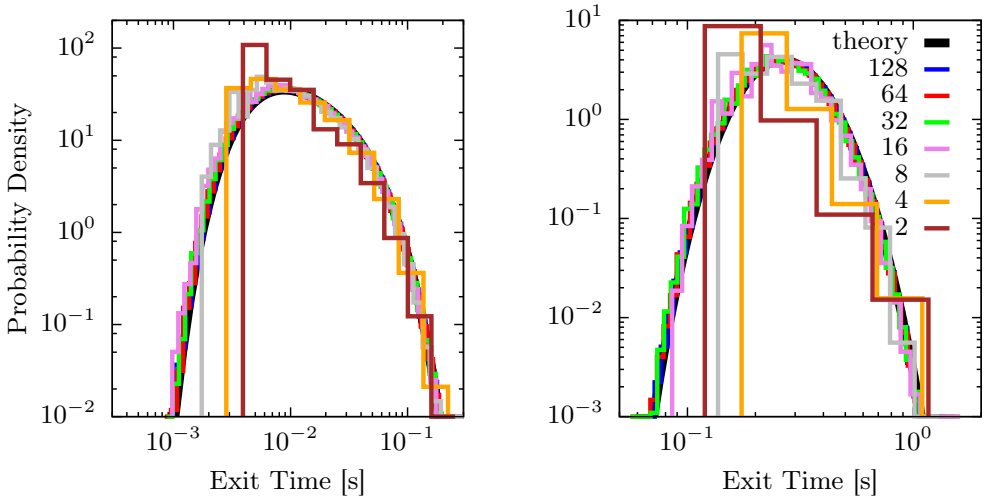

(a) Pe ≈ 0.16 (b) Pe ≈ 15

Figure 4.9: Forward exit time distributions from the center of a finite interval for Pe ≈ 0.16 (a) and Pe ≈ 15 (b). For both large and small Péclet numbers, we see a fair reproduction of the theoretical curve for 16 or more spatial slices spanning the interval. Fewer spatial slices produce larger deviations from theory.

given by

$$f_{\text{Guo}}(t; x_c, D, v) = \frac{\pi D}{x_c^2} \cosh\left(\frac{v x_c}{2D}\right) \sum_{n=1}^{\infty} n \sin\left(\frac{n\pi}{2}\right) \exp\left(-\frac{tD}{x_c^2}\left[\left(\frac{n\pi}{2}\right)^2 + \left(\frac{v x_c}{2D}\right)^2\right]\right) \tag{4.91}$$

Interestingly, the distribution of exit times in the forward and backward directions are equivalent [2] That is, even for high values of Pe, where we expect with near certainty that particles will move in the forward direction, we can also anticipate that particles that do move backwards will reach the boundary with the same distribution of times. Of course, in that case, the ratio of the absolute number of particles exiting an interval in the backward direction to the forward direction will be very low.

We take the first passage time distribution derived by Guo as a benchmark for setting the number of slices in the system. It is reasonable to expect that dividing the space into more slices, thereby increasing the resolution of the movement process,

[2] The expressions in Ref. [64] for the forward and backward distributions, show a slightly different form, but they are not normalized to 1. After normalizing each distribution, we can see their equivalence.

slices	$Pe \approx 0.16$ Mean(% error)	$Pe \approx 15$ Mean(% error)
Analytic	0.0264142 (0.000)	0.321678 (0.000)
2	0.0195549 (25.97)	0.214431 (33.34)
4	0.0225385 (14.67)	0.257327 (20.00)
8	0.0243453 (7.832)	0.285919 (11.12)
16	0.0253338 (4.090)	0.302799 (5.869)
32	0.0258848 (2.004)	0.311951 (3.024)
64	0.0261452 (1.019)	0.316703 (1.546)
128	0.0262997 (0.434)	0.319080 (0.808)

Table 4.1: Complementary to the data presented in figure 4.9, we tabulate the mean exit time from the center of a finite interval with respect to the number of spatial slices spanning the interval. Low resolution produces large errors in the mean exit time. As we increase the resolution, we decrease the generated error. At 64 total slices, the error is about 1%.

would provide for more accurate statistics of the first passage time distribution. However, an increased resolution also increases the number of computational steps that are needed to represent particle motion. In seeking to optimize the computation, we look for the minimal number of slices that are needed in order to reproduce the analysis given by Guo with low error.

Figure 4.9 and Table 4.1 help us make this determination. Data is collected for the exit times in the forward direction of particles that are initialized at the center of a finite interval. We start with two slices, where a particle only needs to make one forward movement in order to reach the exit, and double the number of total slices for each successive run. Figure 4.9 illustrates the convergence of the forward first passage time distribution generated by the LMC model towards the analytical solution with respect to the number of slices for both low and high Pe cases. We see that in both plots, a low number of slices produces large deviations from Guo's analysis. The effect is exaggerated with large values of Pe because particles are more likely to move in only the forward direction, thereby taking fewer movement events to reach the exit and skewing the distribution towards faster exit times. For lower values of Pe, the dominance of the static movement event allows particles to remain in the system longer and assists a better trace of the expected distribution. Table 4.1 complements Fig. 4.9 with a numerical comparison. With fewer slices in the system, the mean exit time is skewed towards faster exit times. A percent error of about 30% is seen for both high and low Pe with

only 2 slices. Doubling the number of slices (very) roughly halves the percent error such that by 64 slices the percent error is down to about 1%.

In the work of Gauthier and Guo, solutions to the first passage time problem were presented with initial conditions limited to initialization at the midpoint of a finite interval. With respect to the comparison above, we may be led to believe that we require many spatial slices over any arbitrary interval in order to resolve the correct first passage time statistics. With 128 spatial slices, we saw good agreement to the first passage time distribution starting at the center of the space where particles needed to make a minimum of 64 forward movements before reaching the exit. Now we ask, can we still achieve good statistics if the particle were placed closer to the exit, thereby needing fewer forward movements in order to exit the system?

The work of Redner can then be used as another means of verifying the LMC model. Redner finds a general solution to the mean first passage time given an arbitrary starting point [53]. Here, the finite interval is over $(0, 2x_c)$ with an arbitrary initial position of $0 < x_0 < 2x_c$. Redner finds the mean first passage time in the forward direction to be given by,

$$\langle t(x_0)\rangle = \frac{2x_c}{v}\frac{1+\exp(-\frac{v2x_c}{D})}{1-\exp(-\frac{v2x_c}{D})} - \frac{x_0}{v}\frac{1+\exp(-\frac{vx_0}{D})}{1-\exp(-\frac{vx_0}{D})} \tag{4.92}$$

Figure 4.10 shows a comparison of the LMC model with initial positions taken arbitrarily within the interval. As expected, we see that for large Pe the theoretical mean exit time is consistent with the simple approach with a constant drifting velocity. A low Pe, meaning greater diffusive mobility, correlates to faster exit times. With 128 spatial slices, we see very good agreement with the expected mean exit time regardless of where the particles are initialized. The 8-slice model, produces mean exit times that are, again, skewed towards faster emission.

In summary, we have implemented the modified LMC model presented in the work of Gauthier. This model has particles moving with a size-dependent jump time between spatial slices. As a result of each jump, the particle may move forwards, backwards, or it may stay in its current spatial slice. We then examined the implementation of the model against various known analyses of the first passage time problem. In each comparison we find that the LMC model can reproduce accurate statistics. The errors in movement times, introduced by discretizing the space into a lattice, can be kept below 1% by using 128 spatial slices over a typical magnetron chamber length of 12 cm.

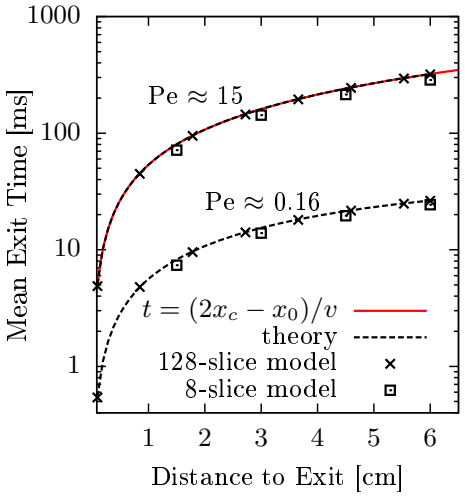

Figure 4.10: Mean forward exit times with respect to an initial position along a finite interval. Data shown for 128 and 8 spatial slices and Péclet numbers Pe ≈ 0.16 and Pe ≈ 15. Large Péclet numbers maintain mean times consistent with a constant velocity motion. The 128-slice model maintains accurate mean values, in both Pe regimes, even for short distances.

Growth is never by mere chance; it is the result of forces working together.

James Cash Penney

CHAPTER 5

Cluster Growth Mechanisms

In this chapter we will explore the key processes that directly relate to the growth of metal clusters. We show how these proccesses can be realized in a KMC setting and illustrate some basic results and restrictions of their implementation.

The entire growth process is viewed to be composed of three essential processes: nucleation, atom attachment, and cluster coagulation[7]. The nucleation process marks the beginning of cluster formation as new clusters are formed out of a supersaturated gas of free metal atoms [7, 27, 65]. Atom attachment is the fundamental method of cluster growth whereby single free atoms adhere to the surface of an existing cluster [7, 8]. Finally cluster coagulation is the process by which two clusters may collide and fuse to form a single larger cluster.

5.1 Properties of Clusters

As a precursor to discussing the growth processes, we should look at relevant physical properties. Within the context of the model at hand, all physical properties of clusters are essentially functions of its size in atoms (N). However, the framework within which we treat the cluster size can give rise to different physical pictures. We utilize two competing frameworks (the liquid-drop and hard-sphere models [7]) and, somewhat arbitrarily, invoke their consequences at our convenience for describing a particular property.

Let us first define what we mean by "cluster". A cluster is a stable, bound collection of metal atoms. A cluster's stability and binding energy allow us to consider each cluster as a single particle [29]. For our purposes we will restrict our definition to particles with extensions in each spatial direction on the order of nanometers. With such a definition, we may consider a cluster to contain up to 10^7 metal, but typically much less. Also, we will often use the term "dimer" to refer to a cluster composed of just two atoms.

The cluster mass is perhaps the most straightforward property to define and is independent of either the liquid-drop or hard-sphere models. We define it simply to be the total mass of the N atoms composing the cluster [7]. Let the atomic mass of a single metal atom to be given by m_{m}, ignoring the effects of binding energies, we write the mass of a cluster of N atoms as,

$$M_N = N m_{\mathrm{m}}. \tag{5.1}$$

The definition of the cluster radius is given within the framework of the liquid-drop model [7]. Here we assume that clusters of size N are spherical liquid-like drops of constant density with a radius (R_N) that preserves the total atomic volume of the N atoms in the cluster. The radius of a single metal atom is taken to be defined by the Wigner-Seitz radius, r_{w}. The atomic volume is taken to be that of the corresponding sphere, $\frac{4}{3}\pi r_{\mathrm{w}}^3$. The liquid drop model then gives,

$$N\frac{4}{3}\pi r_{\mathrm{w}}^3 = \frac{4}{3}\pi R_N^3, \quad R_N = r_{\mathrm{w}} N^{1/3}. \tag{5.2}$$

The liquid-drop model contrasts the use of the hard-sphere model which is invoked when describing cluster collision processes [7]. Clusters and metal atoms are conveniently modeled as solid spheres with a radius given by the liquid drop model. Gas atoms are described as solid spheres as well, but via their Van der Waals radius r_{g}. From this, we have collision cross sections that take the simple geometric form,

$$\varsigma_{ij} = \pi(r_i + r_j)^2, \tag{5.3}$$

where i and j may refer to any particle species.

Relative velocities are defined via the 3D Maxwell-Boltzmann velocity distributions for two particle species (i, j) in thermal equilibrium. We have,

$$\langle v \rangle_{ij} = \sqrt{\frac{8 k_{\mathrm{B}} T}{\pi \mu_{ij}}}, \tag{5.4}$$

where $\mu_{ij} = \frac{m_i m_j}{m_i + m_j}$ is the reduced mass of the two species under consideration.

Collision frequencies are fundamental to rates of growth processes in the model. The general two-body collision frequency for a particular member of species i with some member of species j is,

$$\nu_{ij} = n_j \kappa_{ij}. \tag{5.5}$$

Here, κ_{ij} is the coagulation kernel and can take different forms depending on the nature of how one cluster approaches another. Often, the cluster approach is taken to either be diffusive or kinetic in nature and each leads to very different coagulation kernels.

5.1.1 Cluster Size Indices

The key purpose of the present KMC program is to simulate the growth of clusters from their nucleation to their emission from the cluster chamber. The growth is quantified via the discrete number of atoms in each cluster (N) starting with the dimer. During a cluster's lifetime in the chamber it may grow to contain tens of thousands of atoms. Single atom attachment is assumed to be the most basic and fundamental growth mechanism. If we resolve each additional atom attachment, we would anticipate needing a very large number of calculation steps to realize each cluster. In the interest of keeping the run times of the program managable, we look for ways of simulating selected sizes of clusters rather than resolving the entire spectrum of sizes. To do this we introduce a cluster size index.

A size index is a set of sequential cluster sizes with an arbitrary number of elements, $\mathcal{S} = N_i, N_{i+1}, N_{i+2}, \ldots, N_{i+j}$. We say that each $N_i \in \mathcal{S}$ is represented by the size index.

The relation of the size index to the actual cluster sizes can be completely arbitrary. Here we focus on one family of relations that is shown to be flexible and accurate. The general form of the smallest cluster size in the index (i) is given by $i^p + 2$. If we want to return integer values, we could restrict p to integer values as well. However, to maintain greater flexibility, we will allow p to be any real number by taking only the floor value. We then define the smallest cluster size ($\mathcal{N}$)[1] in an index as,

$$\mathcal{N}_i = \lfloor i^p + 2 \rfloor. \tag{5.6}$$

[1] A word on the chosen notation. The italicized N represents a cluster's number of atoms without any reference to an index. The caligraphic $\mathcal{N}_i$ denotes the number of atoms in the smallest cluster that's represented within the index i.

To prevent multiple indices from evaluating to the same $\mathcal{N}$ we require $p \geq 1$. This is a natural restriction too in the sense that a value of $p = 1$ will lead to $\mathcal{N}$ simply reflecting the number of atoms in each cluster. We then say that $p = 1$ returns to the full spectrum of cluster sizes, and increasing p decreases the resolution of the simulated size spectrum.

Other useful properties of the size index are the number of cluster sizes ($\Delta\mathcal{N}$) from the full size spectrum that is capturued within a single index,

$$\Delta\mathcal{N}_i = \mathcal{N}_{i+1} - \mathcal{N}_i. \tag{5.7}$$

This is important in Sec. 5.3.3 when considering the growth from one size index to the next via atom attachment. The transition from index i to $i + 1$ needs to capture the additon of $\Delta\mathcal{N}_i$ atoms. Physical properties of size indices (mass, radius, collision frequencies, etc.) are given by the median cluster size in a size index,

$$\mathcal{M}_i = \mathcal{N}_i + \frac{\Delta\mathcal{N}_i - 1}{2} = \frac{1}{2}(\mathcal{N}_{i+1} + \mathcal{N}_i - 1) \tag{5.8}$$

Table 5.1 compares the properties of several size index schemes. For $p = 1$ we resolve the full spectrum of cluster size with each index representing just one cluster size. For integer values of p we see a monotonic increase of $\Delta\mathcal{N}_i$. With half-integer values of p, and the use of the floor function, we may have $\Delta\mathcal{N}_{i+1} < \Delta\mathcal{N}_i$. It may be interesting to note that this family of size index schemes always provides for a unique size index to be allocated to our smallest clusters, the dimers.

5.2 Nucleation

The nucleation process adds new clusters into the system and thus marks the beginning of the entire cluster growth process. The model assumes that clusters are formed via the three-body collision of two metal atoms and a buffer gas atom.

$$M + M + G \Rightarrow M_2 + G \tag{5.9}$$

The resultant is a two-particle bound state, dimer, plus a gas atom with high kinetic energy. The gas atom's role in the collision is to absorb excess energy allowing the dimer to be stable. Some authors [30] envision this process in two stages of two-body collisions. The first involves the collision of two metal atoms to form a metastable bounded dimer. Then a subsequent collision of the metastable dimer with a buffer gas atom that effectively removes energy from the bounded pair leaving a stable state.

$$M + M \Rightarrow M_2^*, \quad M_2^* + G \Rightarrow M_2 + G. \tag{5.10}$$

Table 5.1: Size index examples: Basic parameters for several size index schemes in the family $\mathcal{N}_i = \lfloor i^p + 2 \rfloor$. For $p = 1$ we simulate the complete range of cluster sizes. Increasing p reduces the simulated resolution. Cluster properties for a size index are given by the median cluster size, $\mathcal{M}_i$.

$p \rightarrow$	1			1.5			2			3		
i	$\mathcal{N}_i$	$\Delta\mathcal{N}_i$	$\mathcal{M}_i$	$\mathcal{N}_i$	$\Delta\mathcal{N}_i$	$\mathcal{M}_i$	$\mathcal{N}_i$	$\Delta\mathcal{N}_i$	$\mathcal{M}_i$	$\mathcal{N}_i$	$\Delta\mathcal{N}_i$	$\mathcal{M}_i$
0	2	1	2	2	1	2	2	1	2	2	1	2
1	3	1	3	3	1	3	3	3	4	3	7	6
2	4	1	4	4	3	5	6	5	8	10	19	19
3	5	1	5	7	3	8	11	7	14	29	37	47
4	6	1	6	10	3	11	18	9	22	66	61	96
5	7	1	7	13	3	14	27	11	32	127	91	172
6	8	1	8	16	4	17.5	38	13	44	218	127	281
7	9	1	9	20	4	21.5	51	15	58	345	169	429
8	10	1	10	24	5	26	66	17	74	514	217	622
9	11	1	11	29	4	30.5	83	19	92	731	271	866

This second picture provides more degrees of freedom and may be a more accurate physical description than what is modeled. However, this would then entail an additional process to be considered for the breaking of metastable bonds. As we place primary concern in the stable formation of dimers, we ignore any effects of metastable dimers. The single three-body process is then viewed as an ensemble average of the coupled two-body processes, which allows us to focus only on the resulting stable dimers.

The rate for dimer formation neglecting losses due to decay mechanisms, transport out of the volume, and consumption through further growth processes is written as [7, 15, 27],

$$\frac{\mathrm{d}n_\mathrm{d}}{\mathrm{d}t} = K n_\mathrm{m}^2 n_\mathrm{g}, \tag{5.11}$$

where n_d is the number density of dimers. Since we do not directly simulate any of the particles involved, this process is modeled volumetrically in each slice with a rate,

$$\lambda_\mathrm{nuc} = K n_\mathrm{m}^2 n_\mathrm{g} V \tag{5.12}$$

where K is a three-body collision constant. That is, prior to the addition of any clusters in the system, the simulation contains only local (with respect to spatial slices) densities of the buffer gas and the free metal atoms. Then, we add the cluster objects into the system with a time-point sampled from the exponential distribution with a rate parameter

λ_{nuc}. Each spatial slice in the simulation has its own local density and nucleation occurs within each slice independently of the others.

With the use of the nucleation rate we can estimate an upper bound for the cluster density with the system. If we allow the most basic processes of cluster nucleation and cluster movement, without involving cluster growth or loss of clusters to wall diffusion, then the number of clusters (N_{c}) in the system can be found in the balance equation,

$$\frac{\mathrm{d}N_{\text{c}}}{\mathrm{d}t} = \lambda_{\text{nuc}} - \lambda_{\text{move}}, \tag{5.13}$$

where λ_{move} is the rate for clusters to leave the system. We take λ_{move} to be $N_{\text{c}}\frac{2\bar{v}}{L}$, where $\bar{v}$ is the drift velocity of the buffer gas and L is the length of the chamber. This definition of λ_{move} states that, on average, we can consider that clusters drift towards the orifice as though they were nucleated at the axial midpoint of the chamber. This is clearly an oversimplification, as we have already seen that small clusters may move much faster than the drift velocity, however it is well-suited for an upper bound estimation of the cluster density.

To evaluate the balance equation in the stationary case, we want the left-hand side to be zero and we have,

$$\lambda_{\text{nuc}} = \lambda_{\text{move}}. \tag{5.14}$$

We solve for the cluster density and find,

$$n_{\text{c}} = \frac{K n_{\text{m}}^2 n_{\text{g}} L}{2\bar{v}}. \tag{5.15}$$

We see that, with $\bar{v}$ in the denominator, the use of the drift velocity only serves to increase the upper limit of the cluster density. If we increase $\bar{v}$ to account for the faster exit times within the convective-diffusive model, we decrease the evaluated cluster density. We use some typical values for the parameters to evaluate the cluster density. For Cu clusters generated in magentron chamber with an Ar buffer gas at 300 K and 19 Pa [19, 25] we find typical values of: $K = 3 \times 10^{-45}$ m^6/s, $n_{\text{m}} = 2 \times 10^{19}$ m^{-3}, $n_{\text{g}} = 4 \times 10^{21}$ m^{-3}, $L = 0.12$ m, and $\bar{v} = 0.19$ m/s. This gives a maximal cluster density of $\sim 10^{15}$ m^{-3}. Again this is only an upper limit for the cluster density as wall diffusion and cluster coagulation processes will also affect the density, but it is still useful to have.

5.3 Growth via Atom Attachment

The sputtering of metal atoms from the target surface produces a supersaturated gas of free metal atoms that acts as an admixture to the buffer gas. The colder buffer gas helps to cool the free metal atoms below their saturation limit. This causes free atoms to condense onto cluster nuclei leading to metal clusters. The process of condensation is best understood in the context of single free metal atoms adhering to a cluster's surface. This is especially true for the case of small clusters which have smaller collision frequencies with the free metal gas. As the cluster gets larger, with a radius on the order of the mean free path of the metal atoms, it may be the case that several atoms may attach to the cluster's surface at once. We will proceed, however, with the basic picture that the primary mechanism of cluster growth is the attachment of single atoms to the cluster's surface.

5.3.1 Single Atom Attachment Rate

We assume that any collision between a cluster and a metal atom results in the atom's adhesion to the cluster. Furthermore, upon collision, the liquid drop model is invoked and the cluster instantly relaxes to a spherical shape. The attachment process is governed by a specific cluster's collision frequency with the local monomer background. In general this rate is written,

$$k_{\text{attach}} = n_{\text{m}} \varsigma_{N\text{m}} \langle v \rangle_{N\text{m}}. \tag{5.16}$$

The size dependence of the atom attachment rate can been seen when we extract all constant terms into the collision constant $k_0 = \pi r_{\text{w}}^2 \sqrt{\frac{8 k_{\text{B}} T}{\pi m_{\text{m}}}}$,

$$k_{\text{attach}} = k_0 n_{\text{m}} (N^{1/3} + 1)^2 \sqrt{\frac{N+1}{N}}. \tag{5.17}$$

For the case of large clusters ($N \gg 1$) we can write,

$$k_{\text{attach}} \approx k_0 n_{\text{m}} N^{2/3}. \tag{5.18}$$

5.3.2 Mean and Variance of Cluster Radius

We start with the large cluster approximation for the atom attachment rate given by [7, 15, 27, 28],

$$\frac{dN}{dt} = k_0 n_{\text{m}} N^{2/3}, \tag{5.19}$$

where N is the number of atoms in the cluster, n_{m} is the number density of free metal atoms, and k_0 is the growth constant. We will continue under the assumption that n_{m} is effectively constant throughout the growth process. Then invoking the liquid drop model for clusters we set $R = r_{\mathrm{w}} N^{1/3}$ and rewrite the above equation as

$$\frac{d[R^3]}{dt} = k_0 r_{\mathrm{w}} n_{\mathrm{m}} R^2 \Longrightarrow \frac{dR}{dt} = \frac{1}{3} k_0 r_{\mathrm{w}} n_{\mathrm{m}}. \tag{5.20}$$

Applying the boundary condition that the dimer is formed at $t = 0$, we find a rather simple solution for the cluster radius that is linear in time[2],

$$R(t) = \frac{1}{3} k_0 r_{\mathrm{w}} n_{\mathrm{m}} t + R_2, \tag{5.21}$$

where R_2 is the dimer radius.

The distribution properties of the cluster radius are apparently tied intimately with the distribution properties of time itself. That may sound odd because we imagine time to be moving forward steadily. However, we are reminded that within the kMC scheme, time is incremented according to an exponential distribution and therefore has mean and variance values.

It is almost trivial to find the mean cluster radius from Eq. (5.21), simply take the mean or expectation value of each side:

$$\mathrm{E}[R(t)] = \frac{1}{3} k_0 r_{\mathrm{w}} n_{\mathrm{m}} \mathrm{E}[t] + R_2. \tag{5.22}$$

The variance is found easily as well to be:

$$\mathrm{Var}[R(t)] = \left(\frac{1}{3} k_0 r_{\mathrm{w}} n_{\mathrm{m}}\right)^2 \mathrm{Var}[t]. \tag{5.23}$$

To verify this last equation we can use Eq. (5.21) to find the variance by definition. We find two equations; the first is made by taking the mean of each side and squaring, the second is made by squaring the equation first and then taking the mean. The variance is the difference between these two equations.

As pointed out earlier, time is incremented according to exponential distributions associated with the growth process. These exponential distributions are characterized via the cluster growth rates which were given above as our starting point. For convenience, we write these growth rates as $k_j = k_0 n_{\mathrm{m}} j^{2/3}$, where the index j is the number

[2] A linear growth rate was also observed experimentally for carbonaceous nanoparticles [66].

of atoms in the cluster. The mean and variance of the exponential distributions are given by, $1/k_j$ and $1/k_j^2$ respectively. We can go on to build cumulative values as sums over the means and variances of many exponential distributions, but we should be careful to think clearly on the connection between time and the growth rates.

Starting with a cluster of size $N = 2$, we can find the expected time for the cluster to grow to size $N = 3$ from the growth rate k_2, specifically we have,

$$\mathrm{E}[t_{N=3}] = \frac{1}{k_2}. \tag{5.24}$$

Moving on with the growth process, we find the expected value for a cluster of size $N = 4$,

$$\mathrm{E}[t_{N=4}] = \frac{1}{k_2} + \frac{1}{k_3}. \tag{5.25}$$

In general we have, for a cluster created as a dimer at $t = 0$, the expected time to reach size $N > 2$,

$$\mathrm{E}[t_N] = \sum_{j=2}^{N-1} \frac{1}{k_j}. \tag{5.26}$$

The same logic can be carried through with the variance. This allows us to express the cumulative mean and variance, respectively, as

$$\mathrm{E}[t_N] = \sum_{j=2}^{N-1} \frac{1}{k_j} \text{ and } \mathrm{Var}[t_N] = \sum_{j=2}^{N-1} \frac{1}{k_j^2}, \tag{5.27}$$

and the variance of $R(N)$ as:

$$\mathrm{Var}[R(N)] = \left(\frac{1}{3} k_0 r_\mathrm{w} n_\mathrm{m}\right)^2 \mathrm{Var}[t_N] = \left(\frac{1}{3} k_0 r_\mathrm{w} n_\mathrm{m}\right)^2 \sum_{j=2}^{N-1} \frac{1}{k_j^2} = \frac{r_\mathrm{w}^2}{9} \sum_{j=2}^{N-1} \frac{1}{j^{4/3}}. \tag{5.28}$$

For a slight bit of simplification in the notation, we recognize the summation term to be quite similar to the generalized harmonic number [67],

$$H_a^{(b)} = \sum_{m=1}^{a} \frac{1}{m^b}. \tag{5.29}$$

With this notation we have,

$$\mathrm{Var}[R(N)] = \frac{r_\mathrm{w}^2}{9} \left(H_{N-1}^{(4/3)} - 1\right). \tag{5.30}$$

We can also use our starting point ($\frac{dN}{dt} = k_0 n_\mathrm{m} N^{2/3}$) to find $N(t) = (\frac{k_0 n_\mathrm{m} t}{3} + 2^{1/3})^3$. This allows us to write,

$$\mathrm{Var}[R(t)] = \frac{r_\mathrm{w}^2}{9}\left(H^{(4/3)}_{(\frac{k_0 n_\mathrm{m} t}{3}+2^{1/3})^3-1} - 1\right). \tag{5.31}$$

5.3.3 Atom Attachment between Size Indices

As mentioned in the previous section, cluster growth by single atom attachment is viewed to be the fundamental growth mechanism. The mathematical realization of this process is described by the theory of Poisson processes. In this context the time evolution of cluster sizes is governed by exponentially distributed waiting times for clusters to grow by one atom. A KMC implementation is straightforward, we simply sample the time for atom attachment from an exponential distribution with an appropriately chosen rate parameter.

This basic approach, however is suitable only for a size index scheme, as above where $p = 1$, that resolves the full spectrum of cluster sizes. In general, the waiting times for the growth from one size index to the next is not distributed exponentially.

Suppose we are looking to find the waiting time to go from a size index i to $i+1$. We can find this by summing several independent random variates. Let T_j be a random variate of time drawn from the exponential distribution $f(t;\lambda_j)$, and λ_j is the rate parameter associated with the growth of a cluster from size S_j to S_{j+1} atoms. Then our waiting time to go from i to $i+1$ is,

$$T_{i\to i+1} = \sum_{j=\mathcal{N}_i}^{\mathcal{N}_{i+1}-1} T_j. \tag{5.32}$$

This method is statistically correct, but computationally cumbersome. As the index increases, so does the number, $\Delta\mathcal{N}_i$, of clusters represented and more computation time is needed to perform the sum of random variates. A streamlined solution is to draw a single random variate from the convolution of $\Delta\mathcal{N}_i$ exponential distributions. In general this distribution can be written [68],

$$f_{i\to i+1}(t) = \sum_{j=\mathcal{N}_i}^{\mathcal{N}_{i+1}-1}\left(\frac{\Pi_{k=\mathcal{N}_i}^{\mathcal{N}_{i+1}-1}\lambda_k}{\Pi_{k\neq j}^{\mathcal{N}_{i+1}-1}(\lambda_k-\lambda_j)}\right)\mathrm{e}^{-\lambda_j t} \tag{5.33}$$

This distribution function is exact and would simplify the computation immensely, however it is not a standard distribution. Treating this distribution numerically can

be difficult too because of the terms in the denominator. As two clusters get larger while maintaining a size difference of only one atom, the difference between their rates for single atom attachment get closer and closer to zero. Thus, for larger indices, the denominator has terms that approach zero. This problem is sidestepped if all of the λs under consideration are equal.

A convolution of k equal exponential distributions with a rate parameters λ is an Erlang distribution with the probability density function,

$$f(t; k, \lambda) = \frac{\lambda^k t^{k-1}}{(k-1)!} \mathrm{e}^{-\lambda t} \tag{5.34}$$

We take advantage of this fact and make the approximation that the single atom attachment rates for all clusters in a size index are equal and given by the median cluster size.

For index schemes where $p = 1.5$ or 2, the Erlang approximation is nearly indistinguishable from the exact convolution. With $p = 3$, we can see minor deviations for small indices, but the deviations become negligible for larger indices.

Figure 5.1 illustrates the validity of this approximation. For small indices we can show the exact convolution of exponentials versus the Erlang approximation. As we mentioned earlier, numerically treating the exact convolution gets difficult for larger indices, but we can still compare a sampled convolution as a sum of independent random variates. In both cases, we can see that the Erlang approximation is quite good. For the case of $i = 0$, the Erlang approximation is even exact since this index is always reserved for just one cluster size.

The implementation is then as follows: to sample the waiting time between successive indices we use an Erlang distribution approximation with a rate given by the rate of the median cluster size and a shape parameter given by the number of cluster sizes represented by the size-index.

$$T_{i \to i+1} \sim \mathrm{Erl}(\Delta \mathcal{N}_i, \lambda_{\mathcal{M}_i}) \tag{5.35}$$

This approximation will get better as the cluster sizes get larger because the rates will get closer to the same value.

Figure 5.2 shows the effect of the size index scheme on the size distribution. Here we set up a simple simulation where clusters move at a fixed velocity through a constant monomer density. In Figure 5.2 (a), the distribution corresponding to $p = 1$ represents the accepted curve, as this is generated with a full resolution of cluster sizes, and we look

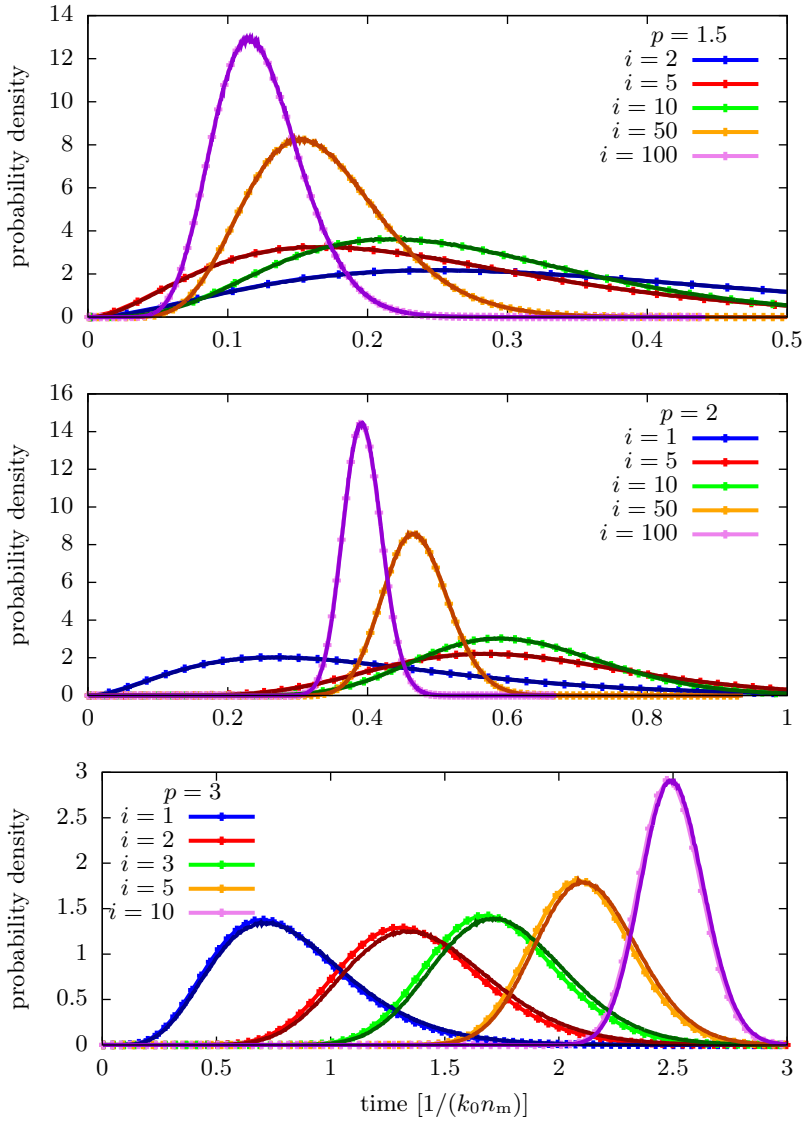

Figure 5.1: Probability distribution functions for the waiting times to grow by an additional index. Samples of the exact convolution of exponential distributions are shown as solid lines and their Erlang approximations are plotted with symbols.

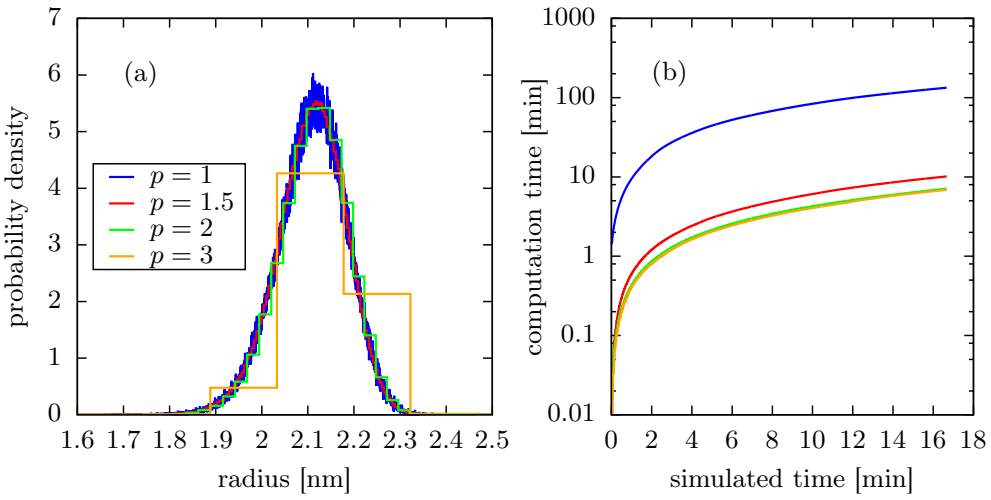

Figure 5.2: (a) Comparison of effect of the choice of size index power. The distribution for $p = 1$ represents a fully resolved distribution. For $p = 3$ the resolution is very poor, but for $p = 2$ we can reasonbly reproduce the $p = 1$ case. (b) The computation times are compared showing considerable decrease in computation time for $p = 1.5$ and higher.

to see if other size index schemes can reproduce it. For $p = 3$ the resulting distribution displays a similar mean value, but the resolution is very poor. For $p = 1.5$ and $p = 2$ we see very good agreement with the accepted distribution. Figure 5.2 (b), shows that even for a $p = 1.5$ we can reduce the computation time needed by an order of magnitude. This improvement is not greatly enhanced much further for $p = 2$ or $p = 3$ indicating that the other processes involved in the simulation (particularly the movement process) dominate in both cases.

5.4 Cluster Coagulation

The nucleation process continually creates more cluster nuclei. The atom attachment process develops these nuclei into larger clusters. These two effects in combination produce increased probability for the collision of two clusters. Within our model, the collision of two clusters leads to cluster coagulation. We assume that two clusters collide resulting in a single cluster with a size equal to the sum of those colliding and that the liquid drop model allows for a fast equilibration to a spherical shape (see Sec. 5.4.4).

The collision process is generally governed by the collision rate between two clusters. A particular cluster of size N will collide with some cluster of size M with a rate,

$$k_{NM} = n_M \kappa_{NM}, \tag{5.36}$$

where n_M is the number density of clusters with size M and κ_{NM} is the coagulation kernel between the two cluster sizes.

5.4.1 Coagulation Kernels

The theoretical dynamics for the coagulation process was founded by Smoluchowski in the early part of the twentieth century. The Smoluchowski coagulation equation (not to be confused with the Smoluchowski diffusion equation from Sec. 4.5) is an integrodifferental equation involving the densities of the medium and diffusing particles and a coagulation kernel. It allows for multipule pathways to achieve a particular cluster size. We do not set out to solve the Smoluchowski equation directly, but our model should obey it within certain limits.

The coagulation kernel is instrumental in establishing the character of the coagulation process. In principal this kernel can take any form however within the literature the two most common kernels used are the free molecular kinetic kernel and the diffusion limited aggregation kernel. The kinetic kernel takes the form [7],

$$\kappa^{\text{kin}}_{NM} = \langle v \rangle_{NM} \varsigma_{NM} = \sqrt{\frac{8 k_{\text{B}} T}{\pi \mu_{NM}}} \pi (r_N + r_M)^2, \tag{5.37}$$

where N and M are cluster sizes, μ_{NM} is the reduced mass, and $r_{N,M}$ are the cluster radii. The term under the radical is simply the mean relative thermal velocity of the two clusters. While $\pi(r_N + r_M)^2$ is the geometric collision cross section. The diffusion kernel takes the form [7, 69],

$$\kappa^{\text{dif}}_{NM} = 4\pi (D_N + D_M)(r_N + r_M), \tag{5.38}$$

where D_N and D_M are the diffusion coefficients for the two clusters.

The choice of which coagulation kernel to apply is understood through a comparison between the mean free path of clusters with respect to the buffer gas, ℓ_{g}, and the mean distance between two clusters, ℓ_{c}. If we find that the ratio $\ell_{\text{g}}/\ell_{\text{c}} \ll 1$, then we can assume that any given cluster will encounter many buffer gas collisions before colliding with another cluster. The clusters are then thought to move diffusively between

each other, and we will therefore employ the diffusive coagulation kernel. Conversely, if $\ell_g/\ell_c \gg 1$, then cluster collisions occur more frequently and we will take the relative movement between them to be of a kinetic nature and use the kinetic coagualtion kernel.

We use a mean free path of clusters with respect to the buffer gas of $\ell_g = (n_g \varsigma_g)^{-1}$, where n_g is the number density of the gas atoms and ς_g is the geometric collision cross-section between a cluster and a gas atom. The mean distance between two clusters is estimated by $n_c^{-1/3}$. Using typical parameters found for Cu clusters with a radius of 3 nm in an Ar buffer gas at 19 Pa in combination with the upper limit of cluster densities found in Section 5.2, we find $\ell_g/\ell_c \approx 0.8$. The ratio will decrease for lower cluster densities as well, and since our esitmated cluster density is known to be large, we will typically take the diffusive coagulation kernel within our model.

5.4.2 Single Cluster Total Collision Rate

There are several ways to treat the collision of a particluar particle with some member of some size species. A brute force method may have us assign a separate collision process to each possible combination of size species that exists in the system. In such a scenario we would have many possible events that could occur, and we would have to appeal to many exponential distributions to generate at sampled time for each possible collision. This, however, seems to be inefficient upon inspection. It would be more practical to define a total collision rate for some member of size-species N to collide with any other cluster in its local environment. There are several ways to do this as well, and here we will look at two of them.

The first method takes its cues from traditional KMC approaches with each possible collision being completely independent from one another. For a particular cluster of size N, each possible collision with some member of size-species M follows an exponential distribution of the waiting time for a collision with a rate defined by $\lambda_{NM} = n_M \kappa_{NM}$,

$$f(t) = \lambda_{NM} \mathrm{e}^{-\lambda_{NM} t}. \tag{5.39}$$

The probability for survival up to a time t, that is the probability that a collision event between N and M has not occurred is,

$$p_{\text{survival},\, M} = 1 - F(t) = 1 - \int_0^t f(t')dt' = \mathrm{e}^{-\lambda_{NM} t}. \tag{5.40}$$

Then we can compose the total survival probability, that a cluster of size N has not collided with any of its neighbors by,

$$p_{\text{survival,total}} = \prod_M p_{\text{survival},\,M} = \exp\left[-t\sum_M \lambda_{NM}\right], \tag{5.41}$$

where both the products and sum run over all size-species M that are local to the particular cluster N. This leads us to the idea that the total survival probability is linked to a single exponential distribution with a total rate given by,

$$\lambda_{\text{total},\,N} = \sum_M \lambda_{NM} = \sum_M \frac{T_M}{V}\kappa_{NM}. \tag{5.42}$$

Again, this paradigm assumes the independence of each possible collision and leads to a total rate for a collision event that is simply the sum of all the individual collision rates.

Another treatment of the total dependent rate is derived with respect to a mean rate via the size distribution function. Let $g(N)$ be the size distribution function of clusters local to our paricular cluster under consideration with the normalization condition $1 = \int_0^\infty g(N)dN$. The mean rate for a particular cluster of size N to collide with some cluster of size M can be expressed as,

$$\langle\lambda_N\rangle = \int_0^\infty \lambda_{NM} g(M)dM. \tag{5.43}$$

We can then multiply $\langle\lambda_N\rangle$ by the total number of clusters, T_{total}, local to our cluster to find a total rate,

$$\lambda_{\text{total},\,N} = T_{\text{total}}\langle\lambda_N\rangle. \tag{5.44}$$

This general approach to finding a total collision rate needs to be adjusted for the discrete scenario presented by the cluster size index. In this case we are looking for the total collision rate between a particular cluster of size index i with some cluster of an arbitrary index j. The continuous size distribution function $g(N)$ becomes discrete, $\tilde{g}(i)$ with the normalization condition $1 = \sum_i \tilde{g}(i)\Delta\mathcal{N}_i$, with the summation running over all size indices local to our particular cluster. We can define $\tilde{g}(i)$ more precisely as,

$$\tilde{g}(i) = \frac{T_i}{\Delta\mathcal{N}_i T_{\text{total}}}, \tag{5.45}$$

where T_i is the total number of clusters of size index i, $\Delta\mathcal{N}_i$ is the width of the size index as described in Sec. 5.1.1, and T_{total} is the total number of clusters. The mean

collision rate can then be found as,

$$\langle \lambda_i \rangle = \sum_j \lambda_{ij} \tilde{g}(j) \Delta \mathcal{N}_j = \sum_j \lambda_{ij} \frac{T_j}{T_{\text{total}}}. \tag{5.46}$$

In the continuous case, we mulitiplied the mean collision rate by the total number of clusters to find a total collision rate. Here, $\langle \lambda_i \rangle$ is a mean collision rate with respect to the number of size indices local to our cluster. Therefore our total collision rate is,

$$\lambda_{\text{total},\, i} = T_{\text{indices}} \langle \lambda_i \rangle, \tag{5.47}$$

where T_{indices} is the number of different size species.

Note the difference between the independent total rate and the dependent total rate.

5.4.3 Choosing a Particular Cluster to Collide with Another

In the previous section we defined a rate for a particular cluster to collide with some other cluster in its local environment. This is to say, we have a means for defining when some collision event is performed. But we still need to find a particular cluster that exists locally to the cluster to which we have assigned the collision event. In defining a means for choosing a single cluster that it does collide with, we need to find a realization of a collision event that can be performed in the simulation.

We approach this via a sample from the total collision rate defined above. We draw a random variate, U, from a uniform distribution defined on the interval (0,1). Then, we use this to effectively sampe from the total rate, $\tilde{\lambda}_{\text{total}} = U \lambda_{\text{total}}$. Finally we compose a partial sum of the individual particle species collision rate. The particle species for which the partial sum is greater than or equal to the sampled rate is chosen to be the species with which our chosen cluster collides. With a total rate defined as the sum of independent rates, we would have

$$\tilde{\lambda}_{\text{total}} \approx \frac{1}{V} \sum_{M}^{M^*} T_M \kappa_{NM}, \tag{5.48}$$

where the summation runs over all species local to our particular cluster and M^* is the species chosen to compose the collision. Finally we simply choose a random cluster of species M^* and carry move along further with the collision event.

5.4.4 Cluster Sticking Efficiency

As mentioned earlier, upon collision the liquid drop model is invoked and a larger spherical cluster is the result. However, it stands to reason that there should be a limitation in the sticking efficiency of two clusters. Indeed taken in an extreme limit two macroscopic metal balls would not coagulate upon collision, they would simply bounce off of each other. A similar mechanism was also put into place for simulations of the formation of nanocolumns via metal deposition [41]. Quantifying this transition is not trivial, however, and an exact solution has yet to be achieved.

We can however, make a first guess for the value of a critical radius that would ensure that clusters coalesce upon collision. It is well established that there exists a melting point depression for metals [70–73]. That is, small nano-sized clusters are known to melt at lower temperatures compared to the bulk material. This is due to the large surface to volume ratio. Surfaces have a lower cohesive energy than the bulk because there are fewer neighbors available to aid in binding an atom to the surface. As the surface to volume ratio increases (inversely to the cluster size), there is less energy required to free atoms from their groundstate positions and melting may be achieved for lower temperatures. Using this theory we can establish a cluster size that would be in a liquid state for our system's temperature. We then assume that if a liquid cluster is involved in a collision process, then there is a higher degree of probability that it will adhere to another cluster. The liquid nature of the cluster would allow for a larger area of contact between two colliding clusters as it can warp upon collision. This would also make the use of the liquid drop model more plausible when applying it to the coagulation of two clusters. Nanda introduced a rather simple model for the size dependent melting point of nanoparticles [71] of the form,

$$T_{\text{melt}}(N) = T_{\text{bulk}} \left(1 - \frac{\beta}{2R(N)} \right), \tag{5.49}$$

where T_{melt} is the melting temperature of the particle, T_{bulk} is the melting point of the bulk material, β is a material dependent constant, and R is the particle radius. Table 5.2 shows the parameters for the Nanda model of melting point depression for some typical metals used in the generation of clusters in magnetron sources. Figure 5.3 shows the melting point depression curve for Cu clusters. We can see that nano-sized clusters can have melting points that are significantly lower than the bulk melting point. For a cluster source of Cu operating at a temperate of 300 K, we can expect that clusters with

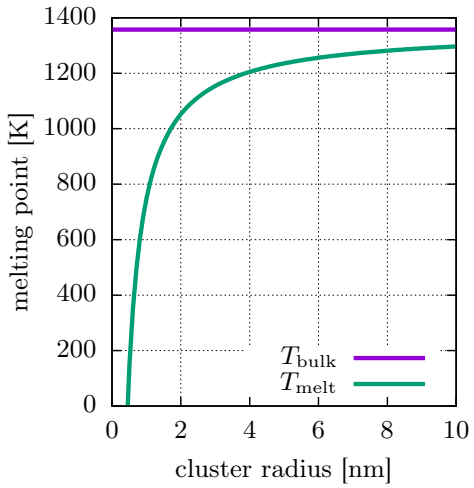

Figure 5.3: Melting point depression curve for Cu clusters based on the model in Ref. [71]. Small clusters melt at a significantly lower temperatures compared to the bulk melting point.

Metal	T_{bulk} [K]	β [nm]
Fe	1809	0.94232
Cu	1357.6	0.9
Ag	1234	0.96564
Au	1337.6	1.1281

Table 5.2: Melting point depression parameters for various common metals used in cluster sources [71].

radii smaller than about 0.6 nm will be in a liquid state and will easily coalesce upon collision.

The use of the melting point depression as a means for obtaining a critical cluster radius for the coalescence of two clusters is only a first estimation. For instance the average collision is met with an energy of $k_{\text{B}}T$ which may be sufficient to melt the collision interface of two clusters and allow for a stronger chance that the two clusters will merge as a single particle. We proceed by allowing the critical cluster radius to be a free parameter. Furthermore we introduce a sampling procedure for the sticking probability for each collision event.

We have already introduced the free parameter for the critical cluster radius, r_c, with motivation held within the melting point depression model. We introduce another free parameter for the variance of the critical radius, σ_c^2. Then we compose a distribution of the critical cluster radius with respect to each collision event, $f_{\text{critical}}(R)$. The exact form of the distribution is not analyzed in detail, but we would like to maintain at least two criteria: 1) the distribution should forbid the sampling of negative cluster radii, and 2) we would like to maintain a high degree of probability for a sampled critical radius

to return that given by our input parameter r_c. With these criteria in mind we choose a log-normal distribution to serve as a distribution of the critical cluster radius with a mean of r_c and variance σ_c^2,

$$f_{\text{critical}}(R;\mu,\sigma) = \frac{1}{R\sigma\sqrt{2\pi}}\exp\left[-\frac{(\ln(R)-\mu)^2}{2\sigma^2}\right], \tag{5.50}$$

where $\mu = \ln\left(\frac{r_c}{\sqrt{1+\sigma_c^2/r_c^2}}\right)$ and $\sigma = \sqrt{\ln\left(1+\sigma_c^2/r_c^2\right)}$.

The procedure for sampling the sticking efficiency is simple. For each collision event encountered we sampled a value from $f_{\text{critical}}(R)$ to serve as the critical cluster radius for that collision event. Then, if either of the two clusters' radii are equal to or smaller than the sampled critical radius, we allow the collision event to result in the coalescence of the two clusters. If the sampled critical radius is less than either of the two clusters' radii, we abort the coagulation procedures and the two particles remain in the system as they were. This results in an effective sticking probability given by the curve,

$$P_{\text{sticking}}(R) = 1 - \int_0^R f_{\text{critical}}(R')dR' = 1 - \frac{1}{2}\text{erfc}\left[-\frac{\ln(R)-\mu}{\sigma\sqrt{2}}\right] \tag{5.51}$$

Figure 5.4 shows the sticking probability curves for various combinations of the two free parameters r_c and σ_c^2. Given the parameters shown, a cluster with a radius of 5 nm will have a near 0% chance of sticking to another cluster upon collision. But collision events, of course, involve two clusters, so if the 5 nm cluster collides with a very small cluster whose individual sticking probability is high, then the collision will very likely result in the coalescence of the two. The left figure (a) shows the influence of the mean critical radius r_c which serves as the center point for the curve. The right figure (b) shows the influence of the σ_c^2 which affects the probability's decay. For low values of σ_c^2, we approach a step-like function such that r_c acts as hard limitation for the coagulation of two clusters. Whereas larger values of σ_c^2 allow for a greater probability of that larger clusters may coalesce. Figure 5.5 displays the effect of various sticking probabilities on the resulting size distribution of clusters. In these examples we have Cu clusters generated in a cluster source with an Ar buffer gas at 19 Pa with a flow rate of 15 sccm and an operating temperature of 300 K. The chamber length is 12 cm and we have placed 150 spatial slices into the system. Nucleation takes place in only the first slice, thereafter, the clusters are moved through the system with only a steady drift velocity of about 19 cm/s. We do not allow atom attachment or wall diffusion to take place. These parameters were chosen to be somewhat typical of the conditions in experimental set-ups, but we try to highlight only the coagulation process.

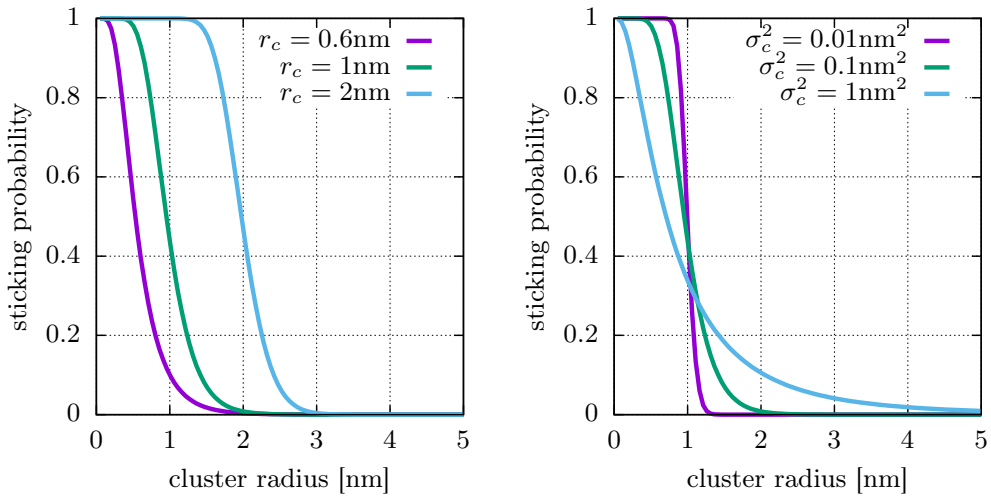

(a) $\sigma_c^2 = 0.1$ nm^2 (b) $r_c = 1.0$ nm

Figure 5.4: Sticking probability curves. Increasing the mean of the critical radius distribution (a) increases the probability for larger clusters to successfully stick to another. Increasing the variance of the critical radius distribution (b) decreases the slope of the sticking probability, thereby slightly increasing the chance for larger clusters to successfully stick to another, but simultaneously decreasing the chance for smaller clusters.

Figure 5.5 (a) shows the effect of the mean critical radius, r_c. Here, we keep σ_c^2 fixed at 0.1 nm^2 and vary the free parameter r_c. We know that increasing r_c will allow for a greater probability for larger clusters to coalesce, thus forming larger clusters. This is reflected in the presented size distributions. With a low value of r_c we observe a low mean value for the cluster size. Increasing r_c shifts the mean value towards larger clusters. Note that the distributions corresponding to $r_c = 1.5$ and $r_c = 2.0$ are essentially the same. The equivalence of these two curves is understood by the limitation of the chamber length, and hence the residence time for the clusters in the chamber. Clusters are emitted from the chamber before they have the opportunity to grow much larger than $R = 1.5$ nm. Therefore, the additional growth that $r_c = 2.0$ would otherwise allow is not capitalized upon and we can consider a natural limitation to cluster growth.

Figure 5.5 (b) shows the effect of the variance of the critical radius. Again, we are holding r_c constant at 1.0 nm and observing the influence of σ_c^2. These distributions generally maintain a similar mean value to the resulting cluster size distribution, but

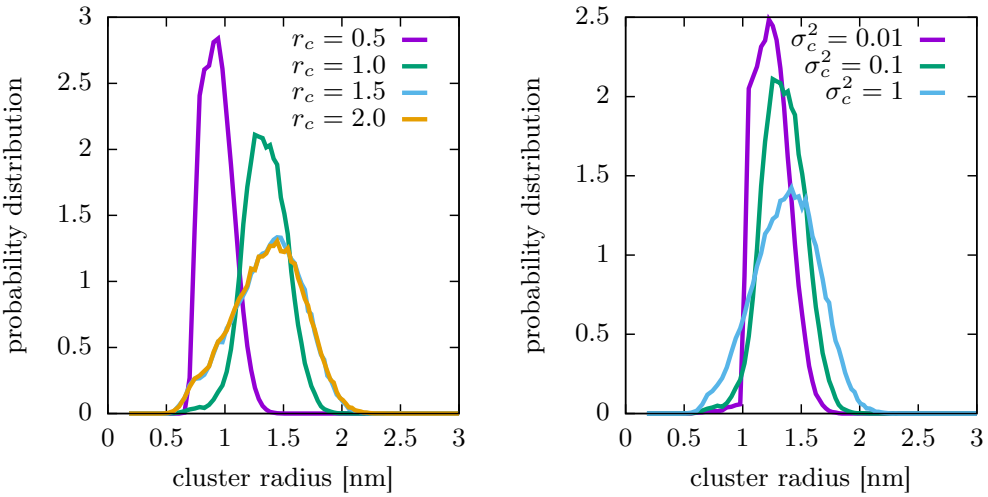

(a) $\sigma_c^2 = 0.1$ nm^2 (b) $r_c = 1.0$ nm

Figure 5.5: Cluster size distributions resulting from various sticking probabilities.

change in the distribution's width. The tightest distribution is seen for low values of σ_c^2 and the distribution broadens as we increase σ_c^2. Note too the correspondence between the step-like behavior of the sticking probability for $\sigma_c^2 = 0.01$ (as shown in Figure 5.4 b) and the jump in the size distribution for the same value of σ_c^2 near the critical radius. Increasing σ_c^2 to 0.1 nm softens this discontinuity to result in an overal smoother distribution. Continuing to increase σ_c^2 allows for a greater probability of larger clusters coalescing, but again we seem to encounter a similar distribution presented in 5.5 (a) for larger critical radii. Apparently, the natural limitation presented by the cluster residence time is met and we do not observe clusters much larger that 1.5 nm.

5.4.5 Establishing the New Cluster Size

If a coagulation event is not limited by the critical cluster size then a larger cluster is the result of the coagulation process. For the case of a size index scheme with $p = 1$ the resulting cluster size is simply the sum of the two colliding clusters' size. For example, a cluster of size $N_1 = 200$ colliding with a cluster of size $N_2 = 300$ results in a cluster of size $N_3 = 500$. However, for size index schemes where p is greater than 1 we need to more clearly define the addition of cluster sizes.

The simplest approach would be to always use the size indices' mean cluster size when calculating the addition of two clusters. But this could result in the loss of some information. For example, for the size index scheme with $p = 2$, the size index $i = 2$ encompasses clusters of size $N = 6 - 10$ with $\mathcal{M}_2 = 8$ and the $i = 0$ index contains only the dimer, $N = 2$. Using only the mean value approach, if a cluster of size index $i = 2$ collides with $i = 0$ the resulting cluster would be of size $N = 10$ and would maintain the size index $i = 2$. This effectively would result in the removal of a single dimer. We lose the possibility that a cluster of size $N = 10$, still within the index $i = 2$, collides with the dimer to result in $N = 12$ and moves to the index $i = 3$.

We deal with this discrepancy by assuming that clusters are distributed uniformly in each size index over the interval of the index's cluster sizes. Within the cluster collision event, we then sample a size for each cluster and the resulting cluster is assigned the size index appropriate to the sum of the cluster sizes. With respect to the example above, we then allow for the possibility that $i = 2$ colliding with $i = 0$ may form a new cluster of $i = 2$ or $i = 3$.

Essentially, all models are wrong, but some are useful.

GEORGE E.P. BOX

CHAPTER 6

Results

In this chapter we present the results for our model. Throughout these results, we will focus on the key quantity of the cluster size distribution. We will look at the effects that various input parameters may have on the cluster sizes to gain insight into the most important processes and conditions that stimulate or control cluster growth and sizes.

The standard model, upon which we base our results, is chosen to be of a system similar to that in Refs. [19, 74]. We will look at Cu cluster growth in an Ar buffer gas in a magnetron chamber of length 12 cm. Standard background conditions are chosen to be a temperature of $T = 300$ K, buffer gas pressure of $P = 19$ Pa, and an Ar flow rate of $F = 15$ sccm. We set the ion current density to 0.8 mA/cm^2 [18]. The sputtering yield, the number of target atoms sputtered for each incident ion, is set to 1.05 [75]. We take the region of target erosion due to the sputtering process to be a concentric ring between 1.25 and 1.75 cm [76]. Using Eqn. (4.62), this gives an initial free atom number density of $\bar{n}(0) \approx 1.69 \times 10^{13}$ cm^{-3}, which is consistent with the estimate given in Ref. [15]. Variations to these parameters will be noted as we proceed through the chapter.

6.1 Buffer Gas Properties

Properties of the surrounding buffer gas, into which the metal atoms are sputtered, play a large role in establishing the overall dynamics of the system. Indeed the conditions of the background gas permeate into all other processes and rates. We look at three essen-

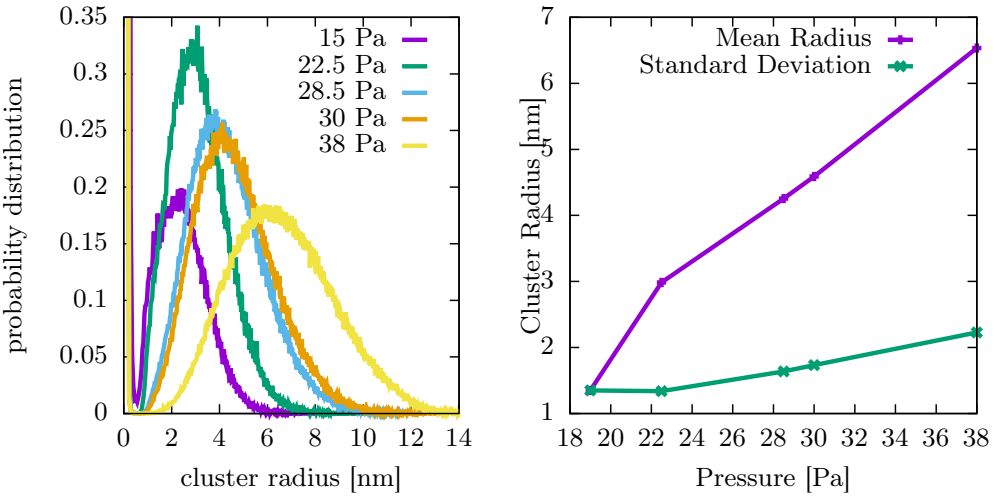

(a) Size Distribution

(b) Mean and Standard Deviation

Figure 6.1: Effect of buffer gas pressure: (a) cluster size distributions with the variation of gas pressure, (b) mean and standard deviation of the distributions in (a). Increasing gas pressure results in larger clusters.

tial gas parameters: buffer gas pressure (P), buffer gas flow rate (F), and temperature (T).

6.1.1 Buffer Gas Pressure

The gas pressure is proportional to the number density of buffer gas atoms via the ideal gas law, $n_g = \frac{P}{k_B T}$. In turn, n_g enters directly into the nucleation rate for new clusters (Eqn. (5.12)). More importantly however, n_g is directly proportional to the collision frequencies of metal particles and buffer gas atoms (Eqn. (5.5)), and hence, inversely proportional to the diffusion constant for metal particles (Eqn. (4.40)). The diffusion constant affects the metal particle mobility and enters into the rates of several processes. In terms of metal particle transport, the diffusion constant affects:

- the decay rate of the metal atom density profile (Eqn. (4.55)),
- the FPTD and MFPT in the radial diffusion of metal clusters to the chamber walls (Eqn. (4.83)),

- the mean movement time and transition probabilities for metal particles between spatial slices (Eqn. (4.90)).

Additionally, the diffusion constant is also significant in establishing the cluster coagulation rates via the coagulation kernel (Eqn. (5.38)).

Some of these pressure dependencies drop out however, when we consider the buffer gas pressure's effect on the drift velocity ($\bar{v}$). The gas pressure is also, as with the diffusion constant, inversely proportional to the buffer gas drift velocity (Eqn. (4.4)) which is then transmitted to the metal particles. Consequently, any rates that contain a $\frac{\bar{v}}{D}$ term will remain independent of the buffer gas pressure. This means the decay rate of the metal atom density profile and the axial movement transition probabilities are unaffected by a change in gas pressure. The drift velocity appears without the diffusion coefficient in the mean movement time and in the initial metal atom density (Eqn. (4.61)). Larger pressures result in a lower drift velocity and therefore we expect larger free metal atom densities. The larger metal atom densities will then increase the rate of atom attachment to existing clusters and will independently increase the nucleation rate separately from an increase in gas atom density.

Pulling all these effects together we have the following picture for the effect of the pressure within the system. An increase of pressure drives-up the number density of buffer gas atoms. As a result, the diffusion constants for metal particles and the drift velocity decreases. Metal particles essentially linger in the system longer by having slower axial movement times and longer waiting times to diffuse to the chamber walls. We can also expect more clusters to be generated because of an increase in the nucleation rate, compounded through the effects of an increase in the initial metal atom density and an increase in the buffer gas atom density. The increase of metal atom density will also increase the rate of atom attachment to existing clusters. Lastly, the cluster coagulation kernel is decreased because of the decrease in diffusion coefficients, but the overall coagulation rate may increase due to the increase in the number of clusters.

Figure 6.1 (a) shows a comparison of the emitted cluster size distribution with variations to the buffer gas pressure. As with all cluster size distributions presented in this chapter, we have truncated the range of the probability distribution to highlight the development of local peaks of the cluster sizes. The probability density of very small clusters (< 10 atoms) dominates the distribution. However, when invoking a comparison to experimental results, the domain of measurable clusters sizes are often limited below 100 atoms [6, 23] and we therefore ignore the initial peak observed within our results. We can see that the most probable cluster size (again, disregarding the smallest

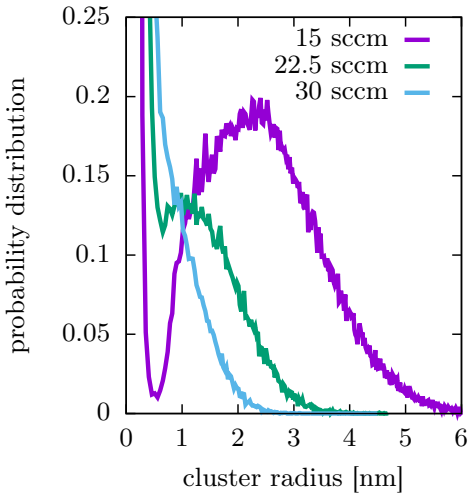

Figure 6.2: Effect of buffer gas flow rate on cluster size distribution. An increase in the flow rate increases the drift velocity and causing a decrease in the free atom density resulting in smaller clusters.

clusters) shifts to larger values with the increase of pressure. The increase in cluster size with the increase of gas pressure is perhaps more clearly depicted in Fig. 6.1 (b). Here, we plot the mean cluster radius and standard deviation of each of the distributions in (a) with respect to the pressure. We note that the relationship of both the mean cluster radius and the standard deviation to the buffer gas pressure is nearly linear. This result is qualitatively consistent with experimental findings presented by Wang et al. in Ref. [77].

6.1.2 Buffer Gas Flow Rate

Isolating a variation in the buffer gas flow rate only directly impacts the drift velocity (Eqn. (4.4)) of the buffer gas. As we mentioned above, the drift velocity is then linked to the transport properties of the clusters. We expect that an increase in the buffer gas flow rate will result in larger drift velocities and shorter residence times for clusters in the system. We also expect a decrease to the initial free atom density causing a decrease in the nucleation rate and atom attachment rates to existing clusters.

Figure 6.2 (a) shows the effect of the buffer gas flow rate on the emitted cluster sizes. Evidently the increase of the buffer gas flow rate has a dramatic effect on the cluster size

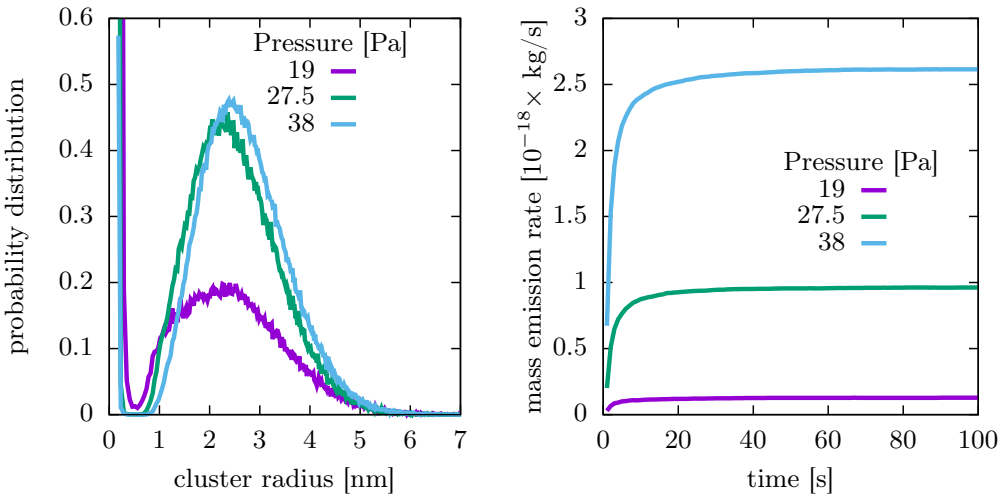

(a) Size Distribution

(b) Mass Emission Rate

Figure 6.3: Effect of increasing pressure while maintaining drift velocity. (a) The peak cluster size is not greatly effected since the cluster residence time remains the same. (b) The increase of pressure allows for higher nucleation rates and hence larger emission rates of clusters.

distribution. Increasing the flow rate by 50% dramatically shifts the peak cluster radius down from about 3 nm to 1 nm. Further increasing the flow rate by 100% removes any peak at all.

6.1.3 Pressure-Flow Rate Ratio

In the previous two examples, we isolated both the buffer gas pressure and the flow rate to see what the effects would be on the cluster size distribution. In practice, the isolation of either parameter is difficult to achieve. In experiment, the increase of pressure is tied intimately to the increase of the flow rate since the emission of gas from the system is limited by the orifice of the chamber. It may therefore be more useful to look at a constant ratio of the pressure and flow rate to see how that affects the cluster size distribution. In leaving the pressure-flow rate ratio constant, we are fixing the drift velocity. However, we will still see a decrease in the diffusion constants and will expect process rates to change accordingly.

Figure 6.3 shows the effects of varying the chamber pressure while maintaining a

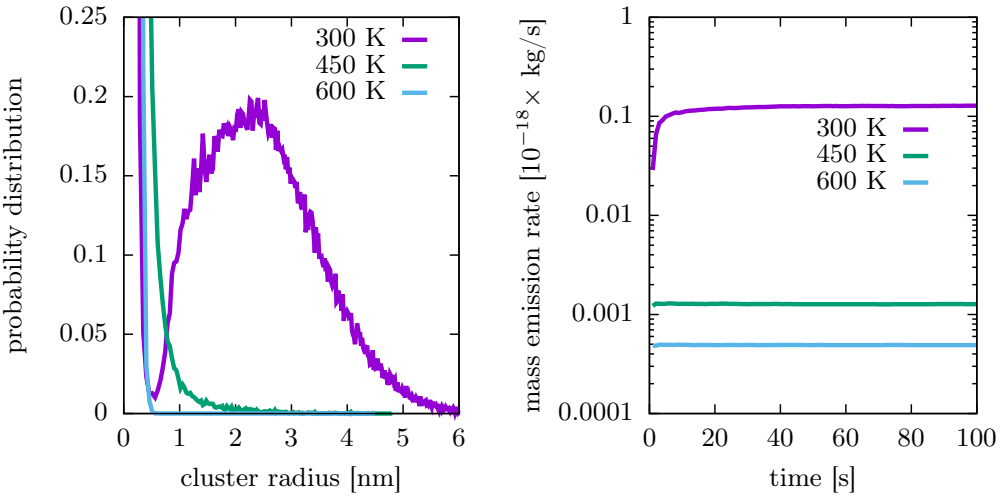

(a) Size Distribution

(b) Mass Emission Rate

Figure 6.4: Effect of an increase of the system temperature. The combined effects of reducing nucleation, atom attachment, and coagulation rates strongly reduces the cluster growth as seen in the size distribution (a) and virtually wipes out the production of clusters altogether (b).

constant drift velocity. While the isolated increase of pressure (Fig. 6.1) had a noticeable effect on the cluster size distribution, leading to larger clusters, the coupled effect of increasing the pressure and flow rate to fix the drift velocity does not greatly affect the size distribution. All sample distributions (Fig. 6.3 (a)) peak at roughly the same position. The curve for a pressure of 19 Pa shows a stronger prevalence of smaller clusters. This is understood through the larger diffusion coefficients in systems with lower pressures. The larger diffusion coefficients allow for clusters to exit the system more rapidly, thus resulting in an increase in the fraction of smaller clusters. Figure 6.3 (b) shows the difference in the mass emission rate for varying the chamber pressure. Although, the cluster size is relatively controlled by the constancy of the drift velocity, the larger pressures still result in a greater nucleation rate, and thus in more material being emitted from the chamber.

6.1.4 Buffer Gas Temperature

We assume local thermal equilibrium over the entire system so that the buffer gas temperature is transmitted to the clusters as well. The system temperature then has a widespread effect over many processes. The temperature is proportional to the drift velocity and inversely proportional to the gas atom number density. The square root of the temperature is proportional to relative particle velocities and inversely proportional to the gas-metal collision frequency. From these we can find that an increase in temperature will decrease movement times, nucleation rates, atom attachment rates, and coagulation rates. In particular, we note that the nucleation rate is ultimately proportional to $\frac{1}{T^3}$, so doubling the system temperature will drive the production of new clusters down by a factor of 8. With far fewer clusters in the system and lower atom attachment rates, we can expect that an increase of the system temperature will result in much smaller clusters. Figure 6.4 illustrates the dramatic effect of increasing the system temperature. We can easily see in the cluster size distribution (a), that the growth of clusters virtually vanishes with an increase of temperature. We can also see in Fig. 6.4 (b) that the production of clusters, is strongly reduced as well.

6.1.5 Pressure-Temperature Ratio

We showed above that the independent variation of buffer gas pressure, temperature, and flow rate can have large effects on the cluster size distribution and overall cluster production. But we also showed that varying the pressure and flow-rate together in order to maintain a constant drift velocity has a relatively low impact on the size distribution. In the same vein we can look at a constant ratio between the temperature and pressure that maintains a constant gas atom number density and drift velocity. Under such circumstances, we find that movement times remain mostly unchanged and nucleation rates remain strictly constant. When we increase the absolute temperature (and pressure) by a factor α, we find an increase in the atom attachment and coagulation rates by a factor of $\sqrt{\alpha}$. Thus, when increasing the pressure while maintaining a constant temperature-pressure ratio, we may expect to find slightly larger clusters generated in the system.

Figure 6.5 displays the results of keeping a fixed ratio of pressure and temperature. At first glance these distributions do not significantly differ from each other. This indicates that the gas atom number density and the drift velocity play a large role in determining the overall size distribution, since, when they are left unaltered, the size

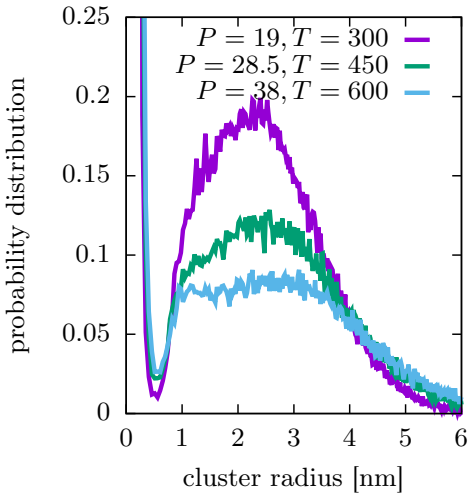

Figure 6.5: Cluster size distributions for an increase of both pressure and temperature. A constant T/P ratio leaves the gas atom density and drift velocity constant.

distribution falls within a similar domain. There are, however, some structural differences between the curves that point to the effect of different processes at work. Particularly, we note the movement away from a single dominating peak with a relatively low pressure/temperature towards a bimodal distribution with larger pressures/temperatures. The emergence of the first peak is due to the coagulation of smaller particles. The atom attachment process then adds to these relatively small clusters to shape the broader peak. With lower temperatures, the atom attachment process does not proceed as quickly and the atom attachment process cannot push the broad peak away from the initial peak developed by coagulation. As the temperature increases, so does the atom attachment rate, and that process is able to act more efficiently to set up a broad secondary peak. This picture of the competition between the atom attachment process and the coagulation process is supported below in Sec. 6.4.

6.2 Other Parameters

We now move to looking at results that are generated by parameters that are not directly related to the buffer gas background. In particular, we look at the effect of the nucleation constant (K), the ion current density (i), the chamber length (L), and the

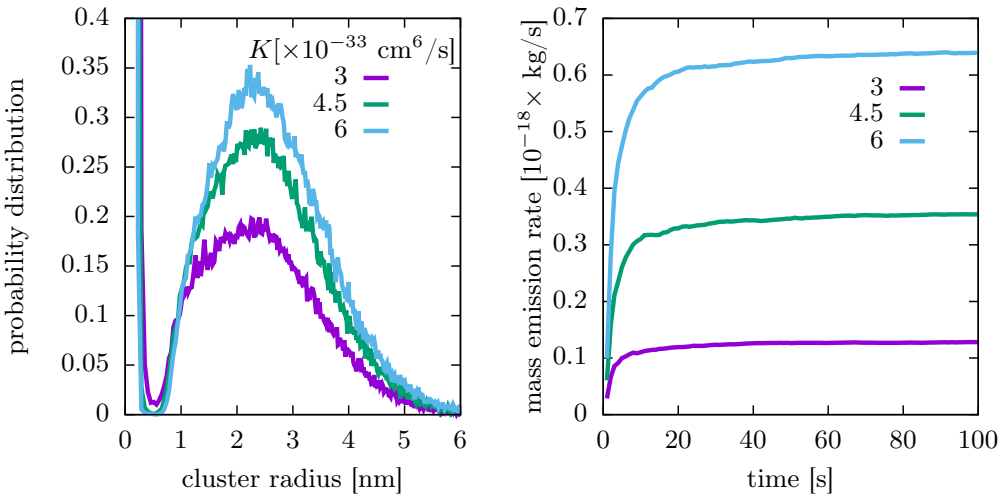

(a) Size Distribution

(b) Mass Emission Rate

Figure 6.6: Effect of the nucleation constant on the cluster size distribution. Increasing the nucleation rate has only a mild effect on the overall size distribution (a). However, we observe more material being emitted from the system with larger nucleation rates (b).

critical cluster radius for coagulation. Of course, both the nucleation constant and the ion current density are physically linked to the buffer background gas. However, within our model, these are taken to be independent parameters that are set independently of the gas pressure, flow rate, and temperature. In varying these parameters then, we do not affect the transport properties of the metal particles. Instead, these parameters only have an influence of the growth mechanisms.

6.2.1 Nucleation Constant

The effect of varying the nucleation constant is quite clear; it directly affects the nucleation rate of new clusters in the system. With more clusters introduced into the system, we can also expect the coagulation rate to increase as well. Figure 6.6 shows the effect of variations in the nucleation constant. What is most notable from this result is that all the distributions are very similar. Evidently, an increase in the cluster density (via an increased nucleation rate) does not significantly alter the coagulation rate such that larger cluster result. We do see however, that with an increase in the nucleation rate,

there is a sharper depletion of smaller clusters. This suggests that the coagulation process has its greatest effect in the domain of small clusters, as we would expect also from considering the critical cluster radius (Sec. 5.4.4). Small clusters have larger diffusion coefficients and hence, the coagulation process can affect smaller clusters more. As the small clusters are depleted through coagulation processes, combined with their growth and larger diffusion coefficients, the coagulation rate drops, and we can assume that cluster growth proceeds by atom attachment.

This result can also help us better understand the results of the pressure variation (Fig 6.1). The nucleation constant affects the cluster number density without affecting the atom attachment rate. The results in this section show only a mild effect of the nucleation rate on the cluster size distribution, so we may conclude that the coagulation processes does not play a large roll in the determination of the cluster size. Therefore, in looking back at the results for the pressure variation, we may conclude that the increase in cluster sizes due to the increase of pressure is primarily a result of an increase in the atom attachment rate.

6.2.2 Ion Current Density

The ion current density is linked to the physical process of sputtering. With an increase of the number of ions striking the target, material is freed from the surface at a faster rate which leads to a higher concentration of the free metal atoms in the system. By applying a variation to the ion current density in our model, we will affect the free metal density which in turn will influence the atom attachment rate and nucleation rate. Figure 6.7 illustrates the influence of the ion current density on the resulting cluster size distribution and mass emission rates. We can easily see that raising the ion current density helps to develop a strong primary peak in the cluster size distribution Fig. 6.7 (a). In addition, the increase in the free metal atom density raises the nucleation rate and we see that more material is emitted from the system for larger ion current densities Fig. 6.7 (b).

6.2.3 Chamber Length

Within our model, the length of the chamber plays no role in determining any process rates. The sole effect of varying the chamber length is to control the residency time of the clusters within the system. Longer residency times allows for more time for the

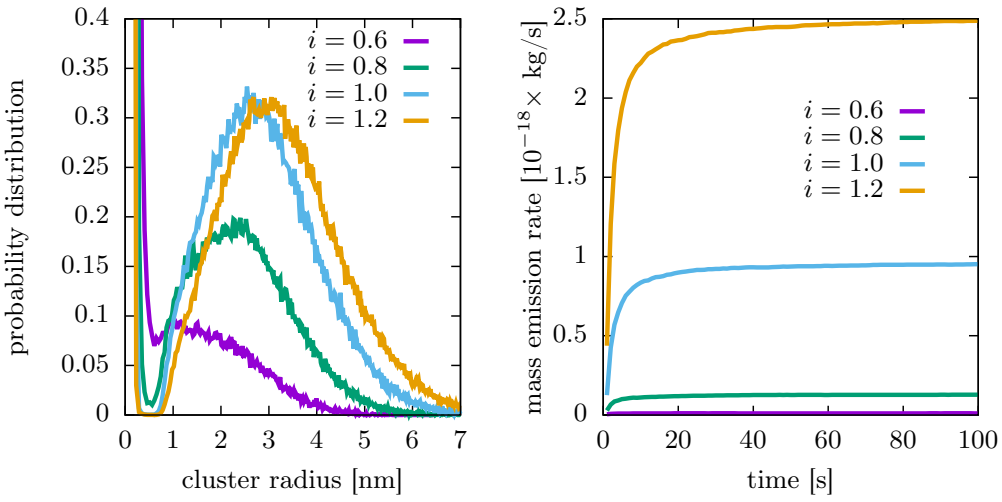

(a) Size Distribution (b) Mass Emission Rate

Figure 6.7: Effect of ion current density (i) on cluster size distribution and mass emission rates. Increasing i results in larger free metal atom densities which helps develop a prominent peak (a) in the cluster size distribution. We also see more material being emitted (b) with larger ion current densities.

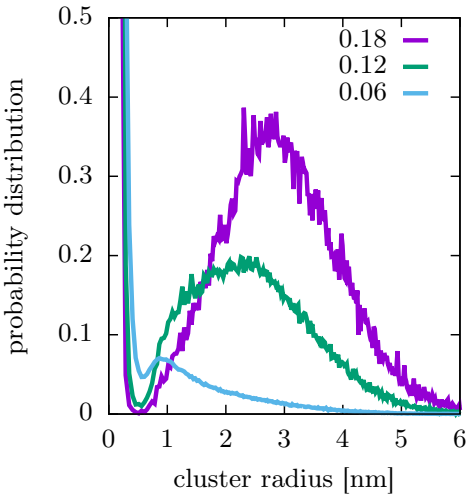

Figure 6.8: The effect of the chamber length [m] on the cluster size distribution. A longer chamber allows for a greater residency time, giving more time for clusters to grow and producing larger clusters.

clusters to grow and hence we would expect to see larger cluster with an increased length of the chamber.

This idea is simply illustrated in Fig. 6.8. We can quickly see that smaller chamber lengths reduce the cluster sizes while larger lengths provide for larger clusters. The shorter residency times of the clusters leads to a higher chance that smaller clusters will exit the system before they have a chance to either diffuse to the chamber walls or collide with another cluster. We can therefore see a stronger prevalence of smaller clusters (< 1 nm) in the shorter system. As the system gets larger, the contribution of smaller clusters decreases in the size distribution.

We can also discern something about the competition between the atom attachment and coagulation processes for cluster growth. With a small chamber length, the clusters do not have much time to grow via the atom attachment process. As a result, the primary peak for a chamber length of 6 cm is given by the coagulation of small clusters. As we increase the chamber length, we allow for more time for the atom attachment process to develop the existing clusters into larger clusters. For the chamber length of 12 cm, we can still see a hint of the residual effect of the initial coagulation process on the size distribution, evidenced by a slight hump before the absolute peak. In our longest example of an 18 cm chamber, we can see that the hump is removed leaving a smoother line shape. This indicates that the atom attachment process is the dominating effect on the size distribution.

6.3 Critical Radius and Experimental Comparison

In Sec. 5.4.4 we found an argument for the critical cluster radius of coagulation where two clusters would be forbidden to complete a coagulation event unless one of them was sufficiently small such that it was in a liquid state according to the melting-point depression model. The use of this criterion also gave credence to our use of the liquid-drop model of cluster morphology. Here we soften these criteria.

It can be the case [70] that a cluster's surface melts at lower temperatures than needed to achieve a completely liquid drop. In such cases it may be possible for two clusters to achieve partial coalescence as their melted surfaces come into contact. It may also be possible that two completely solid clusters are held together if enough of their surface areas come into contact and the interatomic forces are sufficiently strong, i.e. sintering [78, 79].

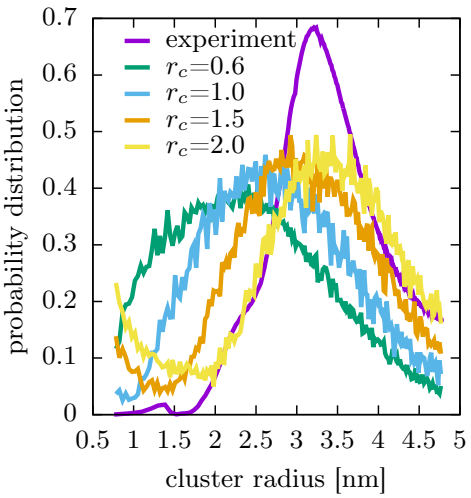

Figure 6.9: Variations to the critical cluster radius can provide for a reasonable quantitative fit to experimental data [74]. The size distributions shown have been truncated and normalized to fit the measurable domain of the experiment. Increasing the critical radius shifts the local minimum and pronounces the dominant peak of the size distribution. For a critical radius of 2 nm, the resulting size distribution is in good agreement with experimental results

In order to address these possibilities we look at the effect of varying the critical cluster radius to allow larger particles a better chance to successfully undergo coagulation with another cluster. Figure 6.9 shows the results of the size distributions with a varying critical radius. We also include here a comparison to experimental results [74]. As experiments have a limited domain of measurement, we have truncated our results to better provide a comparison. Each of the displayed curves are normalized such that the integral over the applicable domain is one.

Even with the truncation of the results, we can get a sense of what the increase in critical cluster radius does to the emitted size distribution. A local minimum in the size distribution is found at approximately the value of the critical radius itself. This was observed in most of the results above as well, where the critical radius was fixed at 0.6 nm. A larger critical radius allows for more depletion to the fraction of smaller clusters and we see that expressed in the minimum of the size distribution. Because of the depletion of smaller cluster coupled with the limitation on growth due to the chamber length, we also see that the dominant peak of the size distribution narrows

and becomes more pronounced.

The results for the variation in critical radius provide a good opportunity to make a favorable comparison to experiment as well. At the beginning of this chapter we identified our parameters and set them according to either experimentally known values or our best theoretical understanding. Throughout the results presented above, we were able to show how variations to these parameters would affect the size distribution. However, our best fit of parameters to the experiments (notably $r_c = 0.6$ nm using the melting point depression analysis of Sec. 5.4.4) would have only provided for a loose qualitative comparison to experimental results. But with a variation to the critical radius, we can find a good quantitative comparison. For a critical radius of 2 nm, we can see that the simulated size distribution is in good agreement with the experiment. The simulation still produces more smaller clusters than that which is observed in experiment. This result indicates that the cluster coagulation process is not limited to liquid clusters, and that it may be necessary to have a more thorough look at mechanisms for partial coalescence and the sticking efficiency of clusters.

6.4 Removal of Selected Processes

In the previous sections we showed the effects that several parameters had on the resulting cluster size distributions. Here we want to highlight the effect of some of the processes themselves on the cluster sizes. We consider the three crucial processes of atom attachment, cluster coagulation, and diffusion to the chamber walls. The results presented here can serve to support statements made above about the interaction between the various processes.

Figure 6.10 shows the effects of removing selected processes from the simulations. In the "full" distribution, we allow all processes to occur. In the other distributions, we remove one of the selected processes from the simulation to see how its absence affects the results. When we remove the cluster coagulation process (blue), we see that there is no local peak. Instead, the distribution is dominated by small clusters with a monotonically decaying long tail into the large cluster domain. With the removal of the atom attachment process (green), we only observe a small peak around clusters with a radius of 1 nm, but still observe a strong contribution from very small clusters. The removal of the wall diffusion process (orange) allows for a strong peak in the same domain as the full simulation.

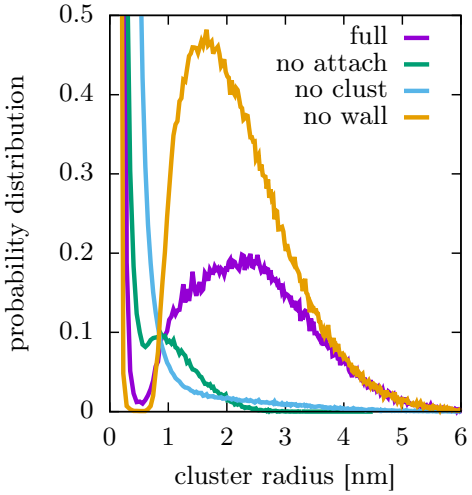

Figure 6.10: The effect of removing processes from the simulation. The full simulation (purple) includes the atom attachment, cluster coagulation, and wall diffusion processes. In the other curves, we remove one process to see how its absence affects the distribution. The absence of atom attachment (green) only produces small clusters, because coagulation is limited by the critical cluster radius. The absence of cluster coagulation (blue) does not produce a prominent peak because moderately-sized clusters are not generated fast enough. The absence of wall diffusion allows for a higher cluster density and a better probability that cluster collisions occur to deplete the smaller cluster, giving rise to a prominent peak.

This helps us build the picture of how the growth process works. The cluster coagulation process is essential to generate an initial peak within the cluster size distribution. The atom attachment process can broaden the size distribution, creating a larger tail. When the two processes are present together, the coagulation process creates an initial peak of small clusters by quickly acting on the smallest clusters available in the system. The atom attachment process can then act more effectively on the cluster sizes contained within the peak. These clusters grow more rapidly as the atom attachment process broadens the distribution. What results is a size distribution with a prominent peak. The wall diffusion process serves to limit the available clusters and has its most notable impact on the removal of mid-sized clusters.

6.5 Summary

The above results demonstrate a functional, self-consistent simulation that includes the most important and relevant process pertaining to the growth of nanoparticles in a magnetron cluster source. The processes themselves were developed and tested extensively in Ch. 4 and Ch. 5 and their implementation is found to be applicable to realistic magnetron plasmas. The model holds predictive capability as illustrated above with numerous variations in parameters.

We were also able to gain insight into the dynamics of cluster growth. In particular in the cooperation of the atom attachment and cluster coagulation processes to develop a pronounced peak in the cluster size distribution. The cluster coagulation process is needed to establish moderately-sized particles near the target. Because of its limitations, the coagulation process cannot significantly develop clusters much further than the size of the critical cluster radius. The atom attachment process can continue to work throughout the length of the chamber, further developing the products of the coagulation process to establish a dominating peak in the cluster size distribution. Without the coagulation process though, the atom attachment process alone would only provide for a monotonically decreasing size distribution.

There are some limitations, however, both to our knowledge and the model, that can limit the suitability of the present model. At the end of Sec. 4.6 we commented on the radial averaging of the free atom density. It is only appropriate to apply this average if $\mathrm{Pe}_{\mathrm{rad}}$ is sufficiently small and radial diffusion dominates over axial drift. If $\mathrm{Pe}_{\mathrm{rad}}$ is large, then we expect to have a tight beam of free metal atoms along the center of the chamber and the radial average applied to free atom density is not suitable. Properly addressing a concentration of free metal atoms along the chamber's axis has not been presented here and would likely demand some reconsiderations to the derived processes, particularly wall diffusion and cluster coagulation.

If there is something very slightly wrong in our definition of the theories, then the full mathematical rigor may convert these errors into ridiculous conclusions.

Richard Feynman

CHAPTER 7

Conclusions

This thesis dealt with the analysis of cluster formation in magnetron cluster sources. We have developed a self-consistent kinetic Monte Carlo model that can accurately account for the nucleation and growth of these clusters. The basic physical input parameters (buffer gas composition, pressure, flow rate, temperature, chamber length, target composition) are translated into analytic solutions for key model parameters (buffer gas drift velocity, buffer gas number density, free metal atom density, and metal atom density profile). These model parameters are shown to have a strong influence on the resulting cluster size distributions.

In formulating the model, we found it necessary to develop a hybrid KMC algorithm. We used a standard First Reaction algorithm as a skeletal structure for nucleating and moving clusters through the system, but also incorporated the Threshold KMC algorithm as a means of determining the performance of other events given changing parameters of the process rates. This presents an expansion to the possibilities and applicabilities of KMC simulations in general.

We analyzed cluster transport processes. We found a basic method of determining sputtered atom thermalization via the simple collision model. This model included explicit interactions between the atoms of the buffer gas and an embedded diffusing particle. In order to reduce the number of interactions we moved particle motion into a continuum regime that allowed us to analyze cluster transport in the context of diffusive motion governed in general by the Smoluchowski equation. By applying appropri-

ate boundary conditions to the Smoluchowski equation, we were led to models for the free atom density profile [61], 2D radial diffusion problem, and 1D axial motion [42].

The cluster growth mechanisms were analyzed with respect to the fundamental processes [7] of nucleation, atom attachment, and cluster coagulation. In order to deal with the growth of large clusters efficiently, we introduced a cluster size index scheme and found a statistically accurate means of compressing many single atom attachment events into growth by these indices.

All of these implementations were carried out so that we could simulate a measurement for cluster size distributions emitted from the magnetron source. The KMC method allowed us to look at some processes in isolation and how the physical parameters affected the resulting distribution. This allowed us to build of picture of cluster growth that is dominated by and indeed dependent upon the cluster coagulation processes in the early stages of development. Thereafter, the atom attachment process can work quickly to establish larger clusters.

It is important to make a note of the accuracy of the model and simulations. Systematic errors arise due to the limited dimensionality of the model. This was alluded to at the end of Sec. 4.6 and again in Sec. 4.7.1 in the discussion of the initial cluster density. Within the model, we average densities over a radial cross section. This is surely an approximation that may not stray significantly from experimental conditions given low Péclet numbers for the free metal atom drift. However, depending upon the experimental set-up, metal atom motion may be characterized by larger Péclet numbers. In this case, averaging the free metal atom density over a radial cross section will introduce an error as we would expect a much higher concentration of atoms along the axis of the chamber.

We also made note in Sec. 5.4 of the choice of the collision kernel. We gave an argument for utilizing the diffusive kernel based on estimations of the ratio of the mean free path between clusters and gas atoms (ℓ_g) and the typical inter-cluster distance (ℓ_c). It may be the case, however, that under the appropriate experimental conditions that the coagulation rate is better described by a kinetic kernel. As the ratio, ℓ_g/ℓ_c, is dependent on the cluster size, an optimal solution to the choice of the coagulation kernel would be some linear combination of the two kernels with coefficients that allow for the appropriate kernel to dominate under the right conditions.

In Chap. 6 we saw how several parameters coud independently affect the cluster size distribution. We found that among the input parameters that most strongly influence the resulting size distribution are the buffer gas drift velocity (via gas pressure

and flow rate), temperature, the free atom density (via ion current density), the cluster chamber length, and the critical radius of cluster coagulation. The nucleation constant has a rather minimal effect on the primary peak of the size distribution. Instead, larger nucleation constants allow for more clusters to enter into the systems and this aids in a more efficient depletion of smaller clusters. Additionally, we may add that an error in the diffusion coefficient itself would most directly impact cluster transport properties (diffusion to the chamber wall and axial motion). A larger diffusion coefficient makes for greater cluster mobility so clusters may move quicker radially to the chamber walls and axially out of the system.

Several ideas can be implemented for future development of the model. First, as pointed out above, it may prove useful to expand the dimensionality of the model space. In the presented model, we essentially reduced the full system to a 1D model with background conditions that were set by radially averaging the quantities (free atom density, buffer gas density, drift velocity). We can envision a 2D or even 3D model that could better resolve the background densities, in particular the free metal atom density. This would necessitate a re-examination of the wall diffusion process which could perhaps be resolved through Lattice Monte Carlo methods [42] similar to those utilized in the implemented axial transport scheme.

The second major development to implement would be the inclusion of particle species from the plasma environment, such as buffer gas ions and electrons, especially near the target. Such a consideration begs for the inclusion of several additional processes as well. Cluster collisions with ions and electrons can result in a net charge being transferred to the clusters [7, 80]. The consideration of charged clusters would entail a re-examination of collision cross sections as the Coulomb force between charged clusters should be considered. Another process that could be included in conjunction with more particle species is cluster heating [81].

In treating the cluster growth process, we could find an implementation that allows for the evaporation or dissociation of clusters [82, 83]. This may be especially important for the representation of small clusters as viable nuclei could be larger than the dimers utilized in the current model [26]. An evaporation or dissociation process may result in a reduction of the observed prominence of small clusters in the presented size distributions. Another idea for the treatment of cluster growth is an implementation of a fractal dimension for clusters [61, 84, 85] which has the capacity to treat more cluster morphologies than the perfect spheres of the liquid drop model. The inclusion of a fractal dimension would imply coagulation events that result in partial coalescence, oblate

clusters, or clusters that are otherwise poorly suited to the liquid drop approximation, such as the cauliflower morphologies sometimes observed in experiment [86, 87].

The cluster velocity distribution is known to vary with size [19] and can have a large influence on the deposition process [88]. Therefore, if we want this model to useful beyond predictions of size distributions, we should better incorporate cluster velocities, especially in the vicinity of the chamber's orifice. We can start with an analysis of the dynamics of gas flows through an orifice [89, 90] and apply the principles developed in the simple collision model to clusters near the orifice to achieve variations in cluster velocities.

A final thought for a direction of development, one that would contribute to many of the aforementioned extensions, is to include a gradient of gas temperatures. The gas temperature is known to be higher near the target [91]. Including a temperature variation would influence all processes that are currently implemented in the model and would additionally effect cluster heating, evaporation and dissociation, and cluster velocities.

Bibliography

[1] T. Montmerle, J.-C. Augereau, M. Chaussidon, M. Gounelle, B. Marty, and A. Morbidelli. "*3. Solar System Formation and Early Evolution: the First 100 Million Years*". Earth, Moon, and Planets, **98**, 39–95 (2006); (p. 1).

[2] H. W. Yorke and P. Bodenheimer. "*The Formation of Protostellar Disks. III. The Influence of Gravitationally Induced Angular Momentum Transport on Disk Structure and Appearance*". The Astrophysical Journal, **525**, 330 (1999); (p. 1).

[3] D. Ward-Thompson. "*Isolated Star Formation: From Cloud Formation to Core Collapse*". Science, **295**, 76–81 (2002); (p. 1).

[4] M. Kulmala, H. Vehkamäki, T. Petäjä, M. Dal Maso, A. Lauri, V. M. Kerminen, W. Birmili, and P. H. McMurry. "*Formation and growth rates of ultrafine atmospheric particles: a review of observations*". Journal of Aerosol Science, **35**, 143–176 (2004); (p. 1).

[5] V. I. Khvorostyanov. "*Mesoscale processes of cloud formation, cloud-radiation interaction, and their modelling with explicit cloud microphysics*". Atmospheric Research, **39**, 1–67 (1995); (p. 1).

[6] M. Ganeva. "*Formation of metal nano-size clusters with a DC magnetron-based gas aggregation source*". PhD thesis, Ernst-Moritz-Arndt-Universität Greifswald, 2013; (pp. 1, 93).

[7] B. M. Smirnov. "*Processes involving clusters and small particles in a buffer gas*". Physics-Uspekhi, **54**, 691–721 (2011); (pp. 1, 9, 11, 13, 67–68, 71, 73, 80, 108–109).

[8] W. A. de Heer. "*The physics of simple metal clusters: experimental aspects and simple models*". Reviews of Modern Physics, **65**, 611–676 (1993); (pp. 1, 67).

[9] I. CODIŢĂ, D. M. CAPLAN, E.-C. DRĂGULESCU, B.-E. LIXANDRU, I. L. COLDEA, C. C. DRAGOMIRESCU, C. SURDU-BOB, and M. BĂDULESCU. "*Antimicrobial activity of copper and silver nanofilms on nosocomial bacterial species*". Roumanian Archives of Microbiology and Immunology, **69**, 204–212 (2010); (p. 2).

[10] E. C. DREADEN, L. A. AUSTIN, M. A. MACKEY, and M. A. EL-SAYED. "*Size matters: gold nanoparticles in targeted cancer drug delivery*". Therapeutic delivery, **3**, 457–478 (2012); (p. 2).

[11] S. SINGAMANENI, V. N. BLIZNYUK, C. BINEK, and E. Y. TSYMBAL. "*Magnetic nanoparticles: recent advances in synthesis, self-assembly and applications*". Journal of Materials Chemistry, **21**, 16819–16845 (2011); (p. 2).

[12] O. N. GADOMSKII and Y. Y. KHARITONOV. "*Quantum computer based on activated dielectric nanoparticles selectively interacting with short optical pulses*". Quantum Electronics, **34**, 249 (2004); (p. 2).

[13] X. QU, P. J. J. ALVAREZ, and Q. LI. "*Applications of nanotechnology in water and wastewater treatment*". Water Research, **47**, 3931–3946 (2013); (p. 2).

[14] Q. ZHIQIANG, K. SIEGMANN, A. KELLER, U. MATTER, L. SCHERRER, and H. C. SIEGMANN. "*Nanoparticle air pollution in major cities and its origin*". Atmospheric Environment, **34**, 443–451 (2000); (p. 2).

[15] P. V. KASHTANOV, B. M. SMIRNOV, and R. HIPPLER. "*Magnetron plasma and nanotechnology*". Physics-Uspekhi, **50**, 455 (2007); (pp. 5–6, 9, 11, 48, 71, 73, 91).

[16] P. A. REDHEAD. "*The Invention of the Cavity Magnetron and Its Introduction into Canada and the U.S.A.*" Physics in Canada, **57**, 321–328 (2001); (p. 5).

[17] H. OECHSNER. "*Sputtering—a review of some recent experimental and theoretical aspects*". Applied physics, **8**, 185–198 (1975); (p. 5).

[18] P. J. KELLY and R. D. ARNELL. "*Magnetron sputtering: a review of recent developments and applications*". Vacuum, **56**, 159–172 (2000); (pp. 5, 91).

[19] M. GANEVA, A. V. PIPA, B. M. SMIRNOV, P. V. KASHTANOV, and R. HIPPLER. "*Velocity distribution of mass-selected nano-size cluster ions*". Plasma Sources Science and Technology, **22**, 045011 (2013); (pp. 6, 32, 38, 72, 91, 110).

[20] A. N. BANERJEE, R. KRISHNA, and B. DAS. "*Size controlled deposition of Cu and Si nano-clusters by an ultra-high vacuum sputtering gas aggregation technique*". Applied Physics A, **90**, 299–303 (2008); (p. 6).

[21] P. Asanithi, S. Chaiyakun, and P. Limsuwan. "*Growth of Silver Nanoparticles by DC Magnetron Sputtering*". Journal of Nanomaterials, **2012**, (2012); (p. 6).

[22] A. I. Ayesh, N. Qamhieh, H. Ghamlouche, S. Thaker, and M. El-Shaer. "*Fabrication of size-selected Pd nanoclusters using a magnetron plasma sputtering source*". Journal of Applied Physics, **107**, 034317 (2010); (p. 6).

[23] C. Xirouchaki and R. E. Palmer. "*Deposition of size-selected metal clusters generated by magnetron sputtering and gas condensation: a progress review*". Philosophical Transactions of the Royal Society A: Mathematical, Physical and Engineering Sciences, **362**, 117–124 (2004); (pp. 6, 93).

[24] H. Hartmann, V. N. Popok, I. Barke, V. von Oeynhausen, and K.-H. Meiwes-Broer. "*Design and capabilities of an experimental setup based on magnetron sputtering for formation and deposition of size-selected metal clusters on ultra-clean surfaces*". Review of Scientific Instruments, **83**, 073304 (2012); (p. 6).

[25] A. Majumdar, D. Köpp, M. Ganeva, D. Datta, S. Bhattacharyya, and R. Hippler. "*Development of metal nanocluster ion source based on dc magnetron plasma sputtering at room temperature*". Review of Scientific Instruments, **80**, 095103 (2009); (pp. 6, 72).

[26] T. Hihara and K. Sumiyama. "*Formation and size control of a Ni cluster by plasma gas condensation*". Journal of Applied Physics, **84**, 5270–5276 (1998); (pp. 7, 32, 109).

[27] B. M. Smirnov, I. Shyjumon, and R. Hippler. "*Formation of clusters through generation of free atoms*". Physica Scripta, **73**, 288–295 (2006); (pp. 9, 11, 67, 71, 73).

[28] P. V. Kashtanov, B. M. Smirnov, and R. Hippler. "*Efficiency of cluster generation in a magnetron discharge*". EPL (Europhysics Letters), **91**, 63001 (2010); (pp. 9, 73).

[29] P. V. Kashtanov and B. M. Smirnov. "*Nanoclusters: Properties and processes*". High Temperature, **48**, 846–859 (2010); (pp. 9, 68).

[30] B. Briehl and H. M. Urbassek. "*Monte Carlo simulation of growth and decay processes in a cluster aggregation source*". Journal of Vacuum Science & Technology A, **17**, 256–265 (1999); (pp. 10–11, 70).

[31] K. De Bleecker, A. Bogaerts, R. Gijbels, and W. Goedheer. "*Numerical investigation of particle formation mechanisms in silane discharges*". Physical Review E, **69**, (2004); (p. 11).

[32] K. De Bleeker. "*Modeling of the formation and behavior of nanoparticles in dusty plasmas*". PhD thesis, Universiteit Antwerpen, 2006; (p. 11).

[33] O. Fischer, T. Henning, and H. W. Yorke. "*Simulation of polarization maps. 1: Protostellar envelopes*". Astronomy and Astrophysics, **284**, 187–209 (1994); (pp. 13, 17).

[34] A. F. Voter, F. Montalenti, and T. C. Germann. "*Extending the Time Scale in Atomistic Simulation of Materials*". Annual Review of Materials Research, **32**, 321–346 (2002); (p. 13).

[35] A. F. Voter. "Introduction to the Kinetic Monte Carlo Method". In: *Radiation Effects in Solids*. K. E. Sickafus, E. A. Kotomin, and B. P. Uberuaga (eds.). NATO Science Series 235. Springer Netherlands, 2007, pp. 1–23 (p. 13).

[36] J. G. Amar. "*The Monte Carlo method in science and engineering*". Computing in science & engineering, **8**, 9–19 (2006); (p. 13).

[37] P. Kratzer. "*Monte Carlo and kinetic Monte Carlo methods*". arXiv preprint arXiv:0904.2556, (2009); (p. 13).

[38] A. Bortz, M. Kalos, and J. Lebowitz. "*A new algorithm for Monte Carlo simulation of Ising spin systems*". Journal of Computational Physics, **17**, 10–18 (1975); (pp. 14, 34).

[39] D. T. Gillespie. "*A general method for numerically simulating the stochastic time evolution of coupled chemical reactions*". Journal of Computational Physics, **22**, 403–434 (1976); (p. 14).

[40] D. T. Gillespie. "*Exact stochastic simulation of coupled chemical reactions*". The Journal of Physical Chemistry, **81**, 2340–2361 (1977); (p. 14).

[41] L. Rosenthal. "*Kinetic Monte Carlo Simulations of Metal-Polymer Nanocomposite Formation*". PhD thesis, Christian-Albrechts-Universität zu Kiel, 2013; (pp. 14, 84).

[42] M. G. Gauthier and G. W. Slater. "*Building reliable lattice Monte Carlo models for real drift and diffusion problems*". Physical Review E, **70**, 015103 (2004); (pp. 21, 58, 108–109).

[43] M. Kendall and A. Stuart. The Advanced Theory of Statistics v. 1. Griffin, 1967; (p. 25).

[44] R. A. Fisher. "*Moments and Product Moments of Sampling Distributions.*" Proc. Lond. Math. Soc. **30**, (1929); (p. 25).

[45] R. Serway and J. J. Jr. 9th ed. Physics for Scientists & Engineers. Books/Cole Publishing, 2014; (p. 32).

[46] L. Hinkle. "Chapter 3.4 - Mass Flow Measurement and Control". In: *Handbook of Vacuum Science and Technology*. D. M. Hoffman and B. S. H. T. H. Thomas (eds.). Academic Press, San Diego, 1998, pp. 376–388 (p. 32).

[47] D. Lemons and P. Langevin. Johns Hopkins Paperback. Johns Hopkins University Press, 2002; (p. 34).

[48] R. W. Wolff. "*Poisson Arrivals See Time Averages*". Operations Research, **30**, 223–231 (1982); (p. 34).

[49] R. E. Somekh. "*The thermalization of energetic atoms during the sputtering process*". Journal of Vacuum Science & Technology A, **2**, 1285–1291 (1984); (p. 34).

[50] S. Chapman and T. Cowling. *The Mathematical Theory of Non-uniform Gases: An Account of the Kinetic Theory of Viscosity, Thermal Conduction and Diffusion in Gases*. Cambridge Mathematical Library. Cambridge University Press, 1970; (pp. 40, 42).

[51] T. R. Marrero and E. A. Mason. "*Correlation and prediction of gaseous diffusion coefficients*". AIChE Journal, **19**, 498–503 (1973); (pp. 40, 42).

[52] T. Ott, P. Ludwig, H. Kählert, and M. Bonitz. In: M. Bonitz, N. Horing, and P. Ludwig, *Introduction to Complex Plasmas*. Chap. Molecular Dynamics Simulation of Strongly Correlated Dusty Plasmas. Springer Series on Atomic, Optical, and Plasma Physics. Springer Berlin Heidelberg, 2010; (pp. 40–41).

[53] S. Redner. A Guide to First-passage Processes. Cambridge University Press, 2001; (pp. 41, 65).

[54] A. Nagar and P. Pradhan. "*First passage time distribution in random walks with absorbing boundaries*". Physica A: Statistical Mechanics and its Applications, **320**, 141–148 (2003); (pp. 41, 53).

[55] C. R. Wilke. "*A Viscosity Equation for Gas Mixtures*". The Journal of Chemical Physics, **18**, 517–519 (1950); (p. 42).

[56] D. F. Fairbanks and C. R. Wilke. "*Diffusion Coefficients in Multicomponent Gas Mixtures*". Industrial & Engineering Chemistry, **42**, 471–475 (1950); (p. 43).

[57] J. D. Ramshaw. "*Self-Consistent Effective Binary Diffusion in Multicomponent Gas Mixtures*". Journal of Non Equilibrium Thermodynamics, **15**, 295–300 (1990); (p. 43).

[58] G. WILEMSKI. "*On the derivation of Smoluchowski equations with corrections in the classical theory of Brownian motion*". Journal of Statistical Physics, **14**, 153–169 (1976); (p. 45).

[59] A. SZABO, K. SCHULTEN, and Z. SCHULTEN. "*First passage time approach to diffusion controlled reactions*". The Journal of Chemical Physics, **72**, 4350–4357 (1980); (p. 45).

[60] G. B. ARFKEN, H. J. WEBER, and F. E. HARRIS. 6th ed. Academic Press, July 5, 2005; (p. 47).

[61] A. A. TURKIN, M. V. DUTKA, Y. T. PEI, D. I. VAINSHTEIN, and J. T. M. DE HOSSON. "*On the evolution of nanocluster size distribution in a nanocluster aggregation source*". Journal of Applied Physics, **111**, 124326 (2012); (pp. 47, 108–109).

[62] P. W. J. M. BOUMANS. "*Sputtering in a glow discharge for spectrochemical analysis*". Analytical Chemistry, **44**, 1219–1228 (1972); (p. 49).

[63] A. MARSHALL and I. OLKIN. "The Inverse Gaussian Distribution". English. In: *Life Distributions*. Springer Series in Statistics. Springer New York, 2007, pp. 451–471 (p. 57).

[64] G. GUO and X. QIU. "*First passage time distributions of anomalous biased diffusion with double absorbing barriers*". Physica A: Statistical Mechanics and its Applications, **411**, 80–86 (2014); (pp. 62–63).

[65] M. P. MOODY and P. ATTARD. "*Homogeneous nucleation of droplets from a supersaturated vapor phase*". The Journal of Chemical Physics, **117**, 6705 (2002); (p. 67).

[66] E. KOVACEVIC. "*Plasma polymerized carbonaceous nanoparticles: application as astroanalog*". PhD thesis, Ruhr-Universität Bochum, 2006; (p. 74).

[67] J. SPIEß. "*Some Identities Involving Harmonic Numbers*". Mathematics of Computation, **55**, (1990); (p. 75).

[68] M. AKKOUCHI. "*On the Convolution of Exponential Distributions*". Journal of the Chungcheong Mathematical Society, **21**, (2008); (p. 76).

[69] M. V. SMOLUCHOWSKI. "*Drei Vorträge über Diffusion, Brownsche Bewegung und Koagulation von Kolloidteilchen*". Zeitschrift fur Physik, **17**, 557–585 (1916); (p. 80).

[70] K. K. NANDA. "*Size-dependent melting of nanoparticles: Hundred years of thermodynamic model*". Pramana, **72**, 617–628 (2009); (pp. 84, 102).

[71] K. Nanda, S. Sahu, and S. Behera. "*Liquid-drop model for the size-dependent melting of low-dimensional systems*". Physical Review A, **66**, (2002); (pp. 84–85).

[72] J. Ross and R. P. Andres. "*Melting temperature of small clusters*". Surface Science, **106**, 11–17 (1981); (p. 84).

[73] J. P. Borel. "*Thermodynamical size effect and the structure of metallic clusters*". Surface Science, **106**, 1–9 (1981); (p. 84).

[74] M. Ganeva. "*Report on measurement and evaluation of Cu cluster size distributions*". unpublished, private communication, 2013 (pp. 91, 103).

[75] W. Eckstein. *Calculated sputtering, reflection and range values*. Max-Planck-Institut für Plasmaphysik, Garching (Germany), 2002 (p. 91).

[76] C. H. Shon and J. K. Lee. "*Modeling of magnetron sputtering plasmas*". Applied Surface Science, **192**, 258–269 (2002); (p. 91).

[77] L. S. Wang, R. T. Wen, Y. Chen, G. H. Yue, D. L. Peng, and T. Hihara. "*Gas-phase preparation and size control of Fe nanoparticles*". Applied Physics A, **103**, 1015–1020 (2011); (p. 94).

[78] M. R. Zachariah and M. J. Carrier. "*Molecular dynamics computation of gas-phase nanoparticle sintering: a comparison with phenomenological models*". Journal of Aerosol Science, **30**, 1139–1151 (1999); (p. 102).

[79] J. S. Raut, R. B. Bhagat, and K. A. Fichthorn. "*Sintering of aluminum nanoparticles: A molecular dynamics study*". Nanostructured Materials, **10**, 837–851 (1998); (p. 102).

[80] J. Blažek, P. Bartoš, R. Basner, and H. Kersten. "*Distribution of charge on clusters in a magnetron discharge*". Proceedings 30th ICPIG, Belfast, Northern Ireland, UK, (2011); (p. 109).

[81] H. R. Maurer and H. Kersten. "*On the heating of nano- and microparticles in process plasmas*". Journal of Physics D: Applied Physics, **44**, 174029 (2011); (p. 109).

[82] F. Calvo and P. Parneix. "*Accurate modeling of sequential decay in clusters over long time scales: Insights from phase space theory*". The Journal of Chemical Physics, **126**, (2007); (p. 109).

[83] U. L. Yannouleas C. and R. Barnett. "Dissociation, Fragmentation, and Fission of Simple Metal Clusters". In: *Metal Clusters*. W. Ekardt (ed.). Wiley Press, New York, 1999, pp. 145–180 (p. 109).

[84] M. KOSTOGLOU and A. G. KONSTANDOPOULOS. "*Evolution of aggregate size and fractal dimension during Brownian coagulation*". Journal of Aerosol Science, **32**, 1399–1420 (2001); (p. 109).

[85] M. K. WU and S. K. FRIEDLANDER. "*Enhanced power law agglomerate growth in the free molecule regime*". Journal of Aerosol Science, **24**, 273–282 (1993); (p. 109).

[86] L. P. EN-KYUL YU and S.-H. KIM. "*Sintering Behavior of Copper Nanoparticles*". Bulletin of the Korean Chemical Society, **32**, 4099–4102 (2011); (p. 110).

[87] T. ACSENTE, R. NEGREA, L. NISTOR, C. LOGOFATU, E. MATEI, R. BIRJEGA, C. GRISOLIA, and G. DINESCU. "*Synthesis of flower-like tungsten nanoparticles by magnetron sputtering combined with gas aggregation*". The European Physical Journal D, **69**, (2015); (p. 110).

[88] A. IPATOV, P.-G. REINHARD, and E. SURAUD. "*Velocity dependence of metal cluster deposition on an insulating surface*". The European Physical Journal D, **30**, 65–70 (2004); (p. 110).

[89] F. SHARIPOV. "Rarefied Gas Flow Through an Orifice at Finite Pressure Ratio". In: *AIP Conference Proceedings*. Rarefied Gas Dynamics: 23rd International Symposium. Vol. 663. AIP Publishing, May 5, 2003, pp. 1049–1056 (p. 110).

[90] S. EIAMSA-ARD. "*Numerical Investigation of Turbulent Flow Through a Circular Orifice*". KMITL Sci. J. **8**, (2008); (p. 110).

[91] A. BOGAERTS, R. GIJBELS, and V. V. SERIKOV. "*Calculation of gas heating in direct current argon glow discharges*". Journal of Applied Physics, **87**, 8334–8344 (2000); (p. 110).

Publications in Peer Reviewed Journals

1. M. Bonitz, L. Rosenthal, K. Fujioka, V. Zaporojtchenko, F. Faupel, and H. Kersten. *"Towards a Particle Based Simulation of Complex Plasma Driven Nanocomposite Formation"*. Contrib. Plasma Phys. **52**, 890–898 (2012).

Acknowledgements

It is impossible for me to consider that this work is solely my own. It is true that I have labored alone over the research and writing, but without the amazing support of a network of friends and family, crossing continents and time-zones, this would not have been possible to complete. As such, this is an accomplishment for all of us.

First and foremost I would like to thank Prof. Dr. Michael Bonitz for allowing me the opportunity to work towards a doctorate under your supervision. Your patience knows no bounds. Your advice and suggestions were always constructive and pushed my comprehension and understanding.

Thank you to Prof. Dr. Sebastian Wolf for many engaging discussions. Your encouragement always left a smile on my face as I left your office.

A special thank you to Christian Henning. You are the reason I first came to Germany, and our continued friendship means so much to me.

To my friends and fellow group members, thank you all for making me feel welcome. Our light-hearted conversations over coffee (or beer) will always be cherished. In particular I'd like to thank Jan Willem Abraham, Sebastian Bauch, Annika Drews, Fanny Geisler, David Hochstuhl, Hanno Kählert, Patrick Ludwig, Torben Ott, Lasse Rosenthal, Hauke Thomsen, and Tim Schoof for helping me integrate into life here in Germany and answering all the questions that I had over the years.

Thank you to Amir Mohammad Ahadi and Marina Ganeva for your discussions and feedback from an experimentalist's perspective. My work could not have taken root without your input.

Finally I would like to thank my family for their unconditional love and support. Mom and Dad, you have always believed in me and I truly would not be here if it weren't for you. Emily, no words can do justice to how much you've helped me. Tai and Mei, you are the biggest inspiration to my life. I love you all.

Selbständigkeitserklärung

Hiermit versichere ich, dass die vorliegende Abhandlung – abgesehen von der Beratung durch den Betreuer – nach Inhalt und Form die eigene Arbeit ist.

Des Weiteren versichere ich, dass die Arbeit unter Einhaltung der Regeln guter wissenschaftlicher Praxis[1] der Deutschen Forschungsgemeinschaft entstanden ist.

Ich versichere, dass die vorliegende Arbeit weder ganz noch zum Teil schon einer anderen Stelle im Rahmen eines Prüfungsverfahrens vorgelegen hat, sowie in dieser Form weder veröffentlicht worden ist noch zur Veröffentlichung eingereicht wurde. Die im Rahmen der Arbeit entstandenen Publikationen in wissenschaftlichen Fachzeitschriften sind auf Seite 119 vermerkt.

Kiel,

[1] Deutsche Forschungsgemeinschaft. *Vorschläge zur Sicherung guter wissenschaftlicher Praxis. „Empfehlungen der Kommission Selbstkontrolle in der Wissenschaft“*, Wiley-VCH, Weinheim (1998).